

# ELECTRONIC STRUCTURE STUDIES OF GRAPHITE SYSTEMS AND SOME TRANSITION METAL OXIDES

By

**Rupali Kundu**

**INSTITUTE OF PHYSICS, BHUBANESWAR.**

A thesis submitted to the  
Board of Studies in Physical Sciences

In partial fulfillment of the requirements

For the Degree of

**DOCTOR OF PHILOSOPHY**

*of*

**HOMI BHABHA NATIONAL INSTITUTE**



March 4, 2013

# Homi Bhabha National Institute

## Recommendations of the Viva Voce Board

As members of the Viva Voce Board, we recommend that the dissertation prepared by **Rupali Kundu** entitled “ ELECTRONIC STRUCTURE STUDIES OF GRAPHITE SYSTEMS AND SOME TRANSITION METAL OXIDES” may be accepted as fulfilling the dissertation requirement for the Degree of Doctor of Philosophy.

----- **Date :**  
Chairman :

----- **Date :**  
Convener :

----- **Date :**  
Member :

----- **Date :**  
Member :

----- **Date :**  
Member :

Final approval and acceptance of this dissertation is contingent upon the candidate's submission of the final copies of the dissertation to HBNI.

I hereby certify that I have read this dissertation prepared under my direction and recommend that it may be accepted as fulfilling the dissertation requirement.

----- **Date :**  
Guide : Prof. Biju Raja Sekhar

## **STATEMENT BY AUTHOR**

This dissertation has been submitted in partial fulfillment of requirements for an advanced degree at Homi Bhabha Institute (HBNI) and is deposited in the Library to be made available to borrowers under rules of the HBNI.

Brief quotations from this dissertation are allowable without special permission, provided that accurate acknowledgement of source is made. Requests for permission for extended quotation from or reproduction of this manuscript in whole or in part may be granted by the Competent Authority of HBNI when in his or her judgment the proposed use of the material is in the interests of scholarship. In all other instances, however, permission must be obtained from the author.

Rupali Kundu

## **DECLARATION**

I, hereby declare that the investigation presented in the thesis has been carried out by me. The work is original and the work has not been submitted earlier as a whole or in part for a degree/diploma at this or any other Institution or University.

Rupali Kundu

*To my parents*

---

## ACKNOWLEDGEMENTS

I would like to take this opportunity to thank all the people who have inspired and helped me during my doctoral study and stay here. Foremost, I wish to express my deep and sincere gratitude to my thesis supervisor Prof. Biju Raja Sekhar for his valuable guidance and encouragement throughout this work. He also provided me enough freedom to work in my own way. It is my pleasure to thank Prof. S. G. Mishra for tolerating all the disturbances and nuisance I had created for him and for teaching me to think in a systematic manner. His suggestions and support have helped me to construct a significant part of my thesis. I feel very happy to acknowledge the moral support, timely advice and encouragements from Prof. S. M. Bhattacharjee and Prof. Sudipta Mukherji. I have always enjoyed their company and learned many things related to academics as well as non-academics.

I am thankful to my collaborators Dr. Prabir Pal and Dr. Manas Kumar Dalai for making me familiar with the instruments and for various discussions. I am also thankful to Pramita and Himanshu for their company and support during many long duration experiments and discussions. I thank Dr. Monodeep Chakraborty for introducing me to the basics of some numerical codes. I acknowledge the help, suggestions and discussions from Prof. S. R. Barman and Mr. M. Maniraj during the inverse photoemission study of graphite at UGC-CSR, Indore. I also thank Prof. C. Martin for providing good quality manganite samples. My sincere thanks go to Prof. R. Suryanarayanan for providing multiferroic samples.

I wish to extend my hearty thanks to Saramadi, Ranjana, Smita madam, Archana and Prof. Alok Kumar for the warm hospitality they have provided me at many times and made my stay at IOP a pleasant and enjoyable one.

I wish to express my warm thanks to all my predoctoral batch mates and scholar friends for their help and good wishes. I have enjoyed many moments of useful and not so useful arguments with my friends Sankha, Jaya, Saumia, Binata, Kuntala, Pramita, Subhadeep, Sazim.

I am grateful to many of my school teachers without whose continuous support and encouragement I would not have reached here.

Finally my deepest gratitude goes to my family members: my parents, my brother and my grand mother for their love, affection, care and immense support throughout the entire period which have helped me to make this thesis possible.

<b>Synopsis</b>	<b>xi</b>
<b>1 Introduction</b>	<b>1</b>
1.1 <i>sp</i> <sup>2</sup> hybridized carbon materials . . . . .	1
1.1.1 Graphite . . . . .	1
1.1.2 Graphene . . . . .	3
1.1.3 Bilayer graphene . . . . .	3
1.2 <b>Transition metal oxides</b> . . . . .	4
1.2.1 Multiferroics . . . . .	4
1.2.2 Manganites . . . . .	5
1.3 <b>Structure of the thesis</b> . . . . .	6
<b>2 Experimental Techniques</b>	<b>10</b>
2.1 <b>Photoelectron Spectroscopy:</b> . . . . .	10
2.1.1 History of Photoelectron Spectroscopy: . . . . .	10
2.1.2 Principle of photoemission and some of its general aspects . . . . .	11
2.1.3 Theory of photoemission . . . . .	15
2.2 <b>Inverse Photoelectron Spectroscopy:</b> . . . . .	21
2.2.1 Basic principle . . . . .	21
2.2.2 Instrumentation . . . . .	23
2.3 <b>Resonance Photoemission Spectroscopy (ResPES)</b> . . . . .	24
2.3.1 X-ray Absorption Spectroscopy . . . . .	24
2.3.2 ResPES . . . . .	25
2.4 <b>Instrumentation</b> . . . . .	27
2.4.1 Gas Discharge Lamp . . . . .	27
2.4.2 X-ray source . . . . .	28
2.4.3 Synchrotron Radiation . . . . .	29
2.5 <b>Energy Analyser</b> . . . . .	30
2.5.1 Hemispherical Analyser . . . . .	30
2.5.2 Electron Lens System . . . . .	31
2.5.3 Single Channel Detector . . . . .	32
2.5.4 Pulse Counting Operation . . . . .	33

2.5.5	Channeltron Operating Plateau . . . . .	33
2.5.6	Low Energy Electron Diffraction (LEED) unit . . . . .	34
2.5.7	Sample Surface Preparation . . . . .	34
<b>3</b>	<b>Tight Binding Calculations of Graphene, Bilayer Graphene and Graphite</b>	<b>38</b>
3.1	<b>Introduction</b> . . . . .	38
3.2	<b>Geometrical structure</b> . . . . .	40
3.3	<b>Electronic structure of a hexagonal sheet of carbon atoms</b> . . . . .	42
3.3.1	Tight binding band of graphene . . . . .	43
3.3.2	Tight binding band of bilayer graphene . . . . .	48
3.3.2.1	Modifications in the bands due to the inclusion of overlap integrals ( $s_0, s'_1$ ) coming from in-plane and inter-plane nearest neighbours and due to breaking of sublattice symmetry . . . . .	50
3.3.2.2	Effect of in-plane second nearest neighbour hopping ( $\gamma_1$ ) and corresponding overlap integral ( $s_1$ ) on the spectra of bilayer graphene . . . . .	52
3.3.2.3	Modification due to the in-plane third nearest neighbour hopping energy ( $\gamma_2$ ) and the overlap integral ( $s_2$ ) on the bands of bilayer graphene . . . . .	53
3.3.3	Tight binding band of graphite . . . . .	55
3.4	<b>Density of states</b> . . . . .	59
3.5	<b>Summary and Conclusion</b> . . . . .	62
3.6	<b>Derivation of the electronic dispersions of graphene in presence of different neighbours</b> . . . . .	64
<b>4</b>	<b>Band Structure of single crystal graphite and HOPG from ARPES and KRIPES</b>	<b>69</b>
4.1	<b>Introduction</b> . . . . .	69
4.2	<b>Experimental</b> . . . . .	70
4.3	<b>Results and Discussions</b> . . . . .	71
4.4	<b>Summary and Conclusions</b> . . . . .	82
<b>5</b>	<b>Electronic structure of <math>\text{Bi}_{1-x}\text{Pb}_x\text{FeO}_3</math> from XPS and UPS</b>	<b>87</b>
5.1	<b>Introduction</b> . . . . .	87
5.2	<b>Experimental</b> . . . . .	89

5.3	<b>Results and Discussions</b> . . . . .	90
5.4	<b>Summary and Conclusions</b> . . . . .	94
<b>6</b>	<b>Electronic Structure of <math>\text{Sm}_{0.1}\text{Ca}_{0.9-x}\text{Sr}_x\text{MnO}_3</math> from UPS and ResPES Studies</b>	<b>96</b>
6.1	<b>Introduction</b> . . . . .	96
6.2	<b>Experimental</b> . . . . .	97
6.3	<b>Results and Discussion</b> . . . . .	98
6.4	<b>Conclusions</b> . . . . .	103
<b>7</b>	<b>Summary</b>	<b>106</b>

# List of Figures

2.1	The schematic of a photoemission experiment. The photoemitted electron is specified by its kinetic energy ( $E_{kin}$ ) and the emission angles $\theta$ and $\phi$ . The intensity of the outgoing electrons is measured by the analyzer as a function of ( $E_{kin}$ ). . . . .	12
2.2	The schematic energy level diagram of photoemission process. $E_F$ and $E_{vac}$ are the Fermi energy and the vacuum level of the system. The intensity of the outgoing electrons is measured as a function of kinetic energy ( $E_{kin}$ ). . .	13
2.3	The universal curve of the electron mean free path versus kinetic energy. . .	16
2.4	Illustration of the three-step model of photoemission. It consists of (1) the photoexcitation of an electron in the bulk, (2) its travel through the solid to the surface and (3) its transmission through the surface into the vacuum. . .	17
2.5	Illustration of inverse photoemission spectroscopy. The typical experimental arrangement (upper diagram). The energy level diagram of the process (lower diagram). If the measured photon energy is held constant and the incident electron beam energy is swept (isochromat mode), the intensity distribution of photon replicates the density of states of unoccupied electronic states. . . . .	22
2.6	A schematic diagram of the X-ray absorption process: an electron is excited from the core level (CL) to the unoccupied states in conduction bands (CB) by absorbing a photon with energy $h\nu$ , leaving a hole in the core level. Such an electron-hole pair may decay through either X-ray fluorescence or emission of Auger electrons. . . . .	25
2.7	A schematic diagram for a resonant photoemission process for $3d$ transition metal compounds. . . . .	26
2.8	Rotation planes of AR65 analyser. . . . .	30
2.9	A schematic diagram of hemispherical analyser. . . . .	31
2.10	A schematic diagram of electron amplification in a channeltron. . . . .	32
2.11	A plateau curve of a channeltron. . . . .	33
2.12	A typical set-up of LEED experimental. . . . .	35
3.1	Structure of graphene. The structure with black circles forms the A-sublattice and that with red circles gives B-sublattice. $\vec{a}_1$ and $\vec{a}_2$ are the unit vectors. . .	41

3.2	(a) Structure of bilayer graphene with unit vectors $\vec{a}_1, \vec{a}_2$ ; the intralayer nearest neighbour coupling energy ( $\gamma_0$ ), interlayer nearest neighbour coupling energy ( $\gamma'_1$ ), intralayer next nearest neighbour coupling energy ( $\gamma_1$ ) and next to next nearest neighbour coupling energy ( $\gamma_2$ ). (b) Brillouin zone of single layer and bilayer graphene with unit vectors $\vec{b}_1, \vec{b}_2$ and the high symmetry directions. . . . .	42
3.3	Electronic structure of graphene with first principle result (full curves), first nearest neighbour interactions (dashed-dotted curves), second nearest neighbour interactions (dotted curves) when first nearest neighbour parameters are fixed and third nearest neighbour interactions (dashed curves) when first and second nearest neighbour parameters are fixed. The parameters are listed in Table 3.1. . . . .	46
3.4	Electronic structure of graphene with first principle result (full curves), first nearest neighbour interactions (dashed-dotted curves), second nearest neighbour interactions (dotted curves) and third nearest neighbour interactions (dashed curves). The parameters are listed in Table 3.2. Here for each curve the parameters are chosen freely. . . . .	47
3.5	Electronic spectra of bilayer graphene. For all three cases, in the upper panel we have plotted the bands along all the high symmetry directions of the brillouin zone and the lower panels show zoomed versions of the corresponding upper panels near the $K$ point. In all the panels the full curves represent the symmetric bands, i.e., bands in presence of nearest neighbour in-plane ( $\gamma_0$ ) and interplane ( $\gamma'_1$ ) hopping energies. In (a) the dashed curves contain informations due to the presence of sublattice asymmetry ( $\Delta$ ), clearly visible from the lower panel; in (b) the dashed curves have the effect of nearest neighbour in-plane ( $s_0$ ) and interplane ( $s'_1$ ) overlap integrals but zero $\Delta$ , whereas the dotted curves are plotted with non-zero values of $s_0, s'_1$ and $\Delta$ . Effects of these parameters at the $K$ point are visible from the lower panel. In (c) the bands in presence of finite values of $s_0, s'_1$ and $\Delta$ (dashed curves) are compared with the symmetric bands (full curves) over the whole brillouin zone (upper panel) and nearer to the $K$ point within optical energy range (lower panel). The relevant parameters are given in rows numbered 1 and 2 in Table 3.3. . . . .	51

- 3.6 Electronic dispersions of bilayer graphene in presence of nearest neighbour in-plane and interplane transfer integrals (full curves), nearest neighbour in-plane and interplane transfer integrals, overlap integrals and sublattice asymmetric energy (dashed curves), in-plane next nearest neighbour interactions (dotted curves) and in-plane next to next nearest neighbour interactions (triangles). The parameters used for these bands are given in Table 3.3. The rows numbered 1, 2, 3 and 4 in the table correspond to the curves with full lines, dashed lines, dotted lines and triangles respectively in the figure. . . . . 54
- 3.7 Electronic spectra of graphite. The upper panel shows the bands along all the high symmetry directions of the graphite brillouin zone and in the lower panels we have shown the zoomed versions of the spectra near the brillouin zone corners ( $K$  and  $H$  points). In all the panels the full curves represent the symmetric bands, i.e., bands in presence of nearest neighbour in-plane ( $\gamma_0$ ) and interplane ( $\gamma'_1$ ) hopping energies. In (a) the dashed curves contain informations due to the presence of sublattice asymmetry ( $\Delta$ ), nearest neighbour in-plane ( $s_0$ ) and interplane ( $s'_1$ ) overlap integrals. Effects of these parameters at and around the  $K$  and  $H$  points are visible from the lower panel (in (b) and (c) respectively). The relevant parameters are given in rows numbered 1 and 2 in Table 3.3. . . . . 57
- 3.8 Electronic dispersions of graphite in presence of nearest neighbour in-plane and interplane transfer integrals (full curves), nearest neighbour in-plane and interplane transfer integrals, overlap integrals and sublattice asymmetric energy (dashed curves), in-plane next nearest neighbour interactions (dotted curves) and in-plane next to next nearest neighbour interactions (triangles). The parameters used for these bands are given in Table 3.3. The rows numbered 1, 2, 3 and 4 in the table correspond to the curves with full lines, dashed lines, dotted lines and triangles respectively in the figure. . . 58

3.9	Density of states of graphene (a) with nearest neighbour hopping but zero overlap integral (full curve) and with nearest neighbour hopping and overlap integral (dashed-dotted curve), (b) derived from the bands in fig. 3.3 (parameters are in Table 3.1). First principle result (full curve), first nearest neighbour interactions (dashed-dotted curve), second nearest neighbour interactions (dotted curve) and third nearest neighbour interactions (dashed curve) and (c) calculated from the bands plotted in fig. 3.4 (parameters are in Table 3.2). First principle result (full curve), first nearest neighbour interactions (dashed-dotted curve), second nearest neighbour interactions (dotted curve) and third nearest neighbour interactions (dashed curve). . . . .	59
3.10	Density of states of bilayer graphene in presence of nearest neighbour in-plane and interplane transfer integrals (full curves), nearest neighbour in-plane and interplane transfer integrals, overlap integrals and sublattice asymmetric energy (dashed curves), in-plane next nearest neighbour interactions (dotted curves) and in-plane next to next nearest neighbours (triangles). The parameters used in these curves are given in Table 3.3. . . . .	60
3.11	Density of states of graphite in presence of nearest neighbour in-plane and interplane transfer integrals (full curves), nearest neighbour in-plane and interplane transfer integrals, overlap integrals and sublattice asymmetric energy (dashed curves), in-plane next nearest neighbour interactions (dotted curves) and in-plane next to next nearest neighbours (triangles). The parameters used in these curves are given in Table 3.3. . . . .	61
4.1	(a) The raw photoemission data from single crystal graphite along the $\Gamma K$ direction of its Brillouin zone. Shown in the inset is the two dimensional Brillouin zone of graphite. The emission angles $\theta$ and $\phi$ (in degree) for some of the spectra are indicated beside the spectra. In (b) the photoemission intensity plot as a function of binding energy and $k_{\parallel}$ derived from the spectra in (a) is shown. The spectra along the cut A of the Brillouin zone through the $K$ point over a small energy range near Fermi energy are shown in (c). In (d) the spectra over a very small energy range at the $K$ point at two different temperatures (300 K (black curve) and 77 K (red curve)) are compared. . . . .	74
4.2	The low energy electron diffraction pattern of single crystal graphite. . . . .	75

- 4.3 (a) The spectra along the  $\Gamma M$  direction of graphite Brillouin zone. The emission angles in degree for some of the spectra are marked beside the spectra. (b) The intensity map of the spectra shown in (a) as a function of binding energy and  $k_{\parallel}$ . . . . . 76
- 4.4 Energy versus momentum component parallel to the sample surface ( $E(k) \sim k_{\parallel}$ ) for all the strong (red circles) and weak (green circles) peaks of the experimental results in figs. 4.1(a) and 4.3(a). They have been plotted along with a theoretical band structure (black circles) of graphite in the  $\Gamma K$  and  $\Gamma M$  directions of the Brillouin zone. . . . . 77
- 4.5 The red and green circles represent the strong and weak features respectively from ARPES experiment, the black curves are calculated tight binding bands due to nearest neighbour in-plane and interplane hopping ( $\gamma_0$  and  $\gamma'_1$ ) only and the blue curves are obtained by considering both the hopping and overlap integrals along with the coupling up to in-plane third nearest neighbours. . . . . 77
- 4.6 (a) The angle resolved photoemission spectra of HOPG along a radial direction of the circular Brillouin zone (along the arrow shown in inset); the low energy electron diffraction pattern of HOPG was taken at room temperature with a beam energy of 165 eV. The circular pattern, instead of six distinct spots as in single crystal graphite, shows its quasi crystalline structure. Since different symmetry directions of the Brillouin zone get averaged out, all the radial directions become equivalent. (b) The intensity plot of the photoemission spectra shown in (a). . . . . 80
- 4.7 Spectra of HOPG along the same direction as in fig. 4.6 over different energy ranges: (a) shows the spectra at the  $\Gamma$  point (black curve) and at the zone boundary (red curve) over an energy range of  $\sim 11$  eV, (b) shows a set of spectra at and around the zone boundary over an energy range of  $\sim 5$  eV, in (c) the spectra at  $K$  point (red curve) and slightly away from the  $K$  point (black curve) of the Brillouin zone over the energy range of  $\sim 3$  eV are compared. The  $K$  point spectra shows the appearance of a small peak very close to the Fermi energy. The dispersion of this peak for some nearby angles is shown in (d) where the spectra are taken over an energy range of 0.5 eV, the same taken at a temperature of 77 K is shown in (e). . . 81

4.8	(a) The $k$ -resolved inverse photoemission spectra of HOPG along a radial direction; (c) the same taken on single crystal graphite along the direction shown in inset. It is $\sim 17^\circ$ away from the $\Gamma - M$ direction of the Brillouin zone of graphite. The spectra were taken at an interval of $5^\circ$ . For clarity, polar angle of incident electrons referred to the surface normal for some of the spectra are marked beside. All the strong (red circles) and weak (green circles) peaks of the experimental results in (a) and (c) have been plotted in (b) and (d) respectively along with the theoretical (black circles) unoccupied bands of graphite calculated by Holzwarth et al [30] in the $\Gamma - M$ direction of the Brillouin zone. . . . .	83
5.1	Valence Band Spectra of the $\text{Bi}_{1-x}\text{Pb}_x\text{FeO}_3$ ( $x = 0.02$ to $0.15$ ) samples taken at room temperature by using Al $\text{K}_\alpha$ X-rays. The spectra corresponding to the $x = 0.125$ and $0.15$ shift towards lower binding energy, possibly due to increase in metallicity. . . . .	90
5.2	O 1s XPS spectra of the $\text{Bi}_{1-x}\text{Pb}_x\text{FeO}_3$ ( $x = 0.02$ to $0.15$ ) samples taken by using Al $\text{K}_\alpha$ X-rays at room temperature. The spectra corresponding to the $x = 0.125$ and $0.15$ shift towards lower binding energy. . . . .	91
5.3	Valence Band spectra of the $\text{Bi}_{1-x}\text{Pb}_x\text{FeO}_3$ ( $x = 0.02$ to $0.15$ ) samples taken by using He I photons at room temperature. The cubic composition $x = 0.15$ shows the presence of an additional feature at $\sim 3$ eV below the $E_F$ . . . . .	92
5.4	Valence Band spectra of the $\text{Bi}_{1-x}\text{Pb}_x\text{FeO}_3$ ( $x = 0.02$ to $0.15$ ) samples taken at 77 K by using He I photons. Inset: Comparison of the spectra of $x = 0.15$ sample taken at 300 K, 150 K and 77 K. . . . .	93
6.1	Phase diagram of $\text{Sm}_{0.1}\text{Ca}_{0.9-x}\text{Sr}_x\text{MnO}_3$ samples determined from magnetic and transport measurement (taken from reference [6]). . . . .	99
6.2	Angle integrated valence band photoemission spectra from the different compositions of the $\text{Sm}_{0.1}\text{Ca}_{0.9-x}\text{Sr}_x\text{MnO}_3$ system taken at room temperature by using He I photons. Intensities of all the spectra are normalized and shifted along the ordinate axis by a constant value for clarity of presentation. 100	

- 6.3 Valence band resonant photoemission spectra of  $\text{Sm}_{0.1}\text{Ca}_{0.9-x}\text{Sr}_x\text{MnO}_3$  for  $x = 0.0$  composition. In the inset the  $MnL$  edge x-ray absorption spectrum (XAS) is shown. The photon energies used to probe the resonant valence band are marked by black circles in the XAS spectrum. Off- and on- resonance spectra are mentioned. Various peaks appearing in the on-resonance spectrum have been indicated by A, B, C, D, E and F respectively. . . . . 101
- 6.4 The difference spectra obtained from the on and off resonance spectra corresponding to the compositions  $x=0.2, 0.3, 0.4$  and  $0.6$  are shown. The spectra have been given constant shifts along y-axis for clarity of presentation. . . . . 102

Graphite, a typical layered material, consists of hexagonal carbon sheets which are stacked on top of each other. Each layer contains two interpenetrating triangular sublattices denoted as A and B. Elemental carbon is tetravalent. Its  $2s$  and  $2p$  electrons hybridize with each other leading to the formation of strong  $\sigma$  bond and the sidewise overlap of  $p_z$  electrons gives rise to  $\pi$  bonds. The  $\sigma$ -bonded electrons are at the root of the hexagonal structure of each layer of graphite whereas the  $\pi$ -bonded electrons are of vital importance for its various electronic properties. The interaction between the  $\pi$  electrons in two consecutive layers is very small compared to the in-plane interaction. This difference in two directions makes graphite a quasi-two-dimensional system, the layers of which could be peeled off easily. Exploring this characteristic, to avoid many experimental complications, the momentum resolved electronic structure of graphite has been studied extensively in the past using angle resolved photoelectron spectroscopy. There have been many band structure calculations also of graphite. Recently, the discovery of the two-dimensional system, graphene with its peculiar electronic structure in which charge carriers mimic massless fermions, has created a renewed interest in the mother system, graphite. Moreover, some of the exotic properties like room temperature ferromagnetism (FM), quantum Hall effect (QHE) in Highly Oriented Pyrolytic Graphite (HOPG) and the M-I like behaviour of graphite have enhanced the necessity to reinvestigate the electronic structure of graphite. Recent angle resolved photoelectron spectroscopic experiments have lead to several new observations, e.g., massless electronic charge carriers (Dirac fermions) coexisting with quasiparticles having finite effective mass, presence of non-dispersive band very close to Fermi energy which was neither predicted by band calculations and strong electron-phonon coupling along with linear energy dependence of the quasiparticle scattering rate indicating a deviation from the Fermi-liquid behaviour of quasiparticles in graphite.

Electron spectroscopy is a very powerful experimental tool for probing the electronic structure, bonding and chemical nature of a material. Angle resolved photoelectron spectroscopy (ARPES) is of particular interest because it provides the advantage of directly probing the electronic structure with both energy and momentum information which is not accessible by any other measurement. Ultra violet photon is used to probe the occupied band structure. On the other hand, angle resolved inverse photoelectron spectroscopy in which energetic electrons are used as the probing agent, is the most direct technique to elucidate the momentum resolved unoccupied electronic structure of a material. More-

over, the introduction of high energy resolution to these techniques enables one to probe directly the most crucial low-energy excitations near the Fermi level ( $E_F$ ). It can give valuable information regarding the quasiparticle lifetime and strength of various interactions like electron-electron, electron-phonon and so on inside a solid. For this thesis we have used Angle resolved photoelectron spectroscopy (ARPES) and  $k$ -resolved inverse photoelectron spectroscopy (KRIPES) techniques to probe the valence and conduction band structure of single crystal graphite and HOPG along the different high symmetry directions of their Brillouin zone.

We have carried out a comparative study of the near Fermi-level electronic structure of single crystal graphite and highly oriented pyrolytic graphite (HOPG). Angle resolved photoelectron spectroscopy and angle resolved inverse photoelectron spectroscopy have been used to probe the occupied and unoccupied electronic states, respectively. The single crystal graphite showed distinctive band dispersions along the symmetry directions  $\Gamma K$  and  $\Gamma M$  of its hexagonal Brillouin zone. We compared these dispersing features with the existing first principle band structure calculations to identify the experimental bands and found them to be in good agreement. All along the symmetry directions only one  $\pi$  band is visible but near the  $K$  point (Brillouin zone corner) the  $\pi$  bands of single crystal graphite show a splitting. The splitting at the  $K$ -point was estimated to be  $\sim 0.5$  eV. We have also compared the dispersing  $\pi$  bands with another band structure calculation performed by us within tight binding model with much importance on the in-plane interactions among the electrons. In the following paragraph we will describe the outline of the formalism and compare the experimental results with that. We have done a low temperature (77K) study of the near  $E_F$  feature at the  $K$  point and observed the presence of a quasiparticle peak below  $E_F$  which indicates a strong electron-phonon coupling in graphite. On the other hand, HOPG showed a circular low energy electron diffraction (LEED) image consistent with the presence of microcrystalline grains in the material. In ARPES experiment on HOPG, the  $M$  and  $K$  points like features were found to be present in the same radial direction due to the superposition of the  $\Gamma M$  and  $\Gamma K$  directions. Angle resolved inverse photoemission spectroscopy, which gives the dispersions of the conduction band states, have been carried out on single crystal graphite (along a Brillouin zone direction very close to  $\Gamma M$ ) and on HOPG (along a radial direction). Results from this spectroscopy have displayed band dispersions which are matching with the lower  $\pi^*$  band along the  $\Gamma M$  direction of the calculated conduction band structure. We have also found the presence of some non-dispersive features in both the valence and conduction bands which are thought

to be coming from the presence of loose carbon atoms at the surface or from the high density of states due to the flat band near the  $M$  point.

Since singly occupied  $p_z$  electrons are responsible for the electronic properties of graphite, we have particularly compared the experimentally found  $\pi$  bands with our tight binding  $\pi$  bands on graphite. To calculate the bands we have initially constructed the formalism for graphene which could be thought as the first approximation of graphite. We have calculated the bands considering the hopping of the electrons up to third nearest neighbours in the graphene plane with an aim to find a set of parameters which will not be mere fitting parameter, rather have some physical ground, e.g. the parameters should be decreasing in magnitude with increasing distance. We have also included the overlap integral corrections to the bands. We find that the  $\pi$  bands are linear near the  $K$  point and the near  $K$  point regions of the dispersions are very little affected by the inclusion of different parameters whereas the slope of the bands change considerably in the region near about the  $\Gamma$  point. We have fixed the values of the parameters by comparing the results with a first principle band structure calculation. We have also produced the partial density of states (due to  $\pi$  band only) within the same model. Furthermore, we have investigated the effects of these in-plane parameters on the  $\pi$  bands of bilayer graphene along with its out-of-plane interaction between the neighbouring planes. Here we have also searched for the effect of the site energy difference ( $\Delta$ ) which comes from the difference in structural environment between two atoms in two different sublattices in the same graphene layer. It is observed that the bands become quadratic in nature near the  $K$  point of bilayer brillouin zone. We also observe that  $\Delta$  introduces asymmetry in energy values of top conduction band and bottom valence band at the  $K$  point with respect to zero energy and the out-of-plane overlap integral introduces further asymmetry to these. In general there is noticeable electron-hole asymmetry in the slope of the bands away from the  $K$  point, and also the changes in band widths due to different in-plane coupling parameters. For this system also we have derived the density of states within the same model. Finally, we have applied this formalism on graphite which is nothing but a bilayer graphene with periodicity along the z-axis. So, the brillouin zone of graphite is also three dimensional. In this system we find that the bands are non-linear near the  $K$  point whereas they are linear near the  $H$  point (another corner at the top) of the brillouin zone. Comparison of the experimental  $\pi$  bands with those of the calculated ones in the  $\Gamma MK$  plane of the brillouin zone reveals that the bands having the effect of parameters up to third nearest neighbours have a better matching near the zone boundaries, i.e. near  $K$  and  $M$  point compared to the bands with nearest neighbour hop-

ping only. At and around the zone centre none of the calculated bands superpose well with the experimental bands.

Though, for this thesis the major work is on graphite system, we have done some electronic structure studies applying the photoelectron spectroscopic methods on two transition metal oxide systems of current interest namely,  $\text{BiFeO}_3$ , a multiferroic material and  $\text{Sm}_{0.1}\text{Ca}_{0.9-x}\text{Sr}_x\text{MnO}_3$ , a colossal magnetoresistive material.

Multiferroic materials are of great interest because of their huge application possibility in magnetic storage devices, electronics, sensor etc. and also from the physics point of view the simultaneous presence of different ferroic orders (magnetic, electric and/or structural) and their coupling mechanism needs to be understood.  $\text{BiFeO}_3$  is of particular interest because its both the transition temperatures ( $T_C$  and  $T_N$ ) are above room temperature. Here, we have studied the valence band electronic structure of Pb doped  $\text{BiFeO}_3$  i.e.,  $\text{Bi}_{1-x}\text{Pb}_x\text{FeO}_3$  ( $x = 0.02$  to  $0.15$ ) system using X-ray (XPS) and ultra-violet photoelectron spectroscopy (UPS). The system undergoes a R3c (distorted cubic perovskite) to cubic phase transition with Pb doping. The cubic composition shows an enhancement of the oxygen 2p character in the near Fermi level density of states, possibly due to the weakening of the Fe 3d - O 2p - Bi 6p hybridization strengths following the changes in the topology of the oxygen octahedra in its structure. The compositions with the R3c structure showed a much larger band gap and band width compared to those reported from LSDA + U calculations. We attribute this to a larger effective Coulomb interaction ( $U_{eff}$ ).

To study the electronic structure of  $\text{Sm}_{0.1}\text{Ca}_{0.9-x}\text{Sr}_x\text{MnO}_3$  which is an electron doped system ( $x=0.0, 0.2, 0.3, 0.4$  and  $0.6$ ) we have used ultra violet photoelectron spectroscopy (UPS) with fixed photon energy (HeI line) and resonance photoelectron spectroscopy (ResPES) with varying photon energy across Mn 2p-3d absorption edge. The manganese based perovskite systems, usually known as manganites, have attracted enormous attention over the last several decades because of their potential application in data storage and because of the richness of physics involved in various interesting phenomena exhibited by them. They show a huge decrease of electrical resistance due to the application of external magnetic field, a phenomenon leading to the name colossal magnetoresistance (CMR). The electronic degrees of freedom e.g. charge, spin, orbital and their interplay show interesting phenomena like charge ordering, orbital ordering, pseudogap formation, phase separation etc. Electronic structure study, particularly the near Fermi level electronic structure could shed light on the nature of the interactions behind these phenomena. The magnetic ground state of the parent compound ( $\text{Sm}_{0.1}\text{Ca}_{0.9}\text{MnO}_3$ ) at low temperatures (below  $T_N=T_c=110\text{K}$ )

comprises of ferromagnetic clusters (FM) embedded in a G-type AFM phase. Compositions with  $x < 0.2$  also show the presence of this FM component. This component is sensitive to the substitution of Sr for Ca. From the combined UPS and ResPES studies we find that the valence band of this material has major contribution from Mn 3d states and there is a strong hybridization between Mn 3d  $t_{2g}$  and O 2p states. The very weak spectral weight around the Fermi energy in the resonant photoemission spectrum is attributed to low density of Mn 3d  $e_g$  electrons in  $\text{Sm}_{0.1}\text{Ca}_{0.9-x}\text{Sr}_x\text{MnO}_3$ ; having only a small fraction of  $\text{Mn}^{3+}$  ( $t_{2g}^3 e_g^1$ ) ions. With strontium doping, the A site cation size increases leading to significant changes in the Mn 3d spectral weight. This indicates that there is a change in Mn 3d - O 2p hybridization strength due to structural modification caused by Sr doping.

## List of Publications

- [1] *Near Fermi Level Electronic Structure of  $Pr_{1-x}Sr_xMnO_3$ : Photoemission study*, P. Pal, M. K. Dalai, **R. Kundu**, M. Chakraborty, B. R. Sekhar and C. Martin; **Phys. Rev. B** **76**, 195120 (2007).
- [2] *Towards Phonon Spectrum of Graphene*, **Rupali Kundu**, arXiv:0710.2077v2 (2007).
- [3] *Pseudogap behavior of phase-separated  $Sm_{1-x}Ca_xMnO_3$ : A comparative photoemission study with double exchange*, P. Pal, M. K. Dalai, **R. Kundu**, B. R. Sekhar and C. Martin; **Phys. Rev. B** **77**, 184405 (2008)
- [4] *Electronic structure of  $Pr_{1-x}Ca_xMnO_3$  system revealed by photoemission and inverse photoemission spectroscopies*, M. K. Dalai, P. Pal, **R. Kundu**, B. R. Sekhar, S. Banik, A. K. Shukla, S. R. Barman, C. Martin, **Physica B**, **405**, (2010), 186-191
- \*[5] *Some factors leading to asymmetry in electronic spectra of bilayer graphene*, **Rupali Kundu**; **Int. Journ. of Mod. Phys. B** **25**, (2011) 1877-1888, DOI: 10.1142/S0217979211100060.
- \*[6] *Tight-binding parameters for graphene*, **Rupali Kundu**; **Mod. Phys. Lett. B** **25**, (2011) 163-173, DOI: 10.1142/S0217984911025663.
- \*[7] *Electronic structure of  $Bi_{1-x}Pb_xFeO_3$  from photoelectron spectroscopic studies*, **R. Kundu**, P. Mishra, B. R. Sekhar, J. Chaigneau, R. Haumont, R. Suryanarayanan and J. M. Kiat; **Solid State Communications** **151**, (2011) 256-258.
- [8] *XPS study of  $Pr_{1-x}Ca_xMnO_3$  ( $x = 0.2, 0.33, 0.4$  and  $0.84$ )*, M. K. Dalai, **R. Kundu**, P. Pal, M. Bhanja, B. R. Sekhar, C. Martin, **Journal of Alloys and Compounds**, **509**, (2011) 7674-7676.
- [9] *Near  $E_F$  Electronic Structure of Graphite from Photoemission and Inverse Photoemission studies*, B. R. Sekhar, **R. Kundu**, P. Mishra, M. Maniraj and S. R. Barman; **AIP Conf. Proc.** **1391**, 50 (2011).
- \*[10] *Electronic Structure of single crystal and highly oriented pyrolytic graphite from ARPES and KRIPES*, **R. Kundu**, P. Mishra and B. R. Sekhar, M. Maniraj and S. R. Barman; **Physica B** **407**, (2012) 827-832.

- [11] *Time evolution of resistance in response to magnetic field: Evidence of glassy transport in  $La_{0.85}Sr_{0.15}CoO_3$* , D. Samal, **R. Kundu**, M. K. Dalai, B. R. Sekhar and P. S. Anil Kumar; **Phys. Status Solidi B**, 1-4 (2012)/DOI 10.1002/pssb.201147551.
- \*[12] *Valence Band Electronic Structure of  $Sm_{0.1}Ca_{0.9-x}Sr_xMnO_3$  from Photoemission and Resonant Photoemission Studies*, **R. Kundu**, P. Mishra, M. K. Dalai, B. R. Sekhar, M. Yablonskikh M. Malvestuto and C. Martin; **to be submitted**.

(\*) indicates papers on which this thesis is based.

# 1

## Introduction

The prime objective of this thesis is to study the electronic structure of graphite systems (single crystal graphite, HOPG, bilayer graphene, graphene) and the transition metal oxides ( $\text{BiFeO}_3$ ,  $\text{Sm}_{0.1}\text{Ca}_{0.9}\text{MnO}_3$ ) using the electron spectroscopic techniques ARUPS, KRIPES, UPS, XPS and ResPES; and tight binding band calculation. In the following we will first introduce the material systems which have been studied here and then describe the structure of the thesis.

### 1.1 $sp^2$ hybridized carbon materials

Carbon based materials are unique in many ways. They share the same chemistry, carbon, but are very different in their structure and properties. Hybridization of atomic orbitals leads to several possible configurations of the electronic states of carbon atoms. Atomic carbon has six electrons with the configuration  $1s^2$ ,  $2s^2$  and  $2p^2$ . The  $1s^2$  orbital contains two strongly bound electrons and they are called core electrons. There are four not so tightly bound electrons in  $2s^2 2p^2$  orbitals which are called valence electrons. Since the energy difference between the  $2s$  and  $2p$  energy levels is small, the electronic wave functions of these four electrons can mix with each other and give rise to various hybridized orbitals depending on the contributions from  $s$  and  $p$  orbitals.

#### 1.1.1 Graphite

Graphite is a system with  $sp^2$  hybridization. It has a three dimensional layered structure. Each of these layers consists of carbon atoms arranged in a honeycomb structure. The hexagonal planar arrangement occurs due to  $sp^2$  hybridization. In  $sp^2$  hybridization  $2s$

orbital overlaps with  $2p_x$  and  $2p_y$  orbitals and generates three new in-plane hybridized orbitals each having one electron. Due to overlap of  $sp^2$  orbitals of adjacent carbon atoms strong bonding and antibonding  $\sigma$  bonds are formed. The bonding  $\sigma$  bonds make an angle of  $120^\circ$  among each other and lies in a plane forming hexagonal structure. The singly occupied  $2p_z$  orbitals remain unaltered. The  $p_z$  orbitals are perpendicular to the hexagonal plane and forms bonding and antibonding  $\pi$  bonds due to their overlap in a sidewise fashion. In crystalline phase  $sp^2$  orbitals with a lower binding energy compared to  $1s$  (core level) are called semi core levels and  $p_z$  orbitals having lowest binding energy are the valence levels. The electronic properties of graphite are controlled by  $p_z$  electrons. Further, the in-plane interatomic distance in graphite is much less compared to that between adjacent planes. Hence, the lateral overlap of the  $p_z$  orbitals is very strong in comparison to the longitudinal overlap which results in a very weak coupling between the two layers of graphite. Moreover, the layers could be stacked together in various ways leading to the formation of AA, AB (Bernal) and ABC (rhombohedral) stacked graphite. Because of its weakly coupled layered structure, the surface planes can easily be peeled off. This quality makes graphite a very suitable material for its electronic structure to be studied by angle resolved photoelectron spectroscopy. In fact, using angle resolved photoelectron spectroscopy there have been intensive studies of its electronic structure in the past [1–6]. There have been many band structure calculations [7–13] also on graphite. Earlier band structure calculations also predicted the presence of non-linear dispersion near the  $K$  point, i.e., electrons with finite effective mass and linear dispersion near the  $H$  point, i.e., massless fermions in the same graphite system. But until very recent measurements the coexistence of massive and massless fermions remained unrevealed experimentally [19]. The recent discovery of the two-dimensional system, graphene with its peculiar electronic structure in which charge carriers mimic massless fermions, has created a renewed interest in the mother system, graphite. Moreover, some of the exotic properties like room temperature ferromagnetism (FM), quantum Hall effect (QHE) in Highly Oriented Pyrolytic Graphite (HOPG) and the metal-insulator (M-I) like behaviour of graphite have enhanced the necessity to reinvestigate the electronic structure of graphite. Recent angle resolved photoelectron spectroscopic experiments have lead to several new observations, e.g., massless electronic charge carriers (Dirac fermions) coexisting with quasiparticles having finite effective mass, presence of non-dispersive bands very close to Fermi energy which are neither predicted by band calculations and strong electron-phonon coupling along with linear energy dependence of the quasiparticle scattering rate indicating a deviation from the Fermi-liquid behaviour of

quasiparticles in graphite, presence of a sharp quasiparticle peak in HOPG [14–19].

**HOPG:** Highly oriented pyrolytic graphite is also three dimensional graphite but it is not a perfect single crystal. It has many microcrystal grains with the c-axes being highly oriented (within  $\sim 0.3^\circ - 0.4^\circ$ ). Though this system is characterized by orientationally disordered domains, it shows distinct dispersions in the radial directions along with clear evidence of a sharp quasiparticle peak near the Fermi energy [18].

### 1.1.2 Graphene

Graphene is a one atom thick sheet of hexagonally arranged carbon atoms. It is an ultimate two dimensional material which was once thought to be nonexisting in reality because of large thermal fluctuation. But its existence became an experimental success in 2004 [20]. It has hexagonal brillouin zone, the corners of which are called  $K$  points and the middle of each side is known as the  $M$  point. Near the  $K$  points graphene exhibits unique properties such as the Dirac-like spectrum that derives from its honeycomb lattice structure, the effective fermion velocity being 300 times less than the velocity of light. Actually, the relativistic behaviour of the electrons in graphene was first predicted in 1947 by Philip Russell Wallace [21]. At that time, since nobody believed that a one-atom-thin solid could exist, Wallace rather used the graphene model as his starting point to study graphite. Technologically this material is of great importance in the field of high speed electronics, sensors and energy storage devices.

### 1.1.3 Bilayer graphene

Bilayer graphene is a system of two graphene sheets stacked together. Among all the carbon based materials of recent interest, bilayer graphene is of major practical importance because this is the only two dimensional material in which the band gap between valence and conduction bands can be monitored by applying an external electric field perpendicular to the layers [22–27] or by chemical doping of one of the layers [28]. This makes it a potential candidate for future application in nanoelectronics. The most common and distinctive difference in the electronic features of single-layer and bilayer graphene is that the charge carriers in this material are massive and they behave similar to conventional nonrelativistic electrons. This is caused due to the presence of interlayer coupling in Bernal stacked bilayer graphene.

## 1.2 Transition metal oxides

Transition metal oxides, apart from their unexpected insulating behaviour, exhibit a number of fascinating physical properties like high temperature superconductivity, colossal magnetoresistance (CMR), multiferroicity etc. and fall in the category of strongly correlated electron systems. Because of the inherent richness of physics involved in their properties and large possibility of application in technology, they have attracted considerable attention since last few decades.

### 1.2.1 Multiferroics

Multiferroics are a class of materials which show simultaneous existence of both magnetic, ferroelectric (FE) and/or ferroelastic orders in the same phase. They have the possibility to control the magnetic response by applying electric field and vice versa [29]. Recently, a huge interest has emerged regarding the multiferroics since they are technologically very promising for the construction of multifunctional devices in the field of spintronics and sensors. In general they have a distorted cubic perovskite structure with the general formula  $ABO_3$  where A (Bi, Pb) is rare earth ion and B (Fe, Mn, V) is transition metal ion with much less ionic radius compared to the A-site ion. Among all the multiferroic materials,  $BiFeO_3$  is the most studied one. There is a co-existence of antiferromagnetic (AFM) and FE orders in  $BiFeO_3$ . At room temperature it has a distorted perovskite structure with  $R3c$  symmetry where the  $Bi^{3+}$  and  $Fe^{3+}$  ions are displaced relative to the oxygen octahedra [30]. Also both of its ferroelectric curie temperature ( $T_C$ ) and antiferromagnetic Néel temperature ( $T_N$ ) are above room temperature. At  $T_C$  this material undergoes a first order structural phase transition from FE ( $R3c$ ) to paraelectric (PE) ( $P2_1/m$ ) which is accompanied by a strong tilting of the  $FeO_6$  octahedra. This tilting of the oxygen octahedra results in significant electronic re-arrangements of the chemical bondings, especially the Fe - O bond lengths and Fe - O - Fe bond angles [30]. Partial substitutions of Bi by other elements were also found to result in the tilting of the oxygen octahedra leading to enhanced or suppressed multiferroic properties [31]. Pb substitution for Bi was expected to modify the magnetic and FE properties as Pb ion has similar electronic structure as Bi ion, especially the lone pair electrons, Further, the difference in the charge and ionic radii of  $Bi^{3+}$  and  $Pb^{2+}$  can also lead to topological changes in the oxygen octahedra. It is found that Pb substitution reduces the rhombohedral distortion and progressively breaks the ferroelectric order [32].

## 1.2.2 Manganites

The other class of transition-metal oxides, the colossal magnetoresistance (CMR) materials, also have cubic perovskite structures with the B-site ion being a manganese one. They are very often called manganites because the manganese ion is a key ingredient of these compounds. The term colossal magnetoresistance (CMR) essentially means a huge decrease in electrical resistivity in presence of an external magnetic field. Magnetoresistance is defined by the following equation:

$$MR = 100 \times \frac{\rho(H) - \rho(H = 0)}{\rho(H = 0)}$$

where  $\rho(H)$  is the resistivity in presence of the external magnetic field  $H$ . A wide variety of intriguing phenomena like many types of magnetic ordering, metal-insulator transition, charge and orbital ordering and pressure induced phase transitions etc. are observed by doping the trivalent rare earth (La, Pr, Nd) site with a divalent alkaline earth element (Sr, Ca, Ba) [33]. The undoped parent compound is usually an insulator whereas at low temperatures, properly doped manganites exhibit ferromagnetic metallic or nearly metallic behaviour but at high temperatures they exhibit a paramagnetic insulating behaviour [34]. A qualitatively correct picture of the colossal magnetoresistive effect is given by the double exchange mechanism developed by Zener, DeGennes, Anderson and Hasegawa [35–37]. According to this mechanism, the alignment of adjacent localized  $t_{2g}$  spins on  $Mn^{3+}$  and  $Mn^{4+}$  governs the dynamics of  $e_g$  electrons. However, it can not explain the behaviours of manganites quantitatively. So there are several theories depending on the mechanisms such as electron-phonon interaction, charge and orbital ordering, phase separation etc. The  $Sm_xCa_{1-x}MnO_3$  series shows phase separated behaviour i.e, existence of ferromagnetic domains embedded in an antiferromagnetic matrix over a very small doping range and the ferromagnetic component is maximum near  $x=0.1$  [38]. Further, the nature of phase separation and magnitude of the ferromagnetic component is greatly affected by the A-site cationic size. By substituting Sr for Ca the A-site cationic size is increased in the compound  $Sm_{0.1}Ca_{0.9-x}Sr_xMnO_3$ . The manganese valence state of the series  $Sm_{0.1}Ca_{0.9-x}Sr_xMnO_3$  remains constant at +3.9 irrespective of the doping concentration. At low temperature ( $T < 100$  K) the parent compound  $Sm_{0.1}Ca_{0.9}MnO_3$  shows phase separated behaviour with ferromagnetic domains embedded in a  $G$  type antiferromagnetic matrix and at lower temperature the ferromagnetic domains percolate leading to a more metallic behaviour. This

ferromagnetic component is very sensitive to Sr for Ca substitution. It is almost washed away as soon as  $x$  reaches a value of  $\sim 0.2$  [39].

### 1.3 Structure of the thesis

The thesis is arranged as follows. In *chapter two* the experimental techniques used in this thesis have been discussed along with a brief description of the theory of photoemission and the basic principles of inverse photoemission and resonance photoemission. Brief description of the vital parts of instruments used have also been given.

*Chapter three* is devoted to the electronic band structure calculation of graphite using tight binding description. First, the bands of graphene and bilayer graphene have been calculated within tight binding model to develop the methodology and to determine the parameters to be used for graphite band calculation. In these calculations focus has been given only on the  $\pi$  bands because the  $\pi$  electrons play the key role for the manifestations of the interesting electronic behaviours in these systems. Further, the tight binding model is suitable here because the  $p_z$  orbitals almost keep their atomic character due to small overlap among themselves.

The occupied and unoccupied electronic band structure of single crystal graphite and highly oriented pyrolytic graphite as measured by ARUPS and KRIPES have been presented in *chapter four*. A comparison of the experimentally found bands with the calculated ones have also been shown in this chapter. The splitting between two  $\pi$  bands of graphite at the  $K$  point has been estimated.

The general features of the valence electronic structure of  $\text{Bi}_{1-x}\text{Pb}_x\text{FeO}_3$  from XPS measurements and the near Fermi energy ( $E_F$ ) electronic behaviour using UPS have been discussed in *chapter five*.

*Chapter six* consists of the study of near  $E_F$  electronic behaviour of the manganite sample  $\text{Sm}_{0.1}\text{Ca}_{0.9-x}\text{Sr}_x\text{MnO}_3$  using high resolution photoemission experiments. The bulk-sensitive Mn  $2p$  -  $3d$  resonant photoemission spectroscopy has also been applied to know the contribution of Mn  $3d$  states in the valence band of this material.

The entire work of this thesis has been summed up in *chapter seven*.

# Bibliography

- [1] W. Eberhardt, I. T. McGovern, E. W. Plummer and J. E. Fischer, *Phys. Rev. Lett.* **44**, 200 (1980)
- [2] A. R. Law, J. J. Barry and H. P. Hughes, *Phys. Rev. B* **28**, 5332 (1983)
- [3] D. Marchand, C. Frétigny, M. Laguës, F. Batallan, Ch. Simon, I. Rosenman and R. Pinchaux, *Phys. Rev. B* **30**, 4788 (1984)
- [4] T. Takahashi, H. Tokailin and T. Sagawa, *Phys. Rev. B* **32**, 8317 (1985)
- [5] A. R. Law, M. T. Johnson and H. P. Hughes, *Phys. Rev. B* **34**, 4289 (1986)
- [6] T. Kihlgren, T. Balasubramanian, L. Walldén and R. Yakimova, *Phys. Rev. B* **66**, 235422 (2002)
- [7] J. C. Slonczewski and P. R. Weiss, *Phys. Rev.* **109**, 272 (1958)
- [8] J. W. McClure, *Phys. Rev.* **108**, 612 (1957)
- [9] L. G. Johnson and G. Dresselhaus, *Phys. Rev. B* **7**, 2275 (1973)
- [10] J. -C. Charlier, X. Gonze and J. -P. Michenaud, *Phys. Rev. B* **43**, 4579 (1991)
- [11] R. F. Willis, B. Fitton and G. S. Painter, *Phys. Rev. B* **9**, 1926 (1974)
- [12] N. A. W. Holzwarth, S. G. Louie and S. Rabii, *Phys. Rev. B* **26**, 5382 (1982)
- [13] R. C. Tatar and S. Rabii, *Phys. Rev. B* **25**, 4126 (1982)
- [14] K. Sugawara, T. Sato, S. Souma, T. Takahashi and H. Suematsu, *Phys. Rev. B* **73**, 045124 (2006)
- [15] K. Sugawara, T. Sato, S. Souma, T. Takahashi and H. Suematsu, *Phys. Rev. Lett.* **98**, 036801 (2007)
- [16] C. S. Leem, B. J. Kim, Chul Kim, S. R. Park, T. Ohta, A. Bostwick, E. Rotenberg, H. -D. Kim, M. K. Kim, H. J. Choi and C. Kim, *Phys. Rev. Lett.* **100**, 016802 (2008)
- [17] A. Grüneis, C. Attaccalite, T. Pichler, V. Zabolotnyy, H. Shiozawa, S. L. Molodtsov, D. Inosov, A. Koitzsch, M. Knupfer, J. Schiessling, R. Follath, R. Weber, P. Rudolf, L. Wirtz and A. Rubio, *Phys. Rev. Lett.* **100**, 037601 (2008)

- [18] S. Y. Zhou, G. H. Gweon, C.D. Spataru, J. Graf, D. -H. Lee, Steven G. Louie and A. Lanzara, *Phys. Rev. B* **71**, 161403(R) (2005)
- [19] S. Y. Zhou, G. -H. Gweon, J. Graf, A. V. Fedorov, C. D. Spataru, R. D. Diehl, Y. Kopelevich, D. -H. Lee, S. G. Louie and A. Lanzara, *Nature Physics* **2**, 595 (2006)
- [20] Novoselov, K. S., A. K. Geim, S. V. Morozov, D. Jiang, Y. Zhang, S.V. Dubonos, I.V. Gregorieva and A. A. Firsov, *Science* **306**, 666 (2004)
- [21] P. R. Wallace, *Phys. Rev.* **71**, 622 (1947)
- [22] Edward McCann, *Phys. Rev. B* **74**, 161403(R) (2006)
- [23] Hongki Min, B.R. Sahu, Sanjay K. Banerjee, A.H. MacDonald, *Phys. Rev. B* **75**, 155115 (2007)
- [24] E. V. Castro, K. S. Novoselov, S. V. Morozov, N. M. R. Peres, J. M. B. Lopes dos Santos, J Nilsson, F. Guinea, A. K. Geim, and A. H. Castro Neto, *Phys. Rev. Lett.* **99**, 216802 (2007)
- [25] J. B. Oostinga, H.B. Heersche, X Liu, A.F. Morpurgo and L. M.K. Vandersypen, *Nature Materials* **7**, 151-157 (2007)
- [26] Y. Zhang, Tsung-Ta Tang, C. Girit, Z. Hao, Michael C. Martin, A. Zettl, Michael F. Crommie, Y. Ron Shen and F. Wang, *Nature* **459**, 820-823 (2009)
- [27] A. H. Castro Neto, F. Guinea, N. M. R. Peres, K. S. Novoselov and A. K. Geim, *Rev. Mod. Phys.* **81**, 109 (2009)
- [28] T. Ohta, A. Bostwick, T. Seyller, K. Horn, and E. Rotenberg, *Science* **313**, 951 (2006)
- [29] Nicola A. Hill, *J. Phys. Chem. B* **104**, 6694 (2000)
- [30] R. Haumont, Igor A. Kornev, S. Lisenkov, L. Bellaiche, J. Kreisel and B. Dkhil, *Phys. Rev. B* **78**, 134108 (2008)
- [31] G. L. Yuan and S. W. Or, *J. Appl. Phys.* **100**, 024109 (2006)
- [32] J. Chaigneau, R. Haumont and J. M. Kiat, *Phys. Rev. B* **80**, 184107 (2009)

- [33] Elbio Dagotto, Takashi Hotta and Adriana Moreo; *Physics Reports* **344**, 1-153 (2001)
- [34] Y. Tokura, A. Urushibara, Y. Moritomo, T. Arima, A. Asamitsu, G. Kido and F. Furukawa; *J. Phys. Soc. Jpn* **63**, 3931 (1994)
- [35] C. Zener; *Phys. Rev.* **82**, 403 (1951)
- [36] P. -G. de. Gennes; *Phys. Rev.* **118**, 141 (1960)
- [37] P .W. Anderson and H. Hasegawa; *Phys. Rev.* **100**, 675 (1955)
- [38] C. Martin, A. Maignan, M. Hervieu and B. Raveau; *Phys. Rev. B* **60**, 12191 (1999)
- [39] C. Martin, A. Maignan, M. Hervieu, S. Hébert, A. Kurbakov, G. André, F. Bourée-Vignerou, J. M. Broto, H. Rakoto, and B. Raquet; *Phys. Rev. B* **77**, 054402 (2008)

# 2

## Experimental Techniques

### 2.1 Photoelectron Spectroscopy:

#### 2.1.1 History of Photoelectron Spectroscopy:

Based on the principle of photoelectric effect there are several techniques, e.g., ultraviolet photoemission spectroscopy (UPS), x-ray photoemission spectroscopy (XPS), angle resolved photoemission spectroscopy (ARPES) and resonance photoemission spectroscopy (ResPES) which come under the common name of photoemission spectroscopy (PES). The photoelectric effect was first discovered by Hertz [1] in 1887 and subsequently observed by Thomson [2] and Lenard [3] in 1899 and 1900 respectively. Within classical theory of electromagnetic radiation this phenomenon remained unresolved. In 1905 [4] Einstein gave a satisfactory explanation of this observation by invoking the concept of quantum nature of light. However, it took a long time for photoelectric effect to get established as a technique to extract interesting and valuable information regarding the states of an electron inside a solid. In 1964 Berglund and Spicer [5] performed photoemission experiment on Cu and Ag and showed that their d bands were in good agreement with the predictions of non-interacting band theory. Though, in the same year Kane [6, 7] argued that momentum dependent electronic structure could be mapped from the angle and energy dependence of photoemission spectra; the early time photoemission experiments were purely angle-integrated studies. Later, in 1974 Smith, Traum and DiSalvo [8–11] first performed the angular dependent band mapping of the layered compounds TaS<sub>2</sub> and TaSe<sub>2</sub>. Kai Siegbahn was awarded the Nobel Prize in Physics in 1981 for his development of electron spectroscopy. In its early days the energy and momentum resolutions were around 100 meV and

2° respectively. This was not sufficient for the study of phenomena like superconductivity, ferromagnetism etc. in a solid because these properties are governed by electrons residing within  $\sim 25$  meV below Fermi energy ( $E_F$ ). Significant progress towards the advancement of photoelectron spectroscopy has led to the state of the art energy and momentum resolutions to reach to the regime of sub-meV [12] and fraction of a degree respectively. The enormous evolution of PES is intimately related with the development of many other experimental techniques, such as the improvement of ultrahigh vacuum (UHV) techniques, the design of electron energy analyzers with high energy resolution, the development of synchrotron radiation, laser based light sources and very low temperature facilities.

### 2.1.2 Principle of photoemission and some of its general aspects

In the most simplified picture, photoemission is described as a photon in-electron out process. In this process a photon with energy  $h\nu$  excites an electron to a higher energy state inside a solid. If the photoexcited electron has sufficient energy to overcome the surface barrier (work function) of the material, it comes out of the solid and is detected by an energy analyzer. In Figure 2.1, the schematic of a photoemission geometry is shown.

The kinetic energy of the photoemitted electron is governed by the following equation:

$$E_{kin} = h\nu - |E_B| - \phi \quad (2.1)$$

where  $h\nu$  is the photon energy,  $E_{kin}$  is the kinetic energy of the photoexcited electron,  $E_B$  is the binding energy of the electron inside the solid and  $\phi$  is the work function, which is the energy required for an electron at  $E_F$  to just escape from the solid. The schematic energy level diagram of photoemission process is depicted in figure 2.2. Depending on the energy of the exciting photon there are broadly two types of photoemission spectroscopy namely, XPS and UPS. As the name suggests, in XPS the energy of the exciting photon lies in the X-ray range. Hence, this technique has the capability to probe electrons from the core levels of a material which helps to determine the chemical species present in a material, its elemental concentrations and the charge states of the elements. On the other hand the energy of the incident photon is chosen in the ultra-violet range in case of UPS. As the photon energy used in UPS is lower compared to that in XPS, it has a higher probability to interact with the valence electrons of the solid. Thus, UPS gives information regarding energy states of the valence electrons. In UPS if the emitted photoelectrons are collected from a large solid angle by the energy analyzer, the angular information of the

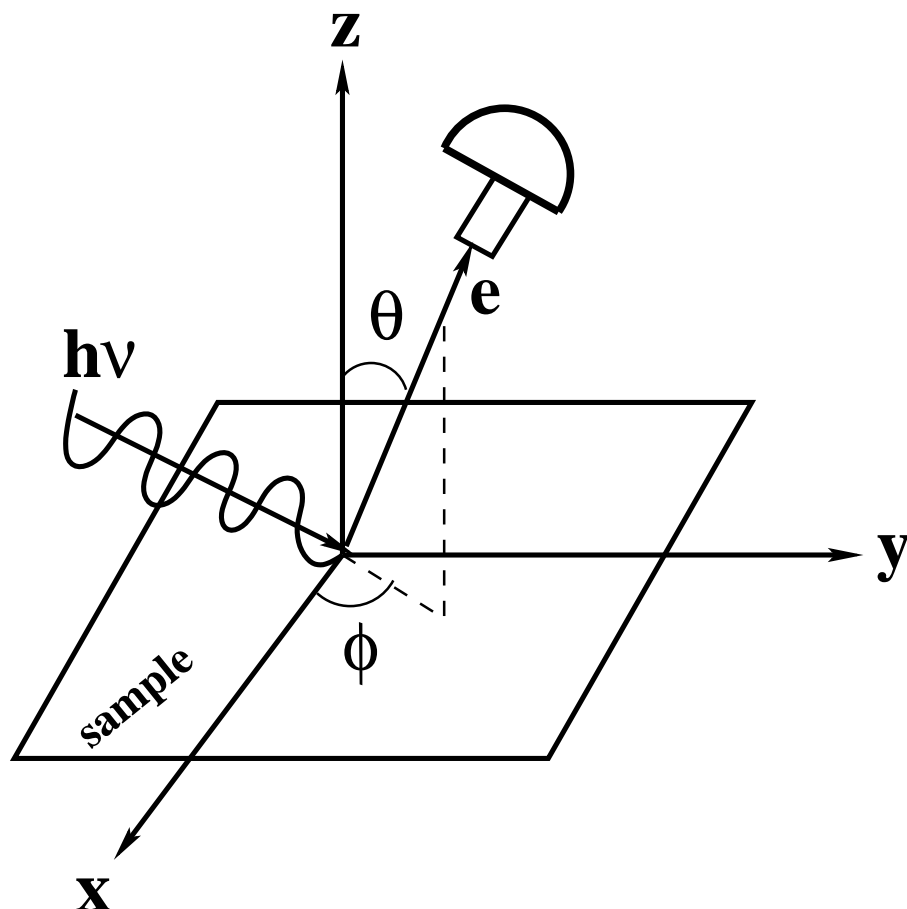


**Figure 2.1:** The schematic of a photoemission experiment. The photoemitted electron is specified by its kinetic energy ( $E_{kin}$ ) and the emission angles  $\theta$  and  $\phi$ . The intensity of the outgoing electrons is measured by the analyzer as a function of ( $E_{kin}$ ).

electrons is lost. The photocurrent is measured as a function of electron kinetic energy and the resulting spectrum is energy distribution curve (EDC). This is technically known as angle integrated ultraviolet photoelectron spectroscopy but is commonly known as only UPS. Since the emission angles of the photoelectrons are not considered, this technique can give information only about the density of states (DOS) of the valence band either of a single crystal or a polycrystalline material but not the momentum ( $k$ ) dependent valence band structure. To obtain momentum resolved energy band of a solid the take off angles of the photoelectrons are also taken care of either by an analyzer with pin hole entrance aperture and EDCs being recorded point by point by moving the analyzer or by a more advanced analyzer with channel plate. This technique is known as angle resolved photoe-

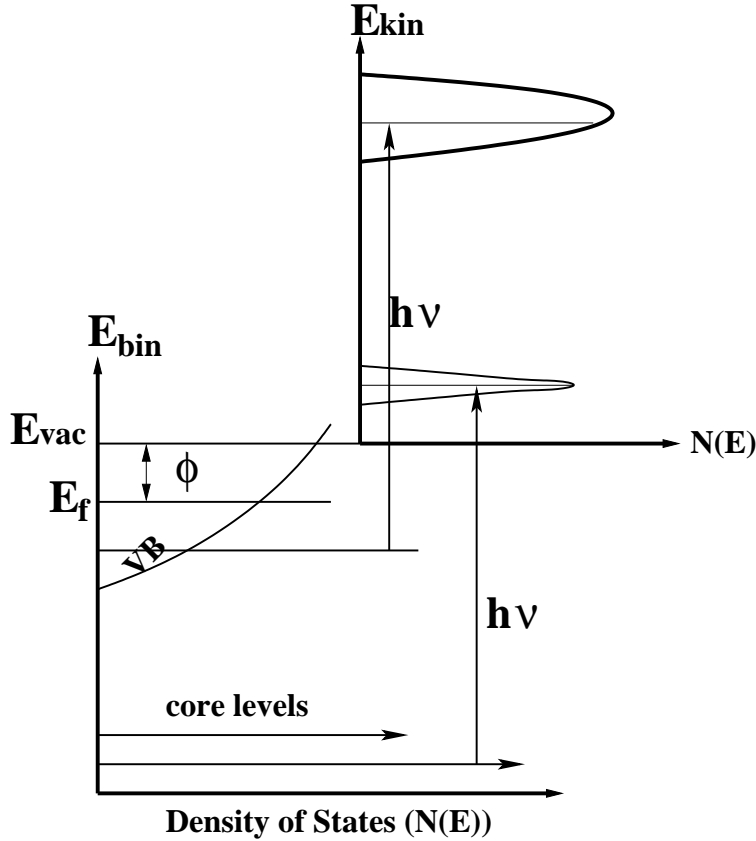


**Figure 2.2:** The schematic energy level diagram of photoemission process.  $E_F$  and  $E_{vac}$  are the Fermi energy and the vacuum level of the system. The intensity of the outgoing electrons is measured as a function of kinetic energy ( $E_{kin}$ ).

mission spectroscopy (ARPES) in general or ARUPS when ultra violet photon is used. The momentum conservation relation which is important in ARPES to obtain the  $k$  dependence of the electronic states along with the energy conservation in equation (2.1), is as follows:

$$\mathbf{k}_i + \mathbf{k}_{h\nu} = \mathbf{k}_f \quad (2.2)$$

where  $\mathbf{k}_i$  and  $\mathbf{k}_f$  are the reduced wave vectors of the electron in its initial and final states respectively inside the solid and  $\mathbf{k}_{h\nu}$  is the wave vector of the incident photon. For low energy photon, used to study the valence band, the momentum of the exciting photon can be neglected when compared with the crystal momentum of the electron in the first Brillouin zone. For example, for the typical photon energy of 20 eV, the photon wave vector ( $2\pi\mathbf{k}_{h\nu}=E/\hbar c$ ) is  $\sim 0.01 \text{ \AA}^{-1}$ , which is less than 1% of the typical size of the reduced bril-

loun zone of graphite or transition metal oxides. Hence, the transition from initial to final state is essentially considered as a vertical one, i.e.,  $\mathbf{k}_i = \mathbf{k}_f$ . Moreover, like the initial state wave function of the electron, the final state also is a Bloch wave so far the electron resides inside the solid. Therefore, one can write  $\mathbf{k}_f$  as  $\mathbf{k}_f = \mathbf{k} + \mathbf{G}$ , where  $\mathbf{G}$  is the reciprocal lattice vector coming from the periodicity of lattice and  $\mathbf{k}$  is the final state crystal momentum in the reduced brillouin zone. But the photoexcited electron outside the solid is a free electron. Hence, for each  $(\mathbf{k}+\mathbf{G})$  component, there exists the possibility that it can be matched to a travelling wave outside the crystal. Thus, the conservation of the wave vector is given by

$$\mathbf{k}_f = \mathbf{k} + \mathbf{G} = \mathbf{K}, \quad (2.3)$$

$\mathbf{K}$  being the wavevector of the travelling free electron. Combining equations (2.2) and (2.3) we get

$$\mathbf{k}_i = \mathbf{K} \quad (2.4)$$

But due to the discontinuity of the solid because of the presence of its surface the total momentum is no longer conserved, rather only the component parallel to the surface is conserved. Hence, the correct momentum conservation relation is

$$\mathbf{k}_{i\parallel} = \mathbf{k}_{\parallel} + \mathbf{G}_{\parallel} = \mathbf{K}_{\parallel} \quad (2.5)$$

where  $\mathbf{k}_{i\parallel}$ ,  $\mathbf{k}_{\parallel}$ ,  $\mathbf{G}_{\parallel}$  and  $\mathbf{K}_{\parallel}$  are the components parallel to the sample surface of the reduced initial state wave vector  $\mathbf{k}_i$ , the reduced final state wave vector  $\mathbf{k}$ , the reciprocal lattice vector  $\mathbf{G}$  and the external photoelectron wave vector  $\mathbf{K}$  respectively. Since the kinetic energy of the photoelectron is measured experimentally, its total momentum can be calculated from the following equation

$$\hbar^2 K^2 / 2m_e = E_{kin} \quad (2.6)$$

where  $m_e$  is the mass of an electron. According to the geometry in fig. 2.1 and using equation (2.6) the parallel and perpendicular components of the momentum are obtained as

$$K_{\parallel} = \frac{\sqrt{2m_e E_{kin}}}{\hbar} \sin \theta \quad (2.7)$$

$$K_{\perp} = \frac{\sqrt{2m_e E_{kin}}}{\hbar} \cos \theta \quad (2.8)$$

The  $x$  and  $y$  components of  $K_{\parallel}$  are related to the azimuthal angle  $\phi$  in the following way

$$K_{\parallel x} = \frac{\sqrt{2m_e E_{kin}}}{\hbar} \sin \theta \cos \phi \quad (2.9)$$

$$K_{\parallel y} = \frac{\sqrt{2m_e E_{kin}}}{\hbar} \sin \theta \sin \phi \quad (2.10)$$

Once  $K_{\parallel x}$  and  $K_{\parallel y}$  become known, the parallel component of the crystal momentum ( $\mathbf{k}_{i\parallel}$ ) of the electron in its initial state is also known through the relation in equation (2.5). The perpendicular component can not be extracted so easily because it is not a conserved quantity. One has to take special care in order to get information regarding this component. The ARPES work presented in this thesis has dealt only with the parallel component of momentum and hence an elaborate discussion of the procedure to determine the perpendicular component is skipped.

Due to inherent randomness polycrystals do not show a Brillouin zone with well defined high symmetry directions and hence using ARPES polycrystalline materials can not be studied because bands are usually measured along the high symmetry directions of the Brillouin zone of the material. Single crystals, on the other hand, show diffraction images which give the symmetry of the crystal. Though, a part of this thesis is based on the ARPES study of a material which is not a perfect single crystal but very close to a single crystal, it is worthy to mention here that some information of the band structure get lost because of the loss of single crystallinity of the material.

The high surface sensitivity of low energy photoemission spectroscopy is also an important issue to be discussed, particularly when ultraviolet photon and soft X-ray is used. The so called ‘universal curve’ which gives an idea of the inelastic mean free path of the photoexcited electron versus its kinetic energy is shown in fig. 2.3. As seen from the figure, the mean free path lies around or below  $10 \text{ \AA}$  in the kinetic energy range of 20-200 eV, which implies that the PES experiment is a highly surface sensitive technique [29]. So to obtain spectra from clean surfaces, vacuum better than  $10^{-10}$  mbar is mandatory for UV-PES experiments.

### 2.1.3 Theory of photoemission

In photoemission experiment the measured quantity is the photoelectron intensity as a function of the kinetic energy of the emitted electrons. The total intensity of the photoemitted

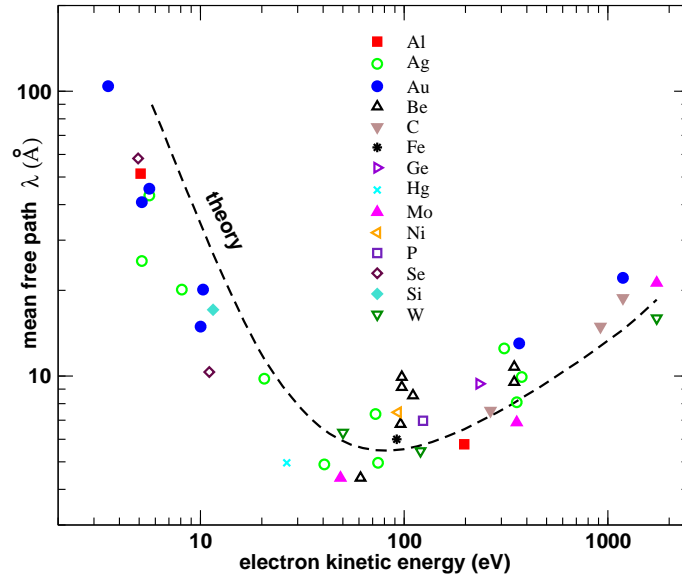


**Figure 2.3:** The universal curve of the electron mean free path versus kinetic energy.

electrons  $I(E, k)$  ( $k$  dependence being taken care of only in ARPES) is a sum of the distribution of primary electrons  $I_p(E, k)$  that have not suffered an inelastic collision and a background of secondary electrons  $I_s(E, k)$  which have suffered an energy loss in one or more collisions. Therefore,

$$I(E, k) = I_p(E, k) + I_s(E, k) \quad (2.11)$$

The background of secondary electrons can be subtracted from the energy distribution curve (EDC) of the photoemitted electrons. To have an idea of the factors contributing to the primary photoelectron intensity, the photoemission process is usually described in the framework of two theoretical models namely, the one-step model and the three-step model. In the one-step model, though the photon absorption, electron removal and electron detection is considered as a single coherent process, it has computational difficulties due to its inherent complexities arising from the involvement of surface vacuum interface and choices of wave functions. Hence, the photoemission process is most often interpreted in terms of the much simpler three-step model [5, 14–16]. Within this approach, the photoemission process is subdivided into three sequential independent steps (Fig. 2.4) such as: (1) the optical excitation of an electron in the bulk, (2) the transport of the excited electron through the solid to the surface and (3) the escape of the electron from the solid surface

into the vacuum. The photoemission intensity ( $I_p(E, k)$ ) is then given by the product of three independent quantities: the total probability for the optical transition ( $P(E, k)$ ), the scattering probability of the electrons while travelling through the solid ( $d(E, k)$ ) and the transmission probability ( $T(E, k)$ ) through the surface potential barrier.

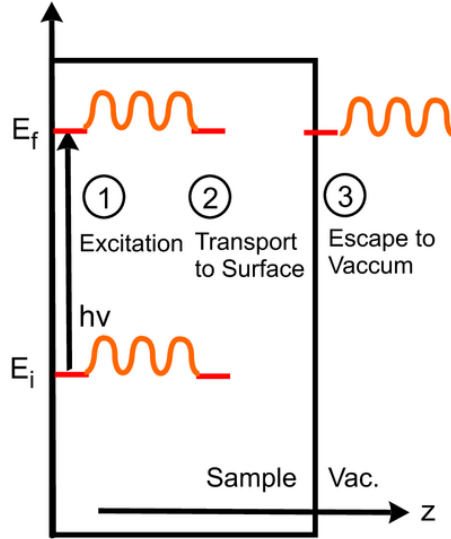


**Figure 2.4:** Illustration of the three-step model of photoemission. It consists of (1) the photoexcitation of an electron in the bulk, (2) its travel through the solid to the surface and (3) its transmission through the surface into the vacuum.

**Step one :** For the first step of this model one has to calculate the transition probability  $w_{fi}$  due to an optical excitation from the  $N$ -electron initial state  $\Psi_i^N$  to one of the possible final states  $\Psi_f^N$ . This can be approximated by Fermi's Golden Rule:

$$w_{fi} = \frac{2\pi}{\hbar} |\langle \Psi_f^N | H_{int} | \Psi_i^N \rangle|^2 \delta(E_f^N - E_i^N - h\nu), \quad (2.12)$$

where  $E_i^N = E_i^{N-1} - E_B^k$  and  $E_f^N = E_f^{N-1} + E_{kin}$  are the energies of the initial and final  $N$ -electron states,  $E_B^k$  is the binding energy of the photoelectron with momentum  $k$  and kinetic energy  $E_{kin}$ . The interaction of the electron with the electromagnetic field of photon is considered as a perturbation. Neglecting the contribution from the quadratic term in vector potential  $\mathbf{A}$ , the interaction Hamiltonian is given by

$$H_{int} = -\frac{e}{2m_e c} (\mathbf{A} \cdot \mathbf{p} + \mathbf{p} \cdot \mathbf{A}), \quad (2.13)$$

$\mathbf{p}$  being the momentum operator,  $e$  and  $c$  are the electronic charge and velocity of light in free space respectively. Further,  $H_{int}$  can be approximated as

$$H_{int} = -\frac{e}{2m_e c} \mathbf{A} \cdot \mathbf{p} \quad (2.14)$$

using the commutator relation  $[\mathbf{p}, \mathbf{A}] = -i\hbar \nabla \cdot \mathbf{A}$  and the dipole approximation  $\nabla \cdot \mathbf{A} = 0$ , i.e.,  $\mathbf{A}$  is constant over atomic dimensions compared to the wavelength of light used. This is not a good approximation because  $\mathbf{A}$  might have a substantial amount of change at the solid surface. For further discussion of the transition matrix element some approximations are required regarding the wave functions contained in it. In the simplest approximation scheme one can take a one-electron view of the initial and final state wave functions. Then the initial state can be written as a product of  $\phi_i^k$ , the state from which the electron with momentum  $k$  is photoexcited and the wave function of the remaining electrons  $\Psi_i^{N-1}$ , i.e.,

$$\Psi_i^N = C \phi_i^k \Psi_i^{N-1}, \quad (2.15)$$

where  $C$  is the operator that antisymmetrizes the wave function properly. In a similar way the final state can also be expressed as

$$\Psi_f^N = C \phi_f^{E_{kin}} \Psi_f^{N-1}, \quad (2.16)$$

where  $\phi_f^{E_{kin}}$  is the wave function of the photoemitted electron and  $\Psi_f^{N-1}$  is the same for the remaining  $(N - 1)$  electrons. The transition matrix element then reduces to

$$w_{fi} = \frac{2\pi}{\hbar} |\langle \phi_f^{E_{kin}} | H_{int} | \phi_i^k \rangle|^2 |\langle \Psi_f^{N-1} | \Psi_i^{N-1} \rangle|^2 \delta(E_f^N - E_i^N - h\nu) \quad (2.17)$$

or

$$w_{fi} = |M_{fi}^k|^2 |c_{fi}|^2 \delta(E_f^N - E_i^N - h\nu), \quad (2.18)$$

where  $|M_{fi}^k|^2 = |\langle \phi_f^{E_{kin}} | H_{int} | \phi_i^k \rangle|^2$  is the one-electron matrix element and  $|c_{fi}|^2 = |\langle \Psi_f^{N-1} | \Psi_i^{N-1} \rangle|^2$  is  $(N - 1)$  electron overlap integral. Basically, this is the probability that the removal of an electron from the  $i^{th}$  state of a  $N$ -electron system leaves the system in any of its excited state  $f$  of the  $(N - 1)$ -electron system. In a real solid many of the  $c_{fi}$  are non-zero which will contribute to the photoemission intensity as additional peaks (called satellites) along

with the main peak. The intensity is then proportional to  $\sum_{fi} w_{fi}$ , i.e.,

$$I_p(E, k) \propto \sum_{f,i} |M_{fi}^k|^2 |c_{fi}|^2 \delta(E_f^N - E_i^N - h\nu) \quad (2.19)$$

**Step two :** The photoexcited electron while travelling towards the surface may undergo collision via several mechanisms like electron-electron, electron-phonon and so on. The dominant scattering mechanism is the electron-electron interaction. Assuming that the scattering frequency  $1/\tau$  ( $\tau$  being lifetime) is isotropic and depends only on energy, the electron inelastic mean free path  $\lambda(E, k)$  is given by

$$\lambda(E, k) = \tau v_g = \frac{\tau}{\hbar} dE/dk, \quad (2.20)$$

where  $v_g$  is the group velocity in the final state. The transmission factor  $T(E, k)$  is calculated in terms of the electron mean free path  $\lambda(E, k)$  and the photon penetration depth  $\lambda_{ph}(\nu)$  by the following equation:

$$T(E, k) = \frac{\lambda(E, k)/\lambda_{ph}(\nu)}{1 + \lambda(E, k)/\lambda_{ph}(\nu)} \quad (2.21)$$

The typical values of  $\lambda(E, k)$  and  $\lambda_{ph}(\nu)$  are  $\sim 5\text{-}20 \text{ \AA}$  and  $100\text{-}1000 \text{ \AA}$ , respectively. Therefore,  $\lambda(E, k)/\lambda_{ph}(\nu) \ll 1$  and  $T(E, k)$  can be replaced by  $\lambda(E, k)/\lambda_{ph}(\nu)$ .

**Step three :** Out of all, the escaping electrons are those for which the contribution to the kinetic energy from the normal component of momentum is sufficient to overcome the surface potential barrier. All other electrons are totally reflected back into the bulk. Approximately, the escape function is defined as

$$\begin{aligned} D(E) = 0 & : E_f(\mathbf{k}) - E_{vac} \leq \hbar^2(\mathbf{k}_{\parallel} + \mathbf{G}_{\parallel})^2/2m_e \\ & = 1 : E_f(\mathbf{k}) - E_{vac} > \hbar^2(\mathbf{k}_{\parallel} + \mathbf{G}_{\parallel})^2/2m_e \end{aligned} \quad (2.22)$$

with  $E_f(\mathbf{k}) - E_{vac} = E_{kin} = \hbar^2(\mathbf{k}_{\parallel} + \mathbf{G}_{\parallel} + \mathbf{K}_{\perp})^2/2m_e$ .

Considering all these three factors of the model together and taking into account the conservation of wave vector, the final expression for  $I_p(E, k)$  is given by

$$I_p(E, k) \propto \sum_{f,i} |M_{fi}^k|^2 |c_{fi}|^2 T(E, k) D(E) \times \delta(\mathbf{k} + \mathbf{G} - \mathbf{k}_i) \delta(\mathbf{k}_{\parallel} + \mathbf{G}_{\parallel} - \mathbf{K}_{\parallel}) \times \delta[E_f(\mathbf{k}) - E_i(\mathbf{k}) - h\nu] \delta[E - E_f(\mathbf{k}) + \phi] \quad (2.23)$$

In the discussion of strongly correlated systems for which the independent-electron approximation is not valid, the interacting electrons are conveniently described using Green's function formalism where the Green's function is related to another quantity called spectral function  $A(k, E)$  in the following manner:

$$A(k, E) = \pi^{-1} \text{Im}\{G(k, E)\} \quad (2.24)$$

It is also found that  $A(k, E)$  has a form which is very similar to the photoemission intensity described above and in fact  $I_p(E, k)$  can be expressed as

$$I_p(E, k) \propto \sum_{f,i} |M_{fi}^k|^2 A(k, E) \quad (2.25)$$

$A(k, E)$  describes the probability of removing (for  $E$  below  $E_F$ ) or adding (to  $E$  above  $E_F$ ) an electron with energy  $E$  and wave vector  $\mathbf{k}$  from (to) the interacting system.

For a non-interacting system with one-electron energy  $E_k^0$ , the Green's function is given by

$$G_0(\mathbf{k}, E) = \frac{1}{E - E_k^0 - i\epsilon} \quad (2.26)$$

where  $\epsilon$  is a very small quantity and

$$A_0(\mathbf{k}, E) = \delta(E - E_k^0) \quad (2.27)$$

which means that the spectral function for a non-interacting system is a  $\delta$ -function centered at  $E = E_k^0$ .

In an interacting electron system the electron energy gets renormalized by the self-energy  $\Sigma(\mathbf{k}, E) = \text{Re}\{\Sigma(\mathbf{k}, E)\} + i\text{Im}\{\Sigma(\mathbf{k}, E)\}$ . The Green's function changes to

$$G(\mathbf{k}, E) = \frac{1}{E - E_k^0 - \Sigma(\mathbf{k}, E)} \quad (2.28)$$

and correspondingly the spectral function gets modified as

$$A(\mathbf{k}, E) = \pi^{-1} \frac{\text{Im}\{\Sigma(\mathbf{k}, E)\}}{[E - E_k^0 - \text{Re}\{\Sigma(\mathbf{k}, E)\}]^2 + [\text{Im}\{\Sigma(\mathbf{k}, E)\}]^2}. \quad (2.29)$$

The real part of the self-energy corresponds to the shift in the energy of the particle (called quasiparticle for interacting system) from its one-electron value, while the imaginary part

is related to the life-time of the quasiparticle.

## 2.2 Inverse Photoelectron Spectroscopy:

In order to investigate the electronic properties of a solid, it is useful to have a knowledge of both the occupied and the unoccupied states near the Fermi level ( $E_F$ ). It has already been discussed that photoelectron spectroscopy probes the occupied electronic states of solid. On the other hand, inverse photoemission spectroscopy (IPES) has emerged as a powerful technique to study the unoccupied electronic states of a solid [17–19]. It can access the otherwise hardly accessible region between the Fermi and the vacuum level of the sample. Hence, photoelectron spectroscopy and inverse photoemission spectroscopy are complementary to each other. But the yield in IPES is very low compared to that of PES as can be seen from the ratio ( $R$ ) of their differential cross-section:

$$R = \frac{(d\sigma/d\omega)_{IPES}}{(d\sigma/d\omega)_{PES}} = \left(\frac{\lambda_e}{\lambda_{h\nu}}\right)^2, \quad (2.30)$$

where  $\lambda_e$  and  $\lambda_{h\nu}$  are the wavelengths of emitted electron and photon in PES and IPES respectively. This ratio is a reflection of the different densities of final states available for the two transitions. In the UV energy range  $R$  is approximately  $10^{-5}$  and in the x-ray range approximately  $10^{-3}$ . The low cross section for emission of photons in IPES is the major reason for a relatively slow development of the technique as compared with PES.

Moreover, compared to other techniques such as appearance potential spectroscopy (APS), x-ray absorption spectroscopy (XAS) which can probe unoccupied electronic states, IPES has the special advantage of resolving the momentum dependence of the empty bands. So, apart from the density of states in its angle-integrated mode it is possible to obtain the  $k$ -dependent band structure from  $k$ -resolved inverse photoemission spectroscopy (KRIPES).

### 2.2.1 Basic principle

As the name suggests, it is a time reversed process of direct photoemission spectroscopy, i.e., it is an electron-in photon-out process. The schematic diagram of a typical experimental arrangement and the energy level diagram of an inverse photoemission process is presented in figure 2.5. An initially free electron with energy  $E_i$  impinges on a solid and occupies an empty electronic state. This electron relaxes to a final unoccupied state at en-

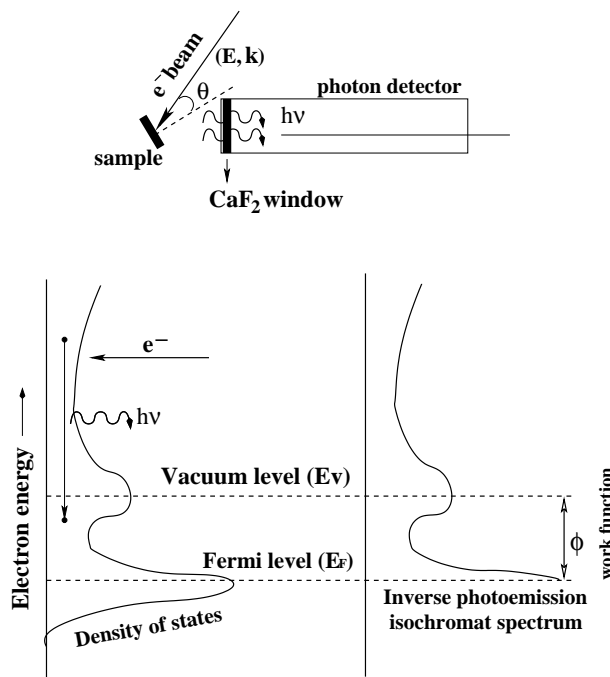


**Figure 2.5:** Illustration of inverse photoemission spectroscopy. The typical experimental arrangement (upper diagram). The energy level diagram of the process (lower diagram). If the measured photon energy is held constant and the incident electron beam energy is swept (isochromat mode), the intensity distribution of photon replicates the density of states of unoccupied electronic states.

ergy  $E_f$  either through radiative or non-radiative transition. When it undergoes a radiative transition with the emission of a photon of energy  $h\nu$ , the intensity of the outgoing photon is measured. This is usually carried out in two ways: (i) the energy of the detected photon  $h\nu$  is held constant and the spectrum is obtained by sweeping  $E_i$  (isochromat mode), and (ii) by fixing the incident electron energy and collecting photons emitted over a range of energies (parallel detection or spectrograph mode). Analogous to the photoemission one can measure an intensity distribution of the emitted photon as a function of the final state energy  $E_f = E_i - h\nu$  by varying the initial state energy  $E_i$  and keeping photon energy  $h\nu$  constant. Within similar approximation schemes, it turns out that this distribution reflects the available number of empty final electronic states above the Fermi level. The interaction Hamiltonian in this case also is same as in direct photoemission (equation 2.14) because both the processes involve interaction of electron with photon. The sampling of the Brillouin zone is determined by the angle of incidence of the electron beam. In the isochromat

mode, the parallel component of the crystal momentum  $k_{\parallel}$  is given by

$$k_{\parallel} = \frac{\sqrt{2m_e}}{\hbar} \sqrt{E_f + h\nu - \phi} \sin \theta, \quad (2.31)$$

where  $\theta$  is the angle of incidence of the electron beam with respect to the surface normal of the sample and  $\phi$  is the work function of the material. In spectrograph mode  $k_{\parallel}$  is given by

$$k_{\parallel} = \frac{\sqrt{2m_e}}{\hbar} \sqrt{E_i - \phi} \sin \theta, \quad (2.32)$$

where the initial energy  $E_i$  is fixed.

### 2.2.2 Instrumentation

The basic experimental requirement of IPES is an electron source providing a well-defined beam and a photon detector with limited bandwidth. The photon detectors used in IPES have fallen into two categories, those which operate in an isochromat or fixed photon energy mode and those that are tunable, allowing detection at different photon energies. The KRIPES results, presented in this thesis, were obtained using a band-pass Geiger-Müller type photon detector with acetone gas filling and  $\text{CaF}_2$  window (acetone/ $\text{CaF}_2$ ) in isochromat mode with a mean photon energy of  $9.9 \text{ eV}$  [20]. A Geiger-Müller counter, as schematically shown in the upper panel of figure 2.5, consists of a tube closed at one end by a calcium fluoride ( $\text{CaF}_2$ ) window and filled with a gas to a certain pressure. The combination of the transmission properties of the window and the photoionization cross section of the gas determines the photon energy detected and the bandwidth. A photon with an energy lower than the cut-off of the window but higher than the ionization potential of the gas will initiate an electron cascade which is collected by a central electrode. For example, the high energy cut-off of the acetone/ $\text{CaF}_2$  detector is due to the  $\text{CaF}_2$  window that does not transmit photons with energy  $> 10.2 \text{ eV}$ , while the threshold for the photoionization of acetone at  $9.7 \text{ eV}$  sets the low energy cut-off. This determines the band-pass function and results in a mean photon detection energy of  $9.9 \text{ eV}$  with a FWHM of  $0.4 \text{ eV}$ . Thus,  $9.9 \pm 0.2 \text{ eV}$  photons can enter the detector to photoionize acetone.

The typical requirements of electron sources for IPES are a large current at low energies with a narrow angular spread in the beam. However, the ability to achieve the requirements of high currents and low energies is restricted by fundamental limits imposed by space-charge effects: the space-charge-limited current density at a cathode varies as the three-

halves power of the extraction voltage and inversely as the square of the cathode-anode distance. A Stoffel-Johnson type [21] electron source was used in our experiment. This is chosen because it has less space-charge effect and high beam current.

## 2.3 Resonance Photoemission Spectroscopy (ResPES)

Resonance photoemission is one of the not so common photoemission techniques and has been used for the investigation of valence band features in transition-metal oxide compounds. Before going into the details of this technique, a brief description of another technique called X-ray absorption spectroscopy (XAS) will be given because to carry out a resonance photoemission experiment, XAS is a prerequisite in order to select the photon energy at which the resonance phenomenon will occur.

### 2.3.1 X-ray Absorption Spectroscopy

X-ray absorption spectroscopy (XAS) is a very powerful technique in the investigation of the unoccupied states as well as the local geometrical structure of a material near an atom. In this method a monochromatic beam of X-rays enters into the solid and may get scattered or absorbed. In the absorption process a core electron is excited to an unoccupied state or to continuum depending on the energy of incident X-rays. Fig 2.6 shows the schematic of X-ray absorption process. When the energy of an incident X-ray photon exceeds the binding energy of a particular core level, the photon can be absorbed, and the core electron is excited to an unoccupied state, leaving a hole in the core-level. Such a core hole may decay through X-ray fluorescence or Auger electron emission. The incident photon intensity  $I_0$  and transmitted photon intensity  $I$  are related as  $I = I_0 \exp^{-\mu x}$  with  $x$  being the sample thickness and  $\mu$  is called the absorption coefficient.  $\mu$  is a function of sample density  $\rho$ , atomic number  $Z$ , atomic mass  $A$  and energy  $E$  of incident X-rays. In XAS, the absorption coefficient  $\mu$  is measured as a function of energy  $E$ . A typical XAS spectrum has several parts. As the photon energy equals with the binding energy of a core level, there is a sharp rise in  $\mu$  which is known as edge and the energy is referred as absorption threshold. The spectral region of a few tens of eV near the threshold is known as near-edge X-ray absorption fine structure (NEXAFS) and the region (upto  $\sim 100$  eV) beyond NEXAFS is known as extended X-ray absorption fine structure (EXAFS). Using X-ray absorption spectroscopy we determined the threshold energy of Mn2p-3d transition in a manganite

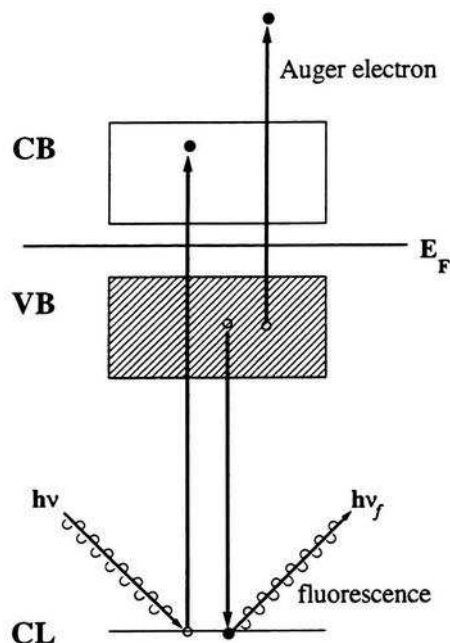


**Figure 2.6:** A schematic diagram of the X-ray absorption process: an electron is excited from the core level (CL) to the unoccupied states in conduction bands (CB) by absorbing a photon with energy  $h\nu$ , leaving a hole in the core level. Such an electron-hole pair may decay through either X-ray fluorescence or emission of Auger electrons.

sample.

There are several techniques for measuring the XAS. The most direct method is to measure the absorption of the sample by monitoring the incoming and the transmitted flux. But this method requires the sample thickness to be very small in case of a large absorption coefficient. By monitoring secondary processes like X-ray fluorescence and Auger electron emission, the absorption can also be measured. A more practical way to measure the absorption is the total-electron yield (TEY) mode, in which all electrons emitted from the sample are collected by an analyzer. The XAS data presented in this thesis were collected in the total electron yield mode.

### 2.3.2 ResPES

In this spectroscopy one excites electrons with photons of energy  $h\nu$  very near to the absorption threshold of a core level. The direct photoemission of valence band electrons can then interfere with the Auger CVV-electrons that are emitted in a Super Koster-Kronig

process. The intensity in the valence band features for which the direct photoemission process and the Auger emission overlap is given as a function of the photon energy  $h\nu$  by the so-called Fano lineshape

$$N(h\nu) \simeq \frac{(\epsilon + q)^2}{(\epsilon^2 + 1)}; \quad \epsilon = \frac{(h\nu - h\nu_j)}{\Delta(h\nu_j)/2} \quad (2.33)$$

where  $h\nu_j$  is a photon energy equal to the binding energy of a core level (near which the resonance is investigated),  $q$  is a parameter for the particular core level and  $\Delta(h\nu_j)$  is the full width at half maxima (FWHM) of that core level.

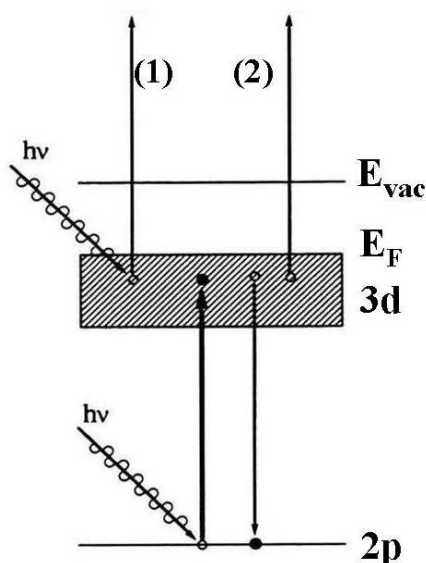


**Figure 2.7:** A schematic diagram for a resonant photoemission process for  $3d$  transition metal compounds.

Fig. 2.7 illustrates the resonant photoemission process of a  $3d$  transition-metal compound at the  $2p$ - $3d$  threshold. In the  $2p$ - $3d$  threshold, in addition to the direct photoemission process (process 1 in the Fig. 2.7):  $3d^n + h\nu \rightarrow 3d^{n-1} + e^-$ , the following atomic process (process 2 in Fig 2.7) takes place.  $3d^n \rightarrow \underline{c}3d^{n+1} \rightarrow 3d^{n-1} + e^-$ , where  $\underline{c}$  denotes a hole in the  $2p$  core level. The first step of such a process is the absorption of a photon, leading to a transition from the  $2p$  core level to the  $3d$  valence band and leaving an intermediate hole state in the  $2p$  core level. The second step is a two-electron Koster-Kronig decay of the intermediate state involving emission of an Auger electron. The above two indistinguishable processes are added coherently due to quantum interference, leading to

an intensity modulation at the  $2p$ - $3d$  threshold.

## 2.4 Instrumentation

The photoemission spectrometric system in our laboratory consists of two OMICRON ultra-high vacuum (UHV) chambers, the main chamber or analysis chamber and a sample preparation chamber. For quick sample loading without breaking the UHV conditions in preparation and analysis chambers a small load lock chamber is attached with the preparation chamber. Further, the sample preparation chamber is equipped with a four-axes manipulator, a diamond file, a sample heater, an evaporator and an Ar ion sputter gun. Samples from the preparation chamber are transferred by using a magnetically coupled transfer rod. The  $\mu$  metal main chamber can protect the photoemitted electrons from earth's magnetic field and any stray magnetic field. The analysis chamber is equipped with the sources of energetic photons (X-ray and VUV-light), the hemispherical electron energy analysers (EA 125 and AR 65), four-axes cryo-manipulator and low energy electron diffraction (LEED) unit to check sample surface orientation. The working principle of a few of the important components are discussed below.

### 2.4.1 Gas Discharge Lamp

The VUV source can be operated with various discharge gases like helium, neon, argon, krypton, xenon or hydrogen. The operation of the lamp is based on the principle of a cold cathode capillary discharge [30]. The lamp is water cooled in order to allow for high discharge current and to reduce electrode degradation resulting in prolonged service intervals. There is a windowless direct sight connection between the discharge area and target. The ignition potential is an order of magnitude higher than the operating potential needed to maintain a continuous discharge. The nature and intensity of the radiation are strongly dependent on gas pressure and discharge current. There are two modes of functioning, namely, lines of neutral atoms (HeI, NeI etc.) and lines of singly charged ions (HeII, NeII etc.). Here, in our ARUPS Laboratory we use a discharge lamp using He or Ne for high resolution studies of the valence band and the near Fermi level ( $E_F$ ) features.

In the VUV discharge lamp, a high dc voltage ( $\sim 500$  V) is applied across a cell containing an inert gas e.g., helium or neon. This will cause an electrical discharge in the gas in which atoms go into an excited state and subsequently the excited states decay very fast by

emitting photons with an energy equal to the energy difference between the excited states and the ground states. In the case of helium, two groups of radiation are present: the first one originates from the decay of excited neutral helium atoms i.e.,  $\text{He } 1s 2p \rightarrow \text{He } 1s^2$  ( $\alpha$ ),  $\text{He } 1s 3p \rightarrow \text{He } 1s^2$  ( $\beta$ ),  $\text{He } 1s 4p \rightarrow \text{He } 1s^2$  ( $\gamma$ ),  $\text{He } 1s 5p \rightarrow \text{He } 1s^2$  ( $\delta$ ), and the second one from the decay of singly ionized helium atoms, i.e.,  $\text{He}^+ 2p \rightarrow \text{He}^+ 1s$  ( $\alpha$ ),  $\text{He}^+ 3p \rightarrow \text{He}^+ 1s$  ( $\beta$ ),  $\text{He}^+ 4p \rightarrow \text{He}^+ 1s$  ( $\gamma$ ),  $\text{He}^+ 5p \rightarrow \text{He}^+ 1s$  ( $\delta$ ). They are labeled as He I ( $\alpha$ ,  $\beta$ ,  $\gamma$  and  $\delta$ ) and He II ( $\alpha$ ,  $\beta$ ,  $\gamma$  and  $\delta$ ) respectively. The  $\alpha$  lines are the strongest ones and occur at 21.22 eV and 40.81 eV for He I and He II respectively. The relative intensities of He I  $\alpha$  and He II  $\alpha$  depend on the conditions of the discharge, particularly the lamp pressure. The amount of He II radiation is normally very small but can be increased by decreasing the lamp pressure. The typical discharge condition for He I are the following:

Inert gas used	Discharge voltage (Volt)	Discharge current (mA)	Lamp pressure (mbar)
Helium $1s 2p \rightarrow 1s^2$ (He I $\alpha$ )	$\sim 500$	80	$\sim 8.7 \times 10^{-01}$

In order to produce a narrow beam the discharge is confined in a narrow quartz capillary. A capillary is mounted at the output stage of the lamp to direct the light onto the sample target. The total photon intensity that is transferred through the capillary to the sample target is proportional to the cross sectional area of the inner bore of the capillary. Due to lack of proper window material in the UV range, two stages of differential pumping are employed to maintain the chamber in UHV while providing a stable pressure in the lamp. At the first stage, the discharge region is pumped down to a pressure of  $\sim 10^{-2}$  mbar using a rotary pump, whereas for the second stage, a turbomolecular pump is employed to further reduce the He gas pressure before the main vacuum chamber.

## 2.4.2 X-ray source

We used DAR 400 X-ray source from OMICRON. It is a twin anode (Mg  $K\alpha$  (1253.6 eV) Al  $K\alpha$  (1486.6 eV)) X-ray source. Electrons are extracted from a hot filament and focused to bombard the selected surface of an anode at high positive potential. The excited core

level electrons emit characteristic X-rays when they de-excite to a lower energy level. The anode is water cooled to prevent the aluminium or magnesium surfaces from evaporating. X-rays generated at the surface of the anode pass through a thin aluminium window to the sample under study. The aluminium window acts as a partial vacuum barrier between the source and the sample region.

### 2.4.3 Synchrotron Radiation

Frequencies generated in Synchrotron radiation (SR) covers almost the entire range of electromagnetic spectrum. Hence, Synchrotron radiation sources are widely used in PES experiments. It is well known that accelerated or decelerated charged particles emit electromagnetic radiation. Based on this principle, Synchrotron radiation is produced from the relativistic electrons, which are guided in a polygon-shaped vacuum tube (called storage ring) by applying a centripetal acceleration. This centripetal acceleration is caused by strong magnets arranged on the corners of the polygon. The electrons are emitted from a cathode and accelerated linearly outside the ring up to several MeV. Then the electrons are inserted into the ring and the bending magnets deflect them. At this stage the electrons emit synchrotron radiation tangential to their trajectory. The energy loss of the electrons due to emission of radiation is compensated by allowing the electrons to pass through radio-frequency cavity. In the present days, insertion devices such as wigglers and undulators which employ periodic magnetic fields to produce radiation with no net deflection of the beam are used to obtain much brighter radiation. Finally a beamline takes the radiation from the ring to the experimental stations. Compared to discrete resonance lines obtained from laboratory source synchrotron source provides several advantages, e.g., its high intensity photon beam allows rapid experiments and highly collimated (due to spatial coherence) photon beam generated by a small divergence allows one to study very small size sample.

The resonance photoemission and x-ray absorption spectroscopy presented in this work were carried out using BACH beamline at Elettra synchrotron light laboratory, Trieste, Italy. BACH beamline employs undulators to enhance the intensity of emitted radiation. It works in the UV-soft X-ray photon energy range (35-1600 eV) with selectable light polarizations. It is equipped with four spherical gratings (SG1, SG2, SG3 and SG4) to select photons in different energy ranges.

## 2.5 Energy Analyser

In this work the UPS and XPS data were collected by a hemispherical analyser (EA125) with a mean radius of 125 mm and the ARPES spectra were recorded by a rotatable hemispherical analyser (AR65) with a mean radius of 65 mm. The analyser EA125 is not movable whereas the AR65 analyser is mounted on a double axes goniometer with two independent degrees of freedom. The possible directions of rotation of the analyser is shown in figure 2.8.

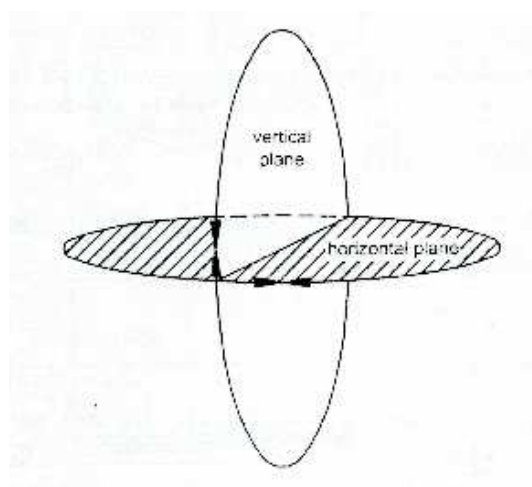


**Figure 2.8:** Rotation planes of AR65 analyser.

### 2.5.1 Hemispherical Analyser

A hemispherical deflection analyser consists of two concentric hemispheres, schematically shown in Fig. 2.9. The entrance and exit slits are centered on the mean radius of the inner and outer spheres. A potential difference is applied between the two hemispheres, with the outer one being negative with respect to the inner one. The voltages on the inner and outer hemispheres ( $V_1$  and  $V_2$ ), which allow only those electrons having a kinetic energy  $E_{pass}$  (usually called pass energy) to enter into the analyser, are given by the following equations:

$$eV_1 = E_{pass}[2R_0/R_1 - 1] \quad (2.34)$$

$$eV_2 = E_{pass}[2R_0/R_2 - 1] \quad (2.35)$$

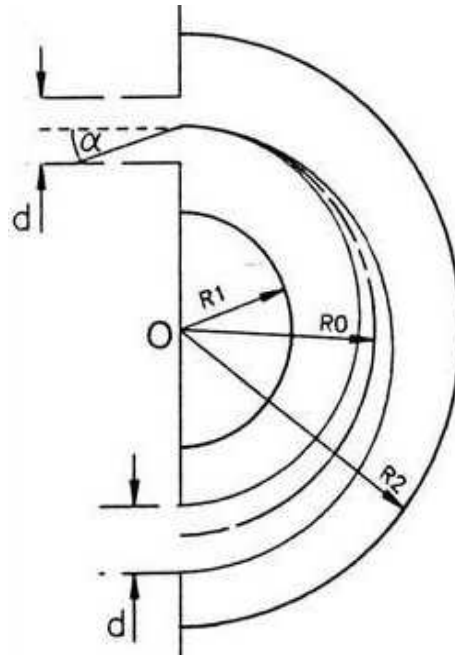


**Figure 2.9:** A schematic diagram of hemispherical analyser.

where  $R_1$  and  $R_2$  are the radii of the inner and outer spheres, respectively with respect to a common centre, and  $R_0$  denotes the mean radius of the two spheres with  $R_0 = (R_1 + R_2)/2$ . The theoretical energy resolution of the analyser  $\Delta E$  is approximately expressed as [28]

$$\Delta E = E_{pass} [d/2R_0 + \alpha^2/4] \quad (2.36)$$

where  $d$  is the slit width (entrance slit) and  $\alpha$  (in radian unit) is the acceptance angle of the analyser. In practice the energy resolution can be varied by changing the pass energy and slit width.

### 2.5.2 Electron Lens System

The electron lens is a multi-element electrostatic lens fitted at the entrance to the analyser. The purpose of the lens is to collect electrons from a larger solid angle and to vary the energy of the beam to the pass energy of the analyser. The resolution obtainable with the hemispherical analyser can be significantly increased by reducing the pass energy of the analysed electrons. An electron lens typically consists of two or more cylinders, which are held at different potentials. The electric field that exists between the elements acts

upon the electrons that pass through it. In cylindrical lenses, the adjacent cylinders are kept at different potentials and focusing takes place. The simplest practical lens consists of two aligned cylinders at different potentials. However, by employing a third element it is possible to accelerate or retard electrons by varying amounts.

### 2.5.3 Single Channel Detector

The photoelectrons in a PES experiment is counted using a channeltron. A channeltron is an electron multiplier made up of a small curved glass tube, the inside wall being coated with a high resistance material. A high voltage is applied along the tube. When a high energy particle enters the low potential end of the tube it collides with the wall, ejecting secondary electrons. These secondary electrons are then accelerated down the tube, making further collisions with the curved wall; each collision generates more and more electrons in an avalanche, resulting in a large electron cloud at the other end of the tube. Thus, from an input of one electron the channeltron respond by producing an output pulse with a typical gain of  $10^8$  [28]. The output can either be measured by a ratemeter or a computer. The data-taking capacity can be enhanced by using a multichannel detector, which consists essentially of a microchannel plate or several channeltrons to perform parallel detection. We have used a single channel detector to detect the photoelectrons passing through the hemispherical deflector.

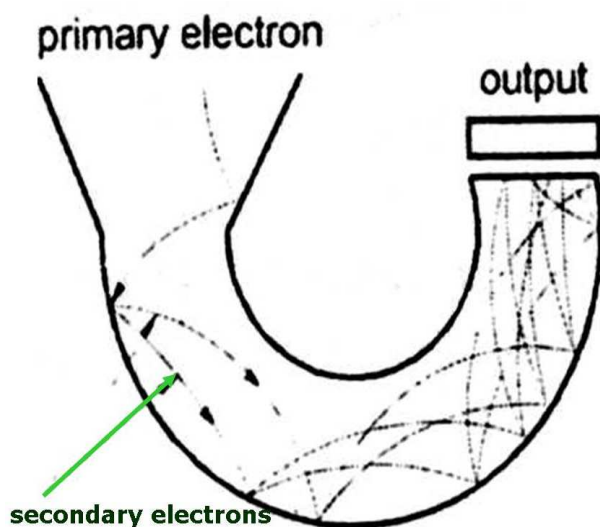


**Figure 2.10:** A schematic diagram of electron amplification in a channeltron.

### 2.5.4 Pulse Counting Operation

In an electron spectrometer, electrons which arrive at the input of the channeltron detector generate secondary electrons which are then accelerated down the channeltron by a positive voltage bias (+2 kV to +3 kV at the output). These electrons strike the channeltron wall producing additional electrons progressively down the channeltron to the output where between  $10^7$  to  $10^8$  electrons arrive (fig. 2.10).

### 2.5.5 Channeltron Operating Plateau

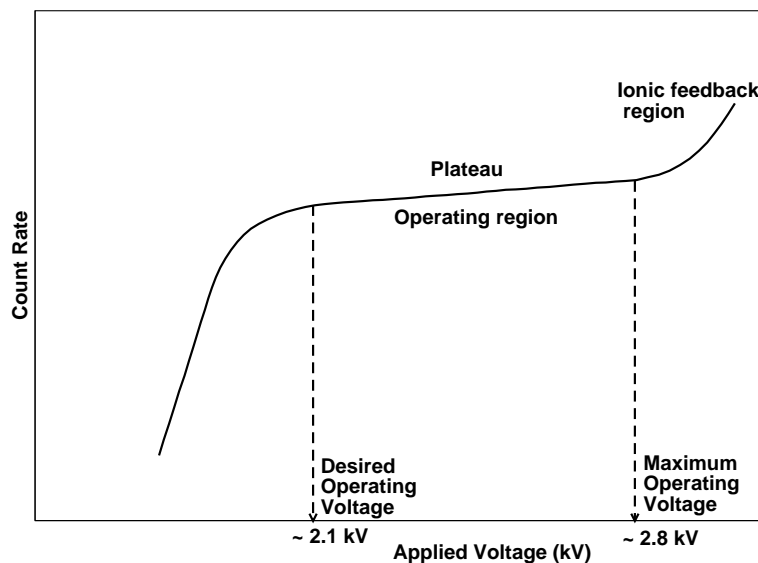


**Figure 2.11:** A plateau curve of a channeltron.

As the voltage applied to a channeltron is increased, the gain increases and the output pulse height increases. As more and more output pulses exceed the threshold set in the preamplifier, the observed count rate increases. When the gain is large enough for the smallest pulses in the distribution to exceed the threshold, a plateau is reached and no further increase in count rate is observed with higher voltages as shown in figure 2.11. At very high voltages, the observed count rate again increases due to the feedback of positive ions generated within the channeltron. This should always be avoided as the observed pulses do not result from an input and operating channeltrons in this condition considerably reduces their lifetime.

The onset of the plateau is reached at approximately 2 kV for new channeltrons and this slowly increases as the channeltron ages. The desired operating voltage is approximately 100 V above the onset of the plateau. The electron pulse is then routed to a preamplifier which filters out the system noise using a high speed threshold comparator circuit. The electrical signal is converted to an optical signal which is transmitted to the receiver unit via an optical fiber link. The receiver unit converts the optical signal to a digital electronic pulse which is then counted by the computer. The optical link isolates the pulse counting system, usually a computer, from the spectrometer and low noise data levels.

### 2.5.6 Low Energy Electron Diffraction (LEED) unit

In addition to the gas discharge lamp and two electron spectrometers EA 125 and AR 65, the main chamber is also equipped with a Low Energy Electron Diffraction (LEED) apparatus which is used to determine the orientation of crystal surface. The LEED experiment uses a beam of electrons of a well-defined low energy (typically within 20 -200 eV) incident normally on the sample. Since the de Broglie wavelength associated with low energy electron is comparable to the lattice constant of a crystal, its diffraction can give information regarding the geometrical structure of the crystal and as the energy is quite low it is very much surface sensitive. The sample under study must be a single crystal with a well-ordered surface structure in order to generate a back-scattered electron diffraction pattern. For a polycrystal it will give a diffused circular pattern. A typical experimental set-up is shown in figure 2.12. Only the elastically-scattered electrons contribute to the diffraction pattern. The lower energy (secondary) electrons are removed by energy-filtering grids placed in front of the fluorescent screen that is employed to display the pattern.

### 2.5.7 Sample Surface Preparation

It has already been discussed that the PES experiment is a highly surface sensitive technique [29]. In order to get the spectra from clean surfaces, vacuum better than  $10^{-10}$  mbar is mandatory for VUV-PES experiments. This makes the preparation and preservation of a clean sample surface essential to PES measurement. Among the surface preparation techniques that have been used, in situ scraping and in situ cleaving are the safest. Here we have used in situ cleaving for graphite samples, i.e., single crystal graphite and HOPG. The samples were cleaved by using post technique inside the preparation chamber. The transition metal oxide samples, i.e.,  $\text{Bi}_{1-x}\text{Pb}_x\text{FeO}_3$  and  $\text{Sm}_{0.1}\text{Ca}_{0.9-x}\text{Sr}_x\text{MnO}_3$ , were scraped insitu

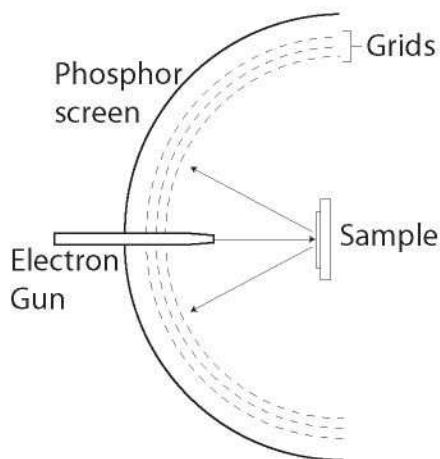


**Figure 2.12:** A typical set-up of LEED experimental.

using a diamond file. The sample was mounted on a stainless steel sample holder using commercial UHV compatible glue and using silver paste it was made conductive with the sample plate. The sample was first loaded under atmosphere into the load lock, which can be pumped down to  $1 \times 10^{-7}$  mbar within one hour, then transferred into the preparation chamber with base vacuum  $\sim 7 \times 10^{-10}$  mbar. In the preparation chamber, we cleaved the graphite samples and then took the LEED pattern inside the analysis chamber. We repeatedly scraped the oxide samples by a diamond file until the feature at  $\sim 9.5$  eV binding energy disappears. This feature has earlier been shown to originate from surface contamination, particularly adsorbed oxygen [31]. After scraping we transfer the sample into the analysis chamber immediately and take the spectra quickly. To check the reproducibility of the results, all measurements reported here have been repeated at different times.

- [1] H. Hertz; Ann. Phys. **17**, 983 (1887).
- [2] J. J. Thomson; Phil. Mag. **48**, 547 (1899).
- [3] P. Lenard; Ann. Physik **2**, 359 (1900).
- [4] A. Einstein; Ann. Phys. **31**, 132 (1905).
- [5] C. N. Berglund and W. E Spicer, Phys. Rev. **136**, A1044 (1964)
- [6] G. W. Gobeli, E. O. Kane, and F. G. Allen, Phys. Rev. Lett. **12**, 94 (1964)
- [7] E. O. Kane, Phys. Rev. Lett. **12**, 97 (1964)
- [8] N. V. Smith and L.F. Mattheiss. Phys. Rev. B, **9**, 1341 (1974).
- [9] N. V. Smith. Phys. Rev. B, **9**, 1365 (1974).
- [10] N. V. Smith, M. M. Traum, and F. J. DiSalvo. Solid State Comm. **15**. 211 (1974).
- [11] M. M. Traum, N. V. Smith and F.J. DiSalvo. Phys. Rev. Lett. **32**, 1241 (1974).
- [12] T. Kiss, F. Kanetaka, T. Yokoya, T. Shimojima, K. Kanai, S. Shin, Y. Onuki, T. Togashi, C. Zhang, C. T. Chen and S. Watanabe. Phys. Rev. Lett. **94**, 057001 (2005).
- [13] C. N. Berglund and W. E Spicer, Phys. Rev. **136**, A1030 (1964)
- [14] H. Y. Fan; Phys. Rev. **68**, 43 (1945).
- [15] H. Mayer and H. Thomas; Z. Phys. **147**, 419 (1957).
- [16] H. Puff; Phys. Stat. Sol. **1**, 636 (1961).
- [17] Volker Dose, Progress In Surface Science, **13**, 225-284 (1983)
- [18] Neville V Smith, Rep. Prog. Phys. **51**, 1227-1294 (1988)
- [19] P. D. Johnson, S. L. Hulbert, Rev. Sci. Instrum. **61**, 2277 (1990)
- [20] S. Banik, A. K. Shukla, and S. R. Barman, Rev. Sci. Instrum **76**, 066102 (2005)
- [21] N. G. Stoffel and P. D. Johnson, Nucl. Inst. & Meth. A **234**, 230 (1985)

- [22] G. D. Mahan; Phys. Rev. B **2**, 4334 (1970)
- [23] C. Caroli, D. Lederer-Rosenblatt, B. Roulett, and D. Saint James; Phys. Rev. B **8**, 4552 (1973)
- [24] P. J. Feibelman and D. E. Eastman; Phys. Rev. B **10**, 4932 (1974)
- [25] G. Jezequel and I. Pollini; Phys. Rev. B **41**, 1327 (1990)
- [26] L. Hedin and S. Lundqvist, in Solid State Physics, edited by F. Seitz, D. Turnbull, and H. Ehrenreich, (Academic Press, New York, 1969), Vol. **23**
- [27] S. G. Louie, in Angle-resolved Photoemission, edited by S. D. Kevan, (Elsevier, Amsterdam, 1992), Vol. **74**
- [28] Omicron Instruction Manual for HA Analyser.
- [29] D. A. Shirley; in Photoemission in Solids I, edited by M. Cardona and L. Ley, (Springer Verlag, Berlin, 1978) Vol **26**, p. 193
- [30] G Schönhense and U Heinzmann, J. Phys. E: Sci. Instrum. **16**, 74 (1983)
- [31] D. D. Sarma, N. Shanthi, S. R. Krishnakumar, T. Saitoh, T. Mizokawa, A. Sekiyama, K. Kobayashi, A. Fujimori, E. Weschke, R. Meier, G. Kaindl, Y. Takeda and M. Takano, Phys. Rev. B **53**, 6873 (1996)

# 3

## Tight Binding Calculations of Graphene, Bilayer Graphene and Graphite

### 3.1 Introduction

In this chapter we describe our tight binding band structure calculations of three graphitic systems, namely, graphene, bilayer graphene and graphite as in the next chapter we will be presenting valence and conduction band mapping of graphite using ARPES and KRIPES. Though we have done experiment only on graphite, the band calculation has been initiated with graphene, the two dimensional approximation of graphite, then developed for bilayer graphene, a system more close to graphite in reality, and finally extended up to three dimensional graphite within similar formalism because it gives some sort of completeness as well as helps to build up an insight of how the electronic dispersion evolves with the dimensionality of a system. To calculate the bands, tight binding scheme has been chosen because the  $p_z$  electrons, which are almost localized in space, play the fundamental role in determining the electronic behaviours in these materials. In the subsequent paragraphs we will introduce the above mentioned systems individually and discuss how far these materials have been exploited using tight binding method.

Graphene is a single sheet of atomic thickness with carbon atoms arranged hexagonally. Though it is an ideal two dimensional material of theoretical interest and one of the earliest material on which tight binding band structure calculation was done [2, 3], it has triggered recently a lot of interest including the reinvestigation of many earlier results since its experimental discovery in 2004 [4], particularly, a large no of tight binding band calculations have been performed with nearest neighbour hopping but without overlap integral correc-

tion [1–3, 5–9]. Some calculations have considered the overlap integral correction [2, 8], out of these only few calculations are there which take care of second and third nearest neighbours along with overlap integral corrections [1, 9]. It is noticed that the first nearest neighbour hopping integral ( $\gamma_0$ ) lies around 2.5eV-3.0eV when tight binding band is fitted with first principle calculation or experimental data [1, 6, 8] near the  $K$  point of the Brillouin zone of graphene, but interestingly, when one tries to have a good agreement of the tight binding band over the whole Brillouin zone by including up to third nearest neighbour hoppings and overlap integrals, the tight binding parameters are considered as merely fitting parameters, not as physical entities [1] i.e., the values of parameters do not decrease consistently as one moves towards second and third nearest neighbours. In present work we have fitted our tight binding band with first principle data with the objective to get a set of parameters which is free from the above discrepancy and found out a set which gives good matching with the first principle data over the whole Brillouin zone. Here we have also calculated the density of states with second and third nearest neighbours.

Bilayer graphene is a system of two stacked hexagonal graphene sheets. Among all the carbon based materials of recent interest, bilayer graphene is of much importance because this is the only two dimensional material in which the band gap between valence and conduction bands can be controlled by applying an external electric field perpendicular to the layers [9–14] or by chemical doping of one of the layers [15]. This makes it a potential candidate for future application in nanoelectronics. There has been a significant amount of effort to study the band structure of bilayer graphene [5, 9, 15–17]. Regarding this the major concern was to see how the linear dispersion near the  $K$  point in single layer graphene gets modified in presence of interlayer coupling in bilayer graphene. It is now well established that even the slightest presence of the interlayer coupling kills the linearity of the dispersion of monolayer graphene and converts it to a parabolic one for the Bernal stacked bilayer graphene. Moreover, most of the studies have talked about the symmetric nature of the valence and conduction bands of bilayer graphene. Only very recently there have been reports [17–19] regarding asymmetry between the valence and conduction bands in this system. In the present work on bilayer graphene we have investigated some parameters which also contribute appreciably towards asymmetry in the bands of this system. While the existing literature mostly discusses the effect of interlayer coupling in bands of bilayer graphene and in graphite [20], we report here about the asymmetry in band structure of bilayer graphene which arises due to the inclusion of in-plane and interplane nearest neighbour overlap integrals ( $s_0$  and  $s'_1$ ) in the tight binding band structure calculation because

we have noticed that the presence of nearest neighbour overlap integral ( $s_0$ ) gives quite a bit of asymmetry in the band structure of monolayer graphene [2, 8]. We have also studied the effects of in-plane next nearest neighbour and next to next nearest neighbour hopping energies ( $\gamma_1$  and  $\gamma_2$ ) along with the corresponding overlap integrals ( $s_1$  and  $s_2$ ) on the band structure of this system in line with the work on single layer graphene [1]. The in-plane parameters used here were determined by comparing the tight binding bands of single layer graphene with the first principle results, by emphasizing the fact that the magnitudes of the parameters should decrease with increasing distance (e.g.,  $\gamma_0 > \gamma_1 > \gamma_2$  and  $s_0 > s_1 > s_2$ ) as has been mentioned in the previous paragraph.

Graphite is a weakly three dimensional system of infinite stack of graphene sheets with interlayer distance much larger than in-plane interatomic distance. In nature graphite exists with various stacking sequences, namely AA, AB (Bernal stacking) and ABC among which AB stacked graphite is most abundant. In this work, utilizing the same tight binding in-plane coupling parameters for single layer graphene and the interlayer coupling parameters for bilayer graphene, we have calculated the band structure of AB stacked graphite in the way similar to that of bilayer graphene and discussed the effect of these parameters on the energy dispersions along different high symmetry directions, particularly near the  $K$  and  $H$  points.

## 3.2 Geometrical structure

Since the geometrical structure of a material plays a crucial role in determining its electronic dispersion, it is important to look at the details of the crystal structure. Here we describe the structures of graphene, bilayer graphene and graphite. An ideal graphene sheet consists of a regular hexagonal arrangement of carbon atoms in two dimension as shown in fig. 3.1. It consists of two inequivalent (with respect to orientations of bonds) triangular sublattices called A-sublattice and B-sublattice. The unit cell contains one A and one B type of carbon atoms contributed by respective sublattices. Each carbon atom has three nearest neighbours coming from the other sublattice, six next nearest neighbours from the same sublattice and three next to next nearest neighbours from the other sublattice.  $a_0$  (1.42 Å) is the nearest neighbour lattice distance. In the figure,  $\vec{a}_1$  and  $\vec{a}_2$  are the unit vectors with magnitude  $a = \sqrt{3}a_0$  i.e., 2.46 Å. With respect to  $A_0$  atom the coordinates of the first neighbours ( $B_{1i}, i = 1, 2, 3$ ); second neighbours ( $A_{2i}, i = 1, \dots, 6$ ) and third neighbours ( $B_{3i}, i = 1, 2, 3$ ) are  $(a/\sqrt{3}, 0)$ ,  $(-a/2\sqrt{3}, -a/2)$ ,  $(-a/2\sqrt{3}, a/2)$ ;

$(0, a)$ ,  $(\sqrt{3}a/2, a/2)$ ,  $(\sqrt{3}a/2, -a/2)$ ,  
 $(0, -a)$ ,  $(-\sqrt{3}a/2, -a/2)$ ,  $(-\sqrt{3}a/2, a/2)$  and  $(a/\sqrt{3}, a)$ ,  $(a/\sqrt{3}, -a)$ ,  $(-2a/\sqrt{3}, 0)$  respectively.

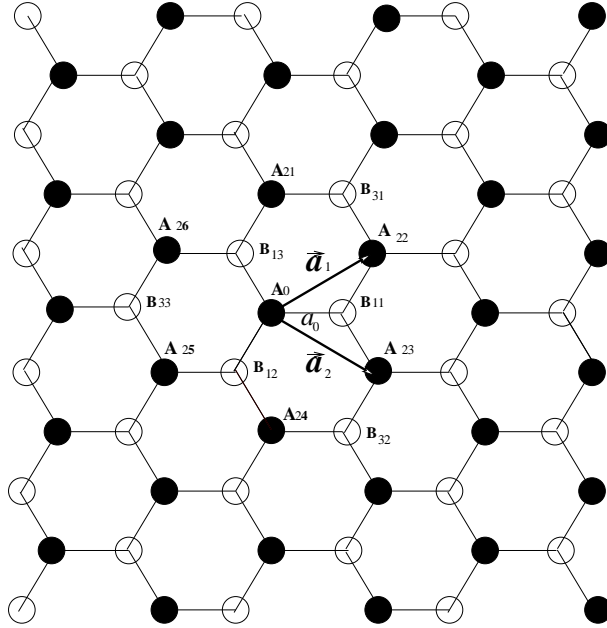


**Figure 3.1:** Structure of graphene. The structure with black circles forms the A-sublattice and that with empty circles gives B-sublattice.  $\vec{a}_1$  and  $\vec{a}_2$  are the unit vectors.

Bilayer graphene is a coupled system of two monolayers of graphene with usually an AB-stacking fashion of the layers, i.e., the atoms in one layer are not just on top of the corresponding atoms in the other layer, rather the arrangement is such that if one layer is projected on the other, the A-type (say) atoms coincide with the A-type atoms but the B-type atoms come at the center of the hexagons of the other layer [16]. So A and B type atoms can not be treated as chemically equivalent carbon atoms as they belong to two different chemical environments. This site energy difference between two atoms in two different sublattices in the same layer is defined here as the asymmetry energy  $\Delta$ . Since its value is very small ( $\sim 18$  meV) [18], these two atoms are usually treated as chemically equivalent. The structure of AB stacked bilayer graphene and its brillouin zone are shown in figure (3.2). The distance between two atoms in a layer is the same as graphene and the interlayer separation is  $3.35 \text{ \AA}$ . The brillouin zone of bilayer graphene is also same as that of single layer graphene because it does not have periodicity along z-direction. Bilayer graphene unit cell contains four atoms. The relevant hopping parameters, i.e.,

nearest neighbour in-plane coupling energy ( $\gamma_0$ ), nearest neighbour interplane coupling energy ( $\gamma'_1$ ), next nearest neighbour in-plane coupling energy ( $\gamma_1$ ) and next to next nearest neighbour in-plane coupling energy ( $\gamma_2$ ) have also been shown in the figure.

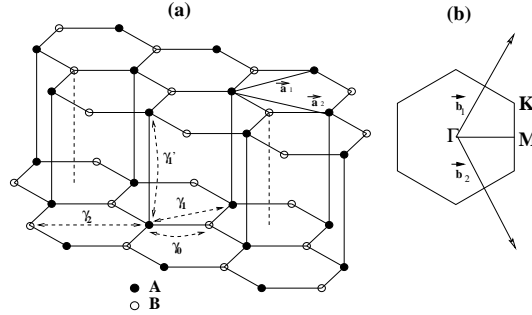


**Figure 3.2:** (a) Structure of bilayer graphene with unit vectors  $\vec{a}_1, \vec{a}_2$ ; the intralayer nearest neighbour coupling energy ( $\gamma_0$ ), interlayer nearest neighbour coupling energy ( $\gamma'_1$ ), intralayer next nearest neighbour coupling energy ( $\gamma_1$ ) and next to next nearest neighbour coupling energy ( $\gamma_2$ ). (b) Brillouin zone of single layer and bilayer graphene with unit vectors  $\vec{b}_1, \vec{b}_2$  and the high symmetry directions.

The structure of graphite is an infinite sequence of AB-stacked graphene layers where the interlayer atomic distance is much larger compared to the intralayer atomic distance similar to bilayer graphene. The only difference with a bilayer graphene is that it has periodicity along the third direction also leading to a three dimensional Brillouin zone. Also, in principle, the value of the asymmetric energy parameter  $\Delta$  should be different in this case.

### 3.3 Electronic structure of a hexagonal sheet of carbon atoms

Since hexagonal array of carbon atoms, i.e., graphene is the building block of bilayer graphene and graphite, it will be relevant to discuss first the basics of electronic configuration of the carbon atoms in graphene. Carbon atom has six electrons with the electronic configuration  $1s^2 2s^2 2p^2$ .  $2s$  and  $2p$  levels of carbon atom can mix up with each other and give rise to various hybridized orbitals depending on the proportionality of  $s$  and  $p$  orbitals. Graphene has  $sp^2$  hybridization:  $2s$  orbital overlaps with  $2p_x$  and  $2p_y$  orbitals and generates three new in-plane  $sp^2$  orbitals each having one electron. The  $2p_z$  orbital remains unaltered and becomes singly occupied. Due to overlap of  $sp^2$  orbitals of adjacent carbon atoms

strong  $\sigma$  (bonding) and  $\sigma^*$  (antibonding) bonds are formed. The bonding  $\sigma$  bonds, lying in a plane, make an angle of  $120^\circ$  with each other and is at the root of hexagonal planar structure of graphene.  $p_z$  orbitals being perpendicular to the plane overlap in a sidewise fashion and give  $\pi$  (bonding) and  $\pi^*$  (antibonding) bonds.  $sp^2$  orbitals with a lower binding energy compared to  $1s$  (core level) are designated as semi core levels and  $p_z$  orbitals having lowest binding energy are the valence levels. Overlapping of  $p_z$  energy levels gives the valence band (bonding  $\pi$  band) and conduction band (antibonding  $\pi^*$  band) in graphene. Thus, we see that while the structure of graphene is because of  $\sigma$  bonds, the  $\pi$  band is responsible for the electronic properties of graphene and hence, as far as electronic properties of graphene are concerned, emphasis is given only on  $\pi$  bands. Since the  $p_z$  orbitals overlap in a side-wise manner, the corresponding coupling is weaker compared to that of  $\sigma$  bonds (where  $sp^2$  orbitals overlap face to face). Therefore the  $p_z$  orbitals essentially retain their atomic character. Hence, to describe the electronic structure of graphene as well as of bilayer graphene and graphite, tight binding model could be a good choice.

### 3.3.1 Tight binding band of graphene

In this subsection tight binding bands of graphene have been reproduced including up to third nearest neighbour hopping of electrons and overlap integral corrections with focus on the point to find out tight binding parameters which are not just fitting parameters but they have physical significance. The results have been compared with existing literature [1]. The key equations are shown here for the different cases of nearest neighbours, next nearest neighbours and next to next nearest neighbours and the details of the calculations are given in the last section of this chapter. Since there are two atoms per unit cell coming from two sublattices, the total wave function can be written as

$$\Psi_k(r) = C_A \Psi_A^k + C_B \Psi_B^k, \quad \text{where} \quad (3.1)$$

$$\Psi_{A/B}^k(r) = \left(1/\sqrt{N}\right) \sum_{A/B} e^{i\vec{k}\cdot\vec{r}_{A/B}} \Phi_{A/B}(r - r_{A/B}) \quad (3.2)$$

are the tight binding Bloch wave functions from A and B sublattices. Here,  $N$  is the number of unit cells in the crystal,  $C_A$  and  $C_B$  are contributions coming from A and B sublattices respectively,  $\Phi'$ s are  $2p_z$  atomic orbitals,  $k$  is crystal momentum and  $r_A$  and  $r_B$  are the positions of A and B atoms respectively with respect to a chosen origin. If  $H$  is the Hamiltonian

and  $E(k)$  the eigenvalue then

$$H\Psi_k(r) = E(k)\Psi_k(r), \quad (3.3)$$

which leads to the secular equation

$$\begin{vmatrix} H_{AA} - E(k)S_{AA} & H_{AB} - E(k)S_{AB} \\ H_{AB}^* - E(k)S_{AB}^* & H_{BB} - E(k)S_{AA} \end{vmatrix} = 0 \quad (3.4)$$

where  $H_{xy} = \int \Psi_x^{*k}(r)H\Psi_y^k(r)d\vec{r} = H_{yx}^*$  and  $S_{xy} = \int \Psi_x^{*k}(r)\Psi_y^k(r)d\vec{r} = S_{yx}^*$ . The indices  $x$  and  $y$  represent both A and B. Since two sublattices are equivalent,  $H_{AA} = H_{BB}$  and  $S_{AA} = S_{BB}$ . The general dispersion relation follows as

$$E^\pm(k) = \left[ (2E_0 - E_1) \pm \sqrt{(E_1 - 2E_0)^2 - 4E_1E_2} \right] / 2E_3, \quad (3.5)$$

where  $S_{AA}H_{AA} = E_0$ ,  $H_{AB}S_{AB}^* + H_{AB}^*S_{AB} = E_1$ ,  $H_{AA}^2 - H_{AB}H_{AB}^* = E_2$  and  $S_{AA}^2 - S_{AB}S_{AB}^* = E_3$ . The explicit forms of the dispersions in presence of different levels of neighbours are discussed below.

1. In case of nearest neighbour approximation the contribution comes from nearest atoms of the other sublattice. Detailed calculations of all the matrix elements are given in the last section of this chapter. From equation (3.5) the dispersion relation for this case becomes

$$E^\pm(k) = \left[ (E_{2p} - s_0\gamma_0g(k)) \pm (\gamma_0 - s_0E_{2p})\sqrt{g(k)} \right] / [1 - s_0^2g(k)], \quad (3.6)$$

where  $E_{2p}$ ,  $\gamma_0$  and  $s_0$  are site energy, nearest neighbour hopping and overlap integrals respectively.

2. With second nearest neighbour approximation the matrix elements  $H_{AA}$  and  $S_{AA}$  get modified but  $H_{AB}$  and  $S_{AB}$  remain as they were. The corresponding energy momentum relation is

$$E^\pm(k) = \left[ E_{2p} + \gamma_1u(k) \mp \gamma_0\sqrt{g(k)} \right] / \left[ 1 + s_1u(k) \mp s_0\sqrt{g(k)} \right], \quad (3.7)$$

where  $\gamma_1$  and  $s_1$  are next nearest neighbour hopping and overlap integrals respectively.

3. With third nearest neighbour approximation the matrix elements  $H_{AB}$  and  $S_{AB}$  get changed but  $H_{AA}$  and  $S_{AA}$  remain unaltered. Calculation of all the matrix elements gives expressions for  $E_1$ ,  $E_2$ ,  $E_3$  as follows:

$$\begin{aligned} E_1 &= 2s_0\gamma_0g(k) + (s_0\gamma_2 + \gamma_0s_2)t(k) + 2s_2\gamma_2g(2k) \\ E_2 &= [E_{2p} + \gamma_1u(k)]^2 - [\gamma_0^2g(k) + \gamma_0\gamma_2t(k) + \gamma_2^2g(2k)] \\ E_3 &= [1 + s_1u(k)]^2 - [s_0^2g(k) + s_0s_2t(k) + s_2^2g(2k)], \end{aligned}$$

which when put in equation (3.5) gives the energy momentum relation in this case.  $\gamma_2$  and  $s_2$  being next to next nearest neighbour hopping and overlap integrals respectively.

The bands of graphene for above three cases are plotted along the high symmetry directions of its hexagonal brillouin zone sketched in figure (3.2). As shown in the figure, the symmetry points are  $\Gamma(0, 0)$ ,  $M(2\pi/\sqrt{3}a, 0)$  and  $K(2\pi/\sqrt{3}a, 2\pi/3a)$ . There are six corner points, out of which three are independent since the nearby corner points ( $K$  and  $K'$ ) are inequivalent. In fig. (3.3) we have compared the bands with nearest, next nearest and next to next nearest neighbour hopping and overlaps with a first principle calculation (produced from this model with the parameters  $E_{2p} = -0.36$  eV,  $\gamma_0 = -2.78$  eV,  $\gamma_1 = -0.12$  eV,  $\gamma_2 = -0.068$  eV,  $s_0 = 0.106$ ,  $s_1 = 0.001$ ,  $s_2 = 0.003$  because within the chosen energy scale it does not show any energy difference with first principle data [1]) for the set of parameters shown in table 3.1 where we have first determined values of nearest neighbour parameters ( $\gamma_0$  and  $s_0$ ) which best reproduces the first principle result, then we have taken care of second nearest neighbours ( $\gamma_1$  and  $s_1$ ) keeping first nearest neighbour parameters fixed and lastly considered the third nearest neighbour parameters ( $\gamma_2$  and  $s_2$ ) with fixed ( $\gamma_0$ ,  $s_0$ ) and ( $\gamma_1$ ,  $s_1$ ) with the expectation to have better matching over the whole brillouin zone of graphene. We observe that nearest neighbour coupling gives good overall agree-

ment for both valence and conduction bands but with the inclusion of second and third nearest neighbours under the above restrictions, the overall matching of the valence band with the first principle band improves whereas for the conduction band it is good only in the optical range. When only nearest neighbour hopping is considered, the total band width (difference between valence band and conduction band energies) at  $\Gamma$  point is  $6|\gamma_0|$ , that at  $M$  point is  $2|\gamma_0|$  but when nearest neighbour overlap integral is also included the valence

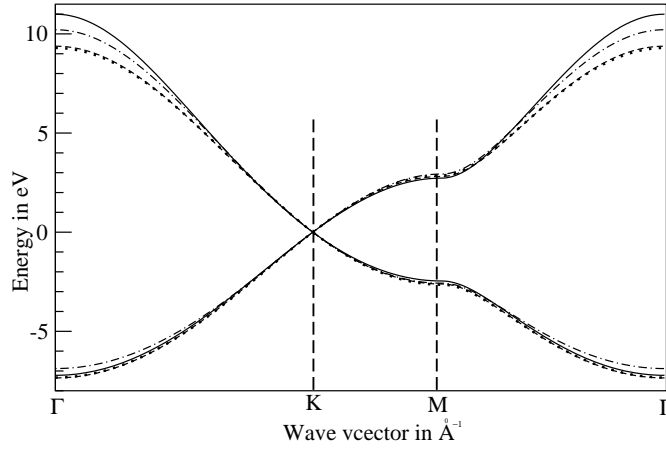


**Figure 3.3:** Electronic structure of graphene with first principle result (full curves), first nearest neighbour interactions (dashed-dotted curves), second nearest neighbour interactions (dotted curves) when first nearest neighbour parameters are fixed and third nearest neighbour interactions (dashed curves) when first and second nearest neighbour parameters are fixed. The parameters are listed in Table 3.1.

**Table 3.1:** Tight binding parameters

Neighbours	$E_{2p}$ (eV)	$\gamma_0$ (eV)	$\gamma_1$ (eV)	$\gamma_2$ (eV)	$s_0$	$s_1$	$s_2$
1st	0.0	-2.74			0.065		
2nd	-0.21	-2.74	-0.07		0.065	0.002	
3rd	-0.21	-2.74	-0.07	-0.015	0.065	0.002	0.001

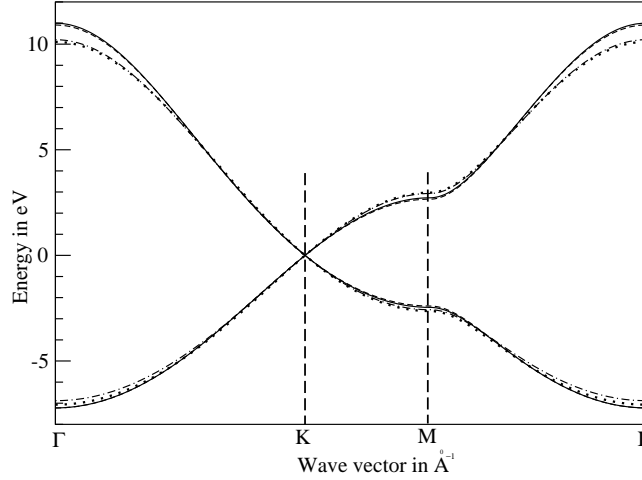


**Figure 3.4:** Electronic structure of graphene with first principle result (full curves), first nearest neighbour interactions (dashed-dotted curves), second nearest neighbour interactions (dotted curves) and third nearest neighbour interactions (dashed curves). The parameters are listed in Table 3.2. Here for each curve the parameters are chosen freely.

and conduction band energies at  $\Gamma$  point occur at  $3\gamma_0/(1+3s_0)$  and  $-3\gamma_0/(1-3s_0)$  respectively and those at  $M$  point appear at  $\gamma_0/(1+s_0)$  and  $-\gamma_0/(1-s_0)$  respectively. The  $K$  point energy is zero for both the cases. Including next nearest neighbours the energy at  $K$  point is  $(E_{2p} - 3\gamma_1)/(1 - 3s_1)$ . So the values of  $E_{2p}$  and  $\gamma_1$  are properly chosen to have  $K$  point energy at zero. In this case the valence and conduction band energies at  $\Gamma$  point are at  $(E_{2p} + 6s_1 + 3\gamma_0)/(1 + 6s_1 + 3s_0)$  and  $(E_{2p} + 6s_1 - 3\gamma_0)/(1 + 6s_1 - 3s_0)$  and those at  $M$  point are at  $(E_{2p} + 2s_1 + \gamma_0)/(1 + 2s_1 + s_0)$  and  $(E_{2p} + 2s_1 - \gamma_0)/(1 + 2s_1 - s_0)$  respectively. In fig. (3.4) we have plotted the above set of curves with a different set of parameters such that both nearest neighbour and next nearest neighbour parameters are free when the effect of second nearest neighbour is looked for and all three, i.e., (nearest, next nearest and next to next nearest neighbour) parameters are free when the third nearest neighbours are included. The parameters are shown in table 3.2. Fig. (3.4) shows that inclusion of second nearest neighbour gives better result over first nearest neighbour interaction compared to the plots in fig. (3.3). Consideration of third nearest neighbour couplings gives very good matching for both valence and conduction bands along all the high symmetry directions of the brillouin zone.

**Table 3.2:** Tight binding parameters

Neighbours	$E_{2p}$ (eV)	$\gamma_0$ (eV)	$\gamma_1$ (eV)	$\gamma_2$ (eV)	$s_0$	$s_1$	$s_2$
1st	0.0	-2.74			0.065		
2nd	-0.30	-2.77	-0.10		0.095	0.003	
3rd	-0.45	-2.78	-0.15	-0.095	0.117	0.004	0.002

### 3.3.2 Tight binding band of bilayer graphene

In the following we first present general aspects of the formalism of tight binding band structure of bilayer graphene and then give details of tight binding band dispersion under different situations like: (i) the simplest case with nearest neighbour in-plane and inter-plane hopping of  $\pi$  electrons; (ii) modifications in the bands due to the inclusion of overlap integrals coming from the same neighbours and due to site energy difference ( $\Delta$ ) between A and B atoms in two different sublattices in the same layer; (iii) effect of in-plane second nearest neighbour hopping and corresponding overlap integral; (iv) effect of in-plane third nearest neighbour hopping and overlap integral on the band near the brillouin zone corner ( $K$ ) point and over the whole brillouin zone, and also the density of states of bilayer graphene corresponding to the above mentioned dispersions. Since bilayer graphene unit cell contains four atoms coming from two different sublattices of two layers, the Bloch wave functions for A and B type atoms for each layer [5] are

$$\Psi_k^{A_i}(r) = 1/\sqrt{N} \sum_{A_i} \Phi_A(r - r_{A_i}) e^{ik \cdot r_{A_i}} \quad \text{and} \quad \Psi_k^{B_i}(r) = 1/\sqrt{N} \sum_{B_i} \Phi_B(r - r_{B_i}) e^{ik \cdot r_{B_i}},$$

where  $i$  refers to layer index,  $\Phi^s$  are  $p_z$  atomic orbitals,  $N$  is the number of unit cells in the crystal,  $C_{A_i}$  and  $C_{B_i}$  are contributions to the total wavefunction coming from  $i^{th}$  atom of A and B sublattices respectively. The total wave function is

$$\Psi_k(r) = \sum_{i=1,2} C_{A_i} \Psi_k^{A_i}(r) + \sum_{i=1,2} C_{B_i} \Psi_k^{B_i}(r).$$

With this choice of wavefunction a secular equation including the overlap integrals can be set up as follows

$$\begin{vmatrix} H_{A_1A_1} - E(k)S_{A_1A_1} & H_{A_1B_1} - E(k)S_{A_1B_1} & H_{A_1A_2} - E(k)S_{A_1A_2} & H_{A_1B_2} - E(k)S_{A_1B_2} \\ H_{B_1A_1} - E(k)S_{B_1A_1} & H_{B_1B_1} - E(k)S_{B_1B_1} & H_{B_1A_2} - E(k)S_{B_1A_2} & H_{B_1B_2} - E(k)S_{B_1B_2} \\ H_{A_2A_1} - E(k)S_{A_2A_1} & H_{A_2B_1} - E(k)S_{A_2B_1} & H_{A_2A_2} - E(k)S_{A_2A_2} & H_{A_2B_2} - E(k)S_{A_2B_2} \\ H_{B_2A_1} - E(k)S_{B_2A_1} & H_{B_2B_1} - E(k)S_{B_2B_1} & H_{B_2A_2} - E(k)S_{B_2A_2} & H_{B_2B_2} - E(k)S_{B_2B_2} \end{vmatrix} = 0,$$

where  $H$  is the Hamiltonian of the system and  $H'_{x_i y_j}$ ,  $S'_{x_i y_j}$  are defined as

$$H_{x_i y_j} = \langle \Psi_k^{x_i} | H | \Psi_k^{y_j} \rangle \quad \text{and} \quad S_{x_i y_j} = \langle \Psi_k^{x_i} | \Psi_k^{y_j} \rangle \quad \text{respectively.}$$

Here  $x, y$  stand for both A and B;  $i, j$  can take either of the values 1 and 2. When this equation is solved for finite  $\gamma_0$  and  $\gamma'_1$  only, ignoring the asymmetric energy ( $\Delta$ ), in-plane overlap integral ( $s_0$ ) and the interplane overlap integral ( $s'_1$ ), the resulting energy eigenvalues are

$$\begin{aligned} E_{1/2}(k) &= \mp \frac{1}{2} \left[ \gamma'_1 \mp \left[ \gamma_1'^2 + 4\gamma_0^2 g(k) \right]^{1/2} \right] \\ \text{and} \quad E_{3/4}(k) &= \mp \frac{1}{2} \left[ \gamma'_1 \pm \left[ \gamma_1'^2 + 4\gamma_0^2 g(k) \right]^{1/2} \right], \end{aligned}$$

where

$$g(k) = \left[ 1 + 4 \cos^2(k_y a/2) + 4 \cos(\sqrt{3}k_x a/2) \cos(k_y a/2) \right],$$

$\gamma_0 = \langle \phi(r - r_{A_i}) | H | \phi(r - r_{B_i}) \rangle$ ;  $i$  being the layer index and  $\gamma'_1 = \langle \phi(r - r_{A_1}) | H | \phi(r - r_{A_2}) \rangle$ . In a similar way  $\gamma_1$  and  $\gamma_2$  can be defined. The expansion around the  $K$  ( $2\pi/\sqrt{3}a, 2\pi/3a$ ) point gives

$$\begin{aligned} E_{1/4}(k) &= \pm \frac{3}{4} \left( \gamma_0^2 / \gamma_1' \right) a^2 (\delta k)^2, \\ \text{and} \quad E_{2/3}(k) &= \pm \gamma_1' \pm \frac{3}{4} \left( \gamma_0^2 / \gamma_1' \right) a^2 (\delta k)^2 \end{aligned}$$

where  $\delta k$  is a small change in  $k$  around the  $K$  point. From the above results we see that there are four  $\pi$  bands in bilayer graphene. All the bands are parabolic near the brillouin zone corner. Two of the bands are degenerate with zero energy at the  $K$  point.  $-\gamma'_1$  and  $\gamma'_1$  are the energies of the other two bands at that point, i.e.,  $\pm \gamma'_1$  is the energy separation

between the highest conduction and the lowest valence bands at that point. Also the valence and conduction bands are symmetric over the entire brillouin zone. Since each atomic site has one  $p_z$  electron, the Fermi energy ( $E_F$ ) for undoped bilayer graphene is at zero energy. The bands are plotted in figure (3.5).

### 3.3.2.1 Modifications in the bands due to the inclusion of overlap integrals ( $s_0, s'_1$ ) coming from in-plane and interplane nearest neighbours and due to breaking of sublattice symmetry

The secular equation now becomes

$$\begin{vmatrix} E_{2p} + \Delta - E(k) & a - bE(k) & \gamma'_1 - s'_1 E(k) & 0 \\ c - dE(k) & E_{2p} - E(k) & 0 & 0 \\ \gamma'_1 - s'_1 E(k) & 0 & E_{2p} + \Delta - E(k) & c - dE(k) \\ 0 & 0 & a - bE(k) & E_{2p} - E(k) \end{vmatrix} = 0, \quad (3.8)$$

where  $a = \gamma_0 f(k)$ ,  $b = s_0 f(k)$ ,  $c = \gamma_0 f^*(k)$ ,  $d = s_0 f^*(k)$  and  $f(k) = e^{ik_x a / \sqrt{3}} + 2e^{-ik_x a / 2\sqrt{3}} \cos k_y a / 2$ ,  $s_0 = \langle \phi(r - r_{A_i}) | \phi(r - r_{B_i}) \rangle$  and  $s'_1 = \langle \phi(r - r_{A_1}) | \phi(r - r_{A_2}) \rangle$ . In a similar way  $s_1$  and  $s_2$  can also be defined. The eigen solutions to the above equation are

$$E_{1/2}(k) = \left[ -B_1 \pm [B_1^2 - 4A_1 C_1]^{1/2} \right] / 2A_1 \quad (3.9)$$

$$\text{and } E_{3/4}(k) = \left[ -B_2 \pm [B_2^2 - 4A_2 C_2]^{1/2} \right] / 2A_2, \quad (3.10)$$

where

$$A_{1/2} = 1 - bd \pm s'_1, \quad B_{1/2} = ad + bc \mp \gamma'_1 \mp s'_1 E_{2p} - 2E_{2p} - \Delta, \quad C_{1/2} = \pm \gamma'_1 E_{2p} - ac + E_{2p}(E_{2p} + \Delta).$$

Figure (3.5) also shows the bands with finite values of  $\Delta$ ,  $s_0$  and  $s'_1$  for comparison. We first discuss the effect of the asymmetry term ( $\Delta$ ) on the spectra at  $K$  point. The two bands which are degenerate at  $K$  point, are not affected by  $\Delta$  at that point but the other two bands appear at energies  $\Delta - \gamma'_1$  and  $\Delta + \gamma'_1$ , i.e., though the separation is still  $\pm \gamma'_1$ , they become asymmetric with respect to Fermi energy at that point. This term has negligible effect on the slope of these curves. The lower panel of (a) in fig. (3.5) shows that the lower valence band comes closer to  $E_F$  whereas the upper conduction band moves away from  $E_F$  when the sublattice asymmetry is taken care of. Next we illustrate the effect of overlap integrals

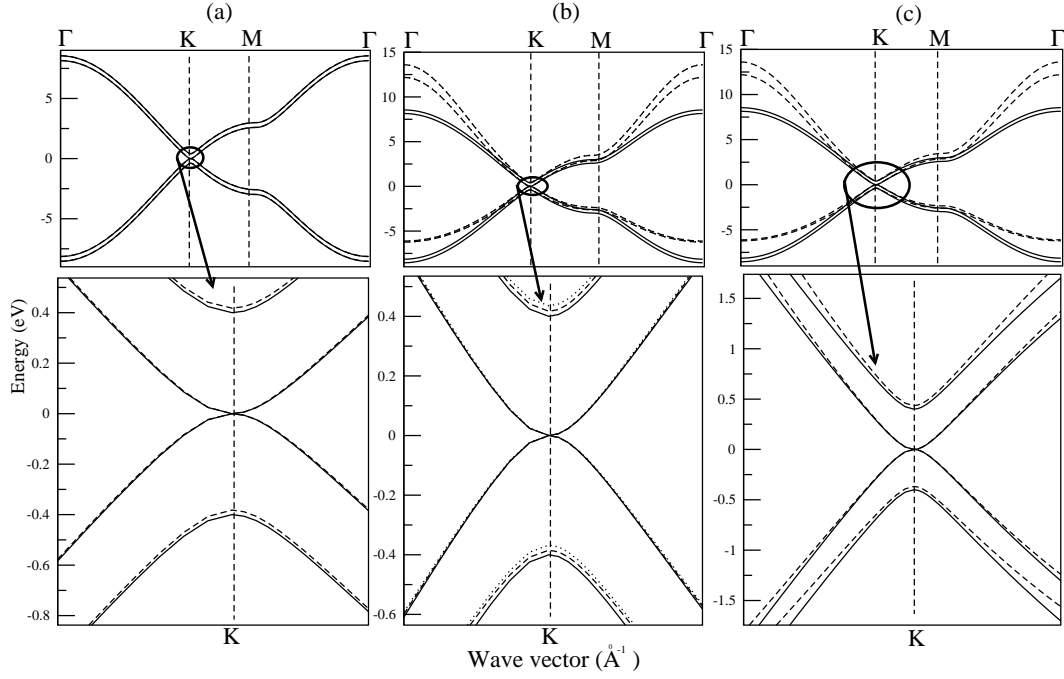


**Figure 3.5:** Electronic spectra of bilayer graphene. For all three cases, in the upper panel we have plotted the bands along all the high symmetry directions of the Brillouin zone and the lower panels show zoomed versions of the corresponding upper panels near the  $K$  point. In all the panels the full curves represent the symmetric bands, i.e., bands in presence of nearest neighbour in-plane ( $\gamma_0$ ) and interplane ( $\gamma'_1$ ) hopping energies. In (a) the dashed curves contain information due to the presence of sublattice asymmetry ( $\Delta$ ), clearly visible from the lower panel; in (b) the dashed curves have the effect of nearest neighbour in-plane ( $s_0$ ) and interplane ( $s'_1$ ) overlap integrals but zero  $\Delta$ , whereas the dotted curves are plotted with non-zero values of  $s_0$ ,  $s'_1$  and  $\Delta$ . Effects of these parameters at the  $K$  point are visible from the lower panel. In (c) the bands in presence of finite values of  $s_0$ ,  $s'_1$  and  $\Delta$  (dashed curves) are compared with the symmetric bands (full curves) over the whole Brillouin zone (upper panel) and nearer to the  $K$  point within optical energy range (lower panel). The relevant parameters are given in rows numbered 1 and 2 in Table 3.3.

$s_0$  and  $s'_1$  at  $K$  point. It is observed that the in-plane nearest neighbour overlap integral  $s_0$  has no effect at  $K$  point because it always appears in product with  $g(k)$  which vanishes at  $K$ . But the interlayer overlap integral  $s'_1$ , though not altering the degenerate bands, affects those bands lying further from  $E_F$  quite significantly. The upper lying band shifts further to  $-\gamma'_1/(1 - s'_1)$  and the lower band comes closer to  $\gamma'_1/(1 + s'_1)$  (dashed curves in lower panel of (b) in fig. (3.5)). The energy separation between them becomes  $2\gamma'_1/(1 - s'^2_1)$ . When  $\Delta$  and overlap integrals are considered together, the upper band shifts even further to  $(\Delta - \gamma'_1)/(1 - s'_1)$  and the lower band comes more close to  $(\Delta + \gamma'_1)/(1 + s'_1)$  (dotted curves in lower panel of (b) in fig. (3.5)). Under this condition the above energy separation becomes  $2(\gamma'_1 - s'_1\Delta)/(1 - s'^2_1)$ . Moreover,  $s_0$  and  $s'_1$  play important role in changing the slope of the curves. They push off the conduction bands and pull in the valence bands with respect to Fermi energy almost over the entire energy range, particularly near the  $\Gamma$  point where the effect is most prominent (dashed curves in upper panel of (c) in fig. (3.5)). With a closer look over the smaller energy range, i.e., the optical range, we see (in lower panel of (c)) that the separation between conduction bands increases while that between the valence bands decreases.

### 3.3.2.2 Effect of in-plane second nearest neighbour hopping ( $\gamma_1$ ) and corresponding overlap integral ( $s_1$ ) on the spectra of bilayer graphene

Since the in-plane next nearest neighbour atoms belong to same sublattice in a plane, we have in this case

$$\begin{aligned}
 A_{1/2} &= (1 + s_1 u(k))^2 - bd \pm s'_1 (1 + s_1 u(k)), \\
 B_{1/2} &= ad + bc \mp \gamma'_1 (1 + s_1 u(k)) \mp s'_1 (E_{2p} + \gamma_1 u(k)) \\
 &\quad - (1 + s_1 u(k))(2E_{2p} + 2\gamma_1 u(k) + \Delta), \\
 C_{1/2} &= \pm \gamma'_1 (E_{2p} + \gamma_1 u(k)) - ac + (E_{2p} + \gamma_1 u(k))(E_{2p} + \gamma_1 u(k) + \Delta),
 \end{aligned}$$

where  $u(k) = 2 \cos(k_y a) + 4 \cos(k_x a \sqrt{3}) \cos(k_y a/2)$ . The eigen solutions are same as in equations (3.9) and (3.10) with the modifications in  $A_1$ ,  $B_1$ ,  $C_1$  and  $A_2$ ,  $B_2$ ,  $C_2$  given above.

### 3.3.2.3 Modification due to the in-plane third nearest neighbour hopping energy ( $\gamma_2$ ) and the overlap integral ( $s_2$ ) on the bands of bilayer graphene

The in-plane third nearest neighbour atoms belonging to the other sublattice incorporate changes in  $A_1, B_1, C_1$  and  $A_2, B_2, C_2$  through changes in  $a, b, c$  and  $d$ . Modified  $a, b, c$  and  $d$  appear as

$$a = \gamma_0 f(k) + \gamma_2 f_1(k), \quad b = s_0 f(k) + s_2 f_1(k),$$

$$c = \gamma_0 f^*(k) + \gamma_2 f_1^*(k) \quad \text{and} \quad d = s_0 f^*(k) + s_2 f_1^*(k),$$

where  $f_1(k) = e^{ik_x a/\sqrt{3}} 2 \cos k_y a + e^{-2ik_x a/\sqrt{3}}$ . The eigen solutions in this case are also same as in equations (3.9) and (3.10) but with a different set of  $A_1, B_1, C_1$  and  $A_2, B_2, C_2$  due to differences appearing in  $a, b, c$  and  $d$ . To illustrate the effects of in-plane next nearest neighbours and next to next nearest neighbours on the spectra of bilayer graphene, all the bands are plotted together with the symmetric spectra (full curves) and the spectra with corrections due to nearest neighbour in-plane and interplane overlaps (dashed curves) in figure (3.6). From the plots shown in fig. (3.6) (and also from those not shown here) it is very clear that the presence of any of the parameters ( $s_0, s'_1, \gamma_1, s_1, \gamma_2, s_2$ ) or all of them together introduces asymmetry of different amounts on the symmetric bands due to  $\gamma_0$  and  $\gamma'_1$ . While  $\Delta$  makes the upper conduction and lower valence band positions asymmetric at  $K$  point, others give asymmetry to the bands almost over the whole Brillouin zone. We have already discussed the effects of  $s_0, s'_1$  on the spectra with  $\gamma_0$  and  $\gamma'_1$  in the previous section. Now, we describe the effects due to in-plane next nearest neighbours ( $\gamma_1, s_1$ ) and in-plane next to next nearest neighbours ( $\gamma_2, s_2$ ) on top of  $s_0, s'_1$ . There is no significant change in energy values of the top conduction band and the bottom valence band at the  $K$  point in presence of in-plane next nearest neighbour and next to next nearest neighbour interactions. For the valence bands, the bands from inclusion of next nearest neighbour hopping energy and overlap integral (dotted curves) are nearer to the symmetric bands (full curves) within  $\sim 2$  eV but those due to the inclusion of next to next nearest neighbour interactions (triangles) are closer to the modified bands (dashed curves) due to  $s_0$  and  $s'_1$ . For the conduction bands the scenario is opposite within the same energy range. Beyond that the bands with next nearest neighbour interactions move away from the symmetric bands. Both conduction and the valence bands move upward with respect to the previous band center. The bands with next to next nearest neighbour interactions start moving towards the symmetric bands such that the valence bands for both the cases almost coincide and the conduction bands keep

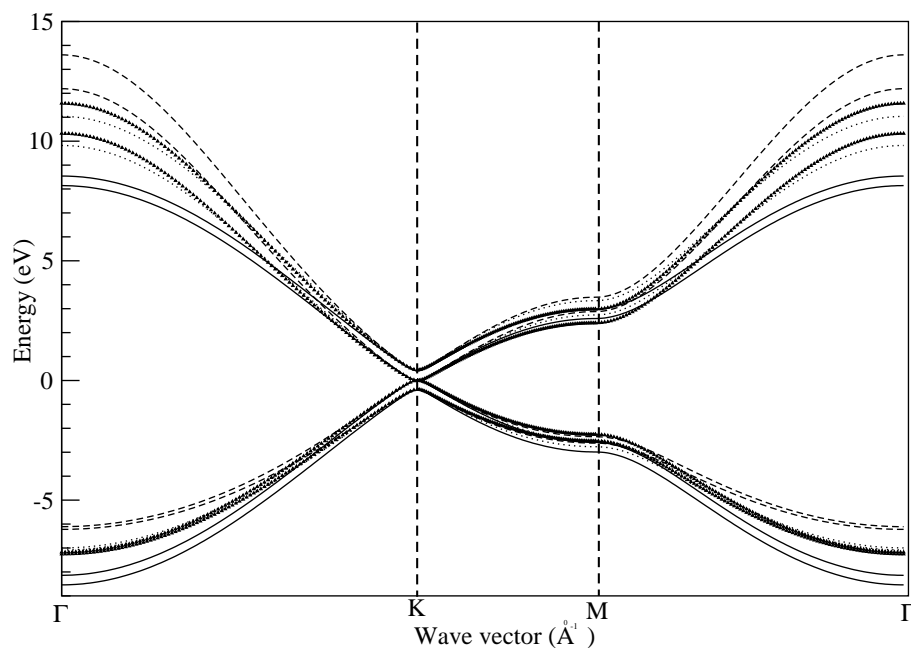


**Figure 3.6:** Electronic dispersions of bilayer graphene in presence of nearest neighbour in-plane and interplane transfer integrals (full curves), nearest neighbour in-plane and interplane transfer integrals, overlap integrals and sublattice asymmetric energy (dashed curves), in-plane next nearest neighbour interactions (dotted curves) and in-plane next to next nearest neighbour interactions (triangles). The parameters used for these bands are given in Table 3.3. The rows numbered 1, 2, 3 and 4 in the table correspond to the curves with full lines, dashed lines, dotted lines and triangles respectively in the figure.

a separation among themselves around  $\Gamma$  point. The values of the parameters used for the plotted bands are given in Table 3.3, the site energy and transfer integrals are in  $eV$ . The rows numbered 1, 2, 3 and 4 in the table correspond to the curves with full lines, dashed lines, dotted lines and triangles respectively in figure (3.6) and (3.10).

**Table 3.3:** Tight binding parameters.  $\gamma_0, \gamma_1, \gamma_2$  and  $\gamma'_1$  are in  $eV$ .

Curves	$E_{2p}$	$\Delta^*$	$\gamma_0$	$\gamma'_1^*$	$\gamma_1$	$\gamma_2$	$s_0$	$s_1^{**}$	$s_1$	$s_2$
1			-2.78	-0.4						
2		0.018	-2.78	-0.4			0.117	0.04		
3	-0.45	0.018	-2.78	-0.4	-0.15		0.117	0.04	0.004	
4	-0.45	0.018	-2.78	-0.4	-0.15	-0.095	0.117	0.04	0.004	0.002

\*taken from reference [18].

\*\*chosen as 10 times less than the magnitude of  $\gamma'_1$ .

In presence of in-plane next nearest neighbour interactions there are three choices of  $E_{2p}$  ( $= 3\gamma_1, 3\gamma_1 - \Delta \pm \gamma'_1$ ) for which the Fermi energy comes at zero. For other choices of  $E_{2p}$  the Fermi level shifts from zero. In presence of in-plane next to next nearest neighbour interactions, the choices of  $E_{2p}$  for which Fermi energy will be at zero, are same as in the case of next nearest neighbour interactions.

### 3.3.3 Tight binding band of graphite

Here we shall present a comparative study of the tight binding dispersions of graphite obtained by following the same prescription used for bilayer graphene. Also, the same set of tight binding parameters (table 3.3) has been utilized. The unit cell of graphite contains four carbon atoms. The collective wave function of the crystal can be written as

$$\Psi_k(r) = \sum_{i=1,..,4} C_i \Psi_i^k, \quad \text{where} \quad (3.11)$$

$$\Psi_i^k(r) = \left(1/\sqrt{N}\right) \sum_{A/B} e^{i\vec{k} \cdot \vec{r}_i^{A/B}} \Phi_{A/B}(r - r_i^{A/B})$$

Proceeding in the same way as described for bilayer graphene, the dispersion relations in presence of nearest neighbour in-plane and interplane overlap, i.e., for finite  $\gamma_0$  and  $\gamma'_1$  only, ignoring the asymmetric energy ( $\Delta$ ), in-plane overlap integral ( $s_0$ ) and the interplane

overlap integral ( $s'_1$ ), are given as

$$E_{1/2}(k) = \mp \frac{1}{2} \left[ \gamma'_1 f_z(k) \mp \left[ \gamma_1'^2 f_z^2(k) + 4\gamma_0^2 g(k) \right]^{1/2} \right]$$

and

$$E_{3/4}(k) = \mp \frac{1}{2} \left[ \gamma'_1 f_z(k) \pm \left[ \gamma_1'^2 f_z^2(k) + 4\gamma_0^2 g(k) \right]^{1/2} \right],$$

where  $f_z(k) = 2 \cos(k_z c/2)$ ,  $c$  being unit cell parameter along z-direction.

In presence of nearest neighbour in-plane overlap integral ( $s_0$ ), interplane overlap integral ( $s'_1$ ), the asymmetric energy ( $\Delta$ ) and in-plane second nearest neighbour hopping ( $\gamma_1$ ) and corresponding overlap integral ( $s_1$ ), the energy dispersions change to

$$E_{1/2}(k) = \left[ -B_1 \pm [B_1^2 - 4A_1 C_1]^{1/2} \right] / 2A_1 \quad (3.12)$$

and

$$E_{3/4}(k) = \left[ -B_2 \pm [B_2^2 - 4A_2 C_2]^{1/2} \right] / 2A_2, \quad (3.13)$$

where

$$\begin{aligned} A_{1/2} &= (1 + s_1 u(k))^2 - bd \pm s'_1 f_z(k)(1 + s_1 u(k)), \\ B_{1/2} &= ad + bc \mp \gamma'_1 f_z(k)(1 + s_1 u(k)) \mp s'_1 f_z(k)(E_{2p} + \gamma_1 u(k)) \\ &\quad - (1 + s_1 u(k))(2E_{2p} + 2\gamma_1 u(k) + \Delta), \\ C_{1/2} &= \pm \gamma'_1 f_z(k)(E_{2p} + \gamma_1 u(k)) - ac + (E_{2p} + \gamma_1 u(k))(E_{2p} + \gamma_1 u(k) + \Delta), \end{aligned}$$

where  $u(k)$ ,  $a$ ,  $b$ ,  $c$  and  $d$  have been defined in the discussion of bilayer graphene.

The energy eigenvalues in presence of in-plane next to next nearest neighbours are same as in equations (3.12) and (3.13) with the modifications in  $A_1$ ,  $B_1$ ,  $C_1$  and  $A_2$ ,  $B_2$ ,  $C_2$  as has been mentioned in the calculation of bilayer graphene. The above results have been depicted in figures 3.7 and 3.8. In figure 3.7 (a) the bands with  $\gamma_0$  and  $\gamma'_1$  only and bands along with ( $s_0$ ), ( $s'_1$ ) and ( $\Delta$ ) have been compared over the entire brillouin zone. It is found that in both the cases there are two bonding  $\pi$  bands and two antibonding  $\pi$  bands in the  $\Gamma MK\Gamma$  plane whereas in  $AHLLA$  plane the  $\pi$  bands are degenerate and so are the  $\pi^*$  bands. Widths of the bands at the  $\Gamma$  point increases and slope the bands changes when ( $s_0$ ) and ( $s'_1$ ) are included. In fig. 3.7 (b) and (c) the effect of the parameters ( $s_0$ ), ( $s'_1$ ) and ( $\Delta$ ) has been clearly shown near the zone corners  $K$  and  $H$  respectively. From the plots shown and from the plots which have not been presented here it is noticed that ( $s_0$ ), ( $s'_1$ ) and ( $\Delta$ ) affect the bands at and near the  $K$  point in a manner exactly similar to that of bilayer graphene.

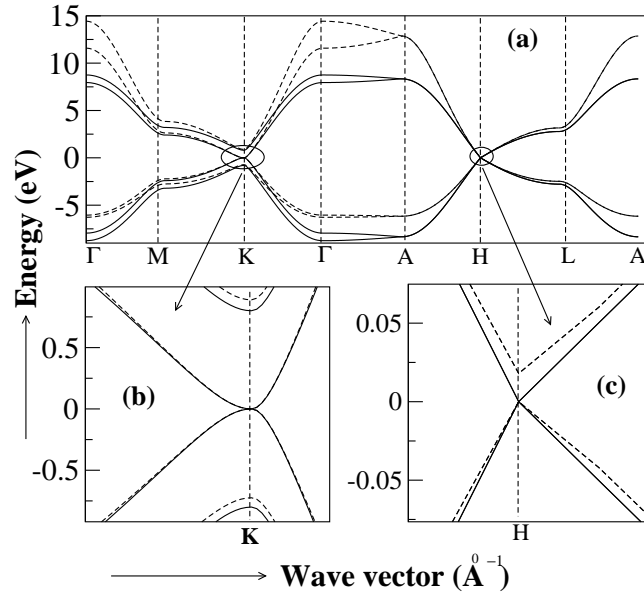


**Figure 3.7:** Electronic spectra of graphite. The upper panel shows the bands along all the high symmetry directions of the graphite Brillouin zone and in the lower panels we have shown the zoomed versions of the spectra near the Brillouin zone corners ( $K$  and  $H$  points). In all the panels the full curves represent the symmetric bands, i.e., bands in presence of nearest neighbour in-plane ( $\gamma_0$ ) and interplane ( $\gamma'_1$ ) hopping energies. In (a) the dashed curves contain information due to the presence of sublattice asymmetry ( $\Delta$ ), nearest neighbour in-plane ( $s_0$ ) and interplane ( $s'_1$ ) overlap integrals. Effects of these parameters at and around the  $K$  and  $H$  points are visible from the lower panel (in (b) and (c) respectively). The relevant parameters are given in rows numbered 1 and 2 in Table 3.3.

The effect of ( $s_0$ ) and ( $s'_1$ ) is not prominent near  $H$  point but away from  $H$  point the slope differs (dashed curves) from those due to  $\gamma_0$  and  $\gamma'_1$  only (full curves) whereas the asymmetric energy term ( $\Delta$ ) opens up a gap at  $H$  point but affects the slope very little. Further, the bands are linear near  $H$  point but parabolic near  $K$  point. In fig. 3.8 we have compared the bands with different neighbours namely, in presence of nearest in-plane and interplane hopping ( $\gamma_0$  and  $\gamma'_1$ , full curves), in-plane and interplane overlap integral, asymmetric energy term ( $s_0$ ,  $s'_1$  and  $\Delta$ , dashed curves), in-plane 2nd nearest neighbour coupling ( $\gamma_1$ ,  $s_1$ , dotted curves) and in-plane 3rd nearest neighbour coupling ( $\gamma_2$ ,  $s_2$ , curves with triangles). Compared to the bands with  $\gamma_0$  and  $\gamma'_1$  only, all other parameters introduce certain amount of asymmetry in slope also in band widths with respect to the zero eigenvalue value. Apart from the exact magnitudes of the band energies, the overall characteristics of the band in presence of various neighbours are similar to that of the corresponding bands of bilayer graphene.

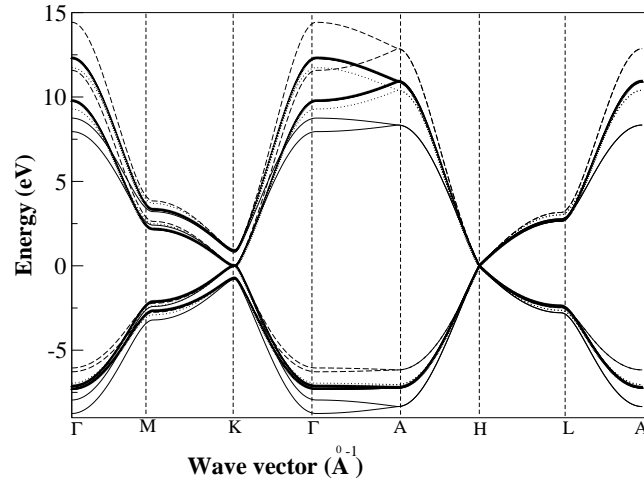


**Figure 3.8:** Electronic dispersions of graphite in presence of nearest neighbour in-plane and interplane transfer integrals (full curves), nearest neighbour in-plane and interplane transfer integrals, overlap integrals and sublattice asymmetric energy (dashed curves), in-plane next nearest neighbour interactions (dotted curves) and in-plane next to next nearest neighbour interactions (triangles). The parameters used for these bands are given in Table 3.3. The rows numbered 1, 2, 3 and 4 in the table correspond to the curves with full lines, dashed lines, dotted lines and triangles respectively in the figure.

### 3.4 Density of states

In fig. 3.9 (a) we have plotted the density of states (due to  $\pi$  band) of graphene for nearest neighbour interaction only without (full curve) and with (dashed-dotted curve) overlap integral correction. It shows that without overlap integral valence and conduction bands

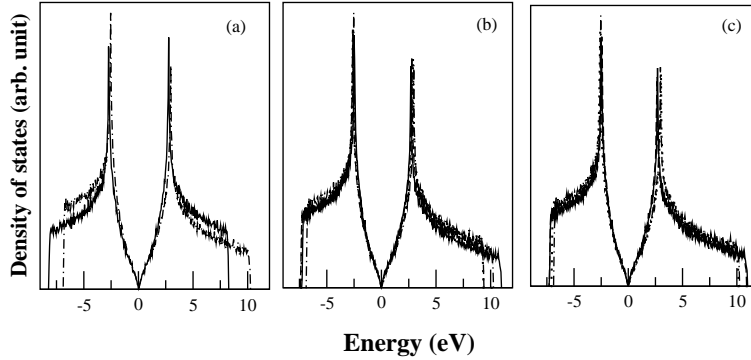


**Figure 3.9:** Density of states of graphene (a) with nearest neighbour hopping but zero overlap integral (full curve) and with nearest neighbour hopping and overlap integral (dashed-dotted curve), (b) derived from the bands in fig. 3.3 (parameters are in Table 3.1). First principle result (full curve), first nearest neighbour interactions (dashed-dotted curve), second nearest neighbour interactions (dotted curve) and third nearest neighbour interactions (dashed curve) and (c) calculated from the bands plotted in fig. 3.4 (parameters are in Table 3.2). First principle result (full curve), first nearest neighbour interactions (dashed-dotted curve), second nearest neighbour interactions (dotted curve) and third nearest neighbour interactions (dashed curve).

are symmetric but in presence of overlap integral width of valence band decreases and that of conduction band increases. Since there are two atoms in each unit cell and each carbon atom has one electron in  $p_z$  state, the valence band is completely filled and hence, the Fermi level lies at the top of the valence band at zero energy which appears at  $K$  and  $K'$  points of the Brillouin zone in energy momentum space. Graphene has zero density of states at Fermi energy and over a very small energy range around zero (i.e.,  $K$  point energy around which energy dispersion is also linear in momentum) the density of states is varying linearly with energy. Due to the flat part of the band near  $M$  point of Brillouin zone Van Hove singularities are arising in density of states. The positions of the singular points are symmetric in absence of overlap term while the singularity moves slightly towards Fermi energy for valence band and goes slightly away from Fermi energy for conduction bands with overlap

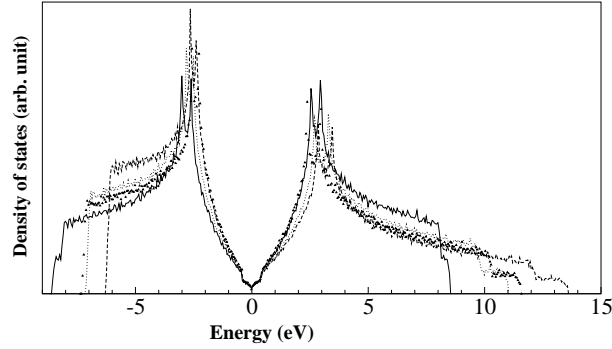


**Figure 3.10:** Density of states of bilayer graphene in presence of nearest neighbour in-plane and interplane transfer integrals (full curves), nearest neighbour in-plane and interplane transfer integrals, overlap integrals and sublattice asymmetric energy (dashed curves), in-plane next nearest neighbour interactions (dotted curves) and in-plane next to next nearest neighbours (triangles). The parameters used in these curves are given in Table 3.3.

( $s_0$ ). In figure 3.9 (b) and (c) the density of states have been plotted as per the bands in fig. (3.3) and (3.4). Here we see that though the density of states is linear near Fermi energy, it becomes asymmetric due to the presence of second and third nearest neighbour interactions. As expected the density of states in presence of third nearest neighbours is matching well with the density of states due to first principle bands when the parameters are chosen freely. In all other cases the band width is changing slightly and positions of Van Hove singularities are changing over a narrow energy range. When compared with ref. [9], the density of states in presence of second nearest neighbours shows a noticeable difference. It is observed that when the second nearest neighbours are chosen for good fitting of low energy part of the spectrum, it gives rise to another Van Hove singularity at conduction band edge but that is removed if the parameters are such that it gives good agreement over the whole energy range. Also, that is suppressed in presence of third nearest neighbour interactions.

The density of states (DOS) of bilayer graphene corresponding to the bands in fig. (3.6) with the parameters in Table 3.3 are shown in figure (3.10). From these curves it is evident that the finite, though small, density of states (DOS) at the zero energy of bilayer graphene remains unaffected due to the presence of factors which lead to asymmetry in bands. Further, the slope of the density of states curves within  $< 0.5 \text{ eV}$  does not change due to the factors mentioned above. Rather, they have prominent effect in bringing asymmetry in band widths. To illustrate, we see that when only nearest neighbour in-plane and

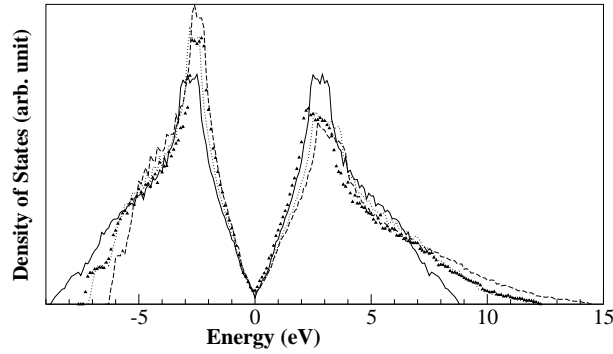


**Figure 3.11:** Density of states of graphite in presence of nearest neighbour in-plane and interplane transfer integrals (full curves), nearest neighbour in-plane and interplane transfer integrals, overlap integrals and sublattice asymmetric energy (dashed curves), in-plane next nearest neighbour interactions (dotted curves) and in-plane next to next nearest neighbours (triangles). The parameters used in these curves are given in Table 3.3.

interplane transfer energies ( $\gamma_0$  and  $\gamma'_1$ ) are there, valence band DOS and conduction band DOS (full curves) are exactly symmetric with respect to the Fermi energy at zero, that is the band widths are same. Also the van Hove singularities are at symmetric positions, the scenario being consistent with the corresponding band structure. As soon as the nearest neighbour in-plane and interplane overlap integrals ( $s_0$  and  $s'_1$ ) are taken into account the valence band (VB) DOS and conduction band (CB) DOS (dashed curves) start becoming asymmetric, i.e., the band widths become different: valence band becomes narrow and conduction band widens. Moreover, the van Hove singularities in VB come closer to  $E_F$  whereas those in CB move away from  $E_F$ . In presence of in-plane second nearest neighbours (dotted curves) CB becomes slightly narrow and VB slightly wide compared to the previous case, though VB is still narrower compared to CB. There is no significant change in the positions of the van Hove singularities in this case when compared with the previous one. In-plane third nearest neighbour interactions do not have much effect on the widths of the bands on top of that of the in-plane second nearest neighbour interactions but bring the van Hove singularities slightly nearer to the Fermi energy. It is also observed that the sublattice asymmetric energy ( $\Delta$ ) does not have any significant effect on the density of states of bilayer graphene.

In figure 3.11 the density of states of graphite corresponding to the bands in fig. (3.8) with the parameters in Table 3.3 are shown. Though little but a finite density of states are present at zero energy. Apart from the nature of the van Hove singularities, the overall appearance of the density of states obtained from the bands due to different coupling param-

eters is similar to those of bilayer graphene (fig. 3.11). There is one van Hove singularity in each band of monolayer graphene and bilayer graphene had two adjacent singularities in each band. In three dimensional graphite it appears as a rise in the density of states rather than the spike like features in monolayer and bilayer graphene, i.e., the singularities become smoother. It needs to be mentioned that all the density of states data presented here are not absolute values, they are arbitrary up to a normalization factor.

### 3.5 Summary and Conclusion

To summarize, we have calculated the electronic spectrum and density of states of graphene including up to third nearest neighbour interactions and got a set of tight binding parameters on the physical ground that the absolute values of the parameters should decrease as one moves from first nearest neighbour towards higher distance. This set of parameters has been used to see the effect of in-plane first nearest neighbour overlap integral ( $s_0$ ), second ( $\gamma_1, s_1$ ) and third ( $\gamma_2, s_2$ ) nearest neighbour interactions on the band structure of bilayer graphene also. We have illustrated the role of these parameters in governing electron-hole asymmetry in the band structure of bilayer graphene within tight binding model. When compared the role of site energy difference ( $\Delta$ ) between A and B sublattices in the same graphene layer on the electronic spectra of single layer graphene and bilayer graphene, a distinct difference is observed between the two systems. Sublattice asymmetry in monolayer graphene introduces a gap in the spectra at the  $K$  point whereas in bilayer it does not induce gap in the spectra, rather it gives an asymmetry in the energy values of the top valence and bottom conduction bands with respect to the energy at which the other two bands are degenerate. Moreover, in presence of  $\Delta$  the gap between top valence and bottom conduction bands at the  $K$  point remains intact to  $\pm\gamma'_1$  which is the separation even without  $\Delta$ . Apart from  $\Delta$  the other important factor which contributes significantly to the values of the top valence and bottom conduction bands at  $K$  point is the interlayer nearest neighbour overlap integral ( $s'_1$ ). Hence, we find that  $E_c$  (top) and  $E_v$  (bottom) are functions of  $\Delta$  and  $s'_1$  both at  $K$  point. Regarding this, Z. Q. Li et al. [18] discuss only the dependence on  $\Delta$ . Our study suggests for the consideration of a model containing both  $\Delta$  and  $s'_1$  for a more accurate determination of  $\Delta$  from experimental results. Further, we observe a considerable change in the slope of the bands in presence of nearest neighbour in-plane and interplane overlap integrals ( $s_0$  and  $s'_1$ ) compared to those with nearest neighbour in-plane and interlayer coupling energies ( $\gamma_0$  and  $\gamma'_1$ ) only. Z. Q. Li et al. [18] have discussed the induction of

electron-hole asymmetry in the slope of valence and conduction bands due to next nearest neighbour interlayer coupling energy ( $\gamma_4$ ) but without overlap integrals. It is noted there that with a finite value of  $\gamma_4$ , two conduction bands are closer and the valence bands are further apart at  $k$  values away from the  $K$  point. We observe that finite values of  $s_0$  and  $s'_1$  also give electron-hole asymmetry in the slope of valence and conduction bands but with an opposite trend compared to the bands with  $\gamma_4$ . With finite values of  $s_0$  and  $s'_1$  the conduction bands move further from each other and the valence bands come closer for  $k$  values away from the  $K$  point. It could be concluded from this comparative study that the combined effect of  $\gamma_4$ ,  $s_0$  and  $s'_1$  could make some balance between the above two cases, may not be a complete balance to get back the symmetric spectra with only  $\gamma_0$  and  $\gamma'_1$  but the degree of electron-hole asymmetry in slope of the bands will get modified nevertheless. A model including  $\gamma_4$ ,  $s_0$  and  $s'_1$ , though very complicated to handle, may lead to more accurate determination of the important parameter like  $\gamma'_1$  when comparing experimental results having asymmetry in electron and hole sides. With in-plane next nearest neighbour interactions ( $\gamma_1$  and  $s_1$ ) the trend of electron-hole asymmetry in slope of bands remains similar as that with  $s_0$  and  $s'_1$  but the asymmetry in valence and conduction band widths near  $\Gamma$  point is reduced compared to that with zero values of  $\gamma_1$  and  $s_1$ . Moreover, in this case if the site energy term  $E_{2p}$  is not chosen properly there will be a shift in Fermi energy [19]. In-plane third nearest neighbour interactions ( $\gamma_2$  and  $s_2$ ) do not affect much on top of in-plane second nearest neighbour interactions except very little change in band widths at  $\Gamma$  point and slight modifications in the slope of the bands. Hence, as far as electron-hole asymmetry in slope of valence and conduction bands is concerned, a Hamiltonian including  $s_0$ ,  $s'_1$  and in-plane second nearest neighbour interactions ( $\gamma_1$  and  $s_1$ ) could be sufficient to interpret experimental results (e.g. the cyclotron resonance data) with asymmetry in electron and hole sides. Also, the in-plane third nearest neighbour interactions could be more useful in determining all the above mentioned parameters by fitting bilayer graphene bands with first principle results or with angle resolved photoemission data over the whole Brillouin zone. Within similar formalism, we have also shown the effects of in-plane nearest, next nearest and next to next nearest neighbour couplings along with the nearest interlayer coupling on the band structure of three dimensional graphite. Near  $K$  point the effect of these parameters mimics those of bilayer graphene whereas at  $H$  point a gap is opened up by the asymmetric energy  $\Delta$  but  $s_0$  and  $s'_1$  incorporate only changes in slope of the bands.

### 3.6 Derivation of the electronic dispersions of graphene in presence of different neighbours

In this last section, as mentioned earlier, we present some details of the derivations of the dispersion relations of graphene in presence of various nearest neighbours. The corresponding matrix elements in equation (3.4) are computed here in presence of different neighbours.

1. For nearest neighbour approximation, we have

$$H_{AA} = (1/N) \sum_A e^{i\vec{k}\cdot(\vec{r}_A-\vec{r}_A)} \langle \Phi_A(r-r_A) | H | \Phi_A(r-r_A) \rangle \approx E_{2p},$$

$$S_{AA} = \langle \Phi_A(r-r_A) | \Phi_A(r-r_A) \rangle = 1,$$

because the wave functions are normalized;

$$H_{AB} = \gamma_0 \sum_B e^{i\vec{k}\cdot(\vec{r}_B-\vec{r}_A)} = \gamma_0 f(k), \quad S_{AB} = s_0 f(k) \text{ where}$$

$$\gamma_0 = (1/N) \sum_A \langle \Phi_A(r-r_A) | H | \Phi_{B_1}(r-r_{B_1}) \rangle,$$

$$s_0 = (1/N) \sum_A \langle \Phi_A(r-r_A) | \Phi_{B_1}(r-r_{B_1}) \rangle, \text{ and}$$

$$f(k) = e^{ik_x a/\sqrt{3}} + 2e^{-ik_x a/2\sqrt{3}} \cos k_y a/2.$$

Hence

$$E_0 = E_{2p}, \quad E_1 = 2\gamma_0 s_0 |f(k)|^2, \quad E_2 = E_{2p}^2 - \gamma_0^2 |f(k)|^2 \text{ and,}$$

$$E_3 = 1 - s_0^2 |f(k)|^2 \text{ with}$$

$$|f(k)|^2 = g(k) = 1 + 4 \cos^2(k_y a/2) + 4 \cos(\sqrt{3}k_x a/2) \cos(k_y a/2),$$

leading to

$$E^\pm(k) = \frac{\left[ (E_{2p} - s_0 \gamma_0 g(k)) \pm (\gamma_0 - s_0 E_{2p}) \sqrt{g(k)} \right]}{[1 - s_0^2 g(k)]}. \quad (3.14)$$

From the secular determinant the dispersion can alternatively be written as [8]

$$E^\pm(k) = \left( E_{2p} \pm \gamma_0 \sqrt{g(k)} \right) / \left( 1 \pm s_0 \sqrt{g(k)} \right). \quad (3.15)$$

2. For second nearest neighbour approximation we need the matrix elements  $H_{AA}$  and  $S_{AA}$  only as these two are affected by next nearest neighbours. These are

$$\begin{aligned} H_{AA} &= \int \Psi_A^{*k}(r) H \Psi_A^k(r) d\vec{r} = E_{2p} + \gamma_1 u(k), \\ S_{AA} &= 1 + s_1 u(k), \text{ where} \\ u(k) &= 2 \cos(k_y a) + 4 \cos(k_x a \sqrt{3}) \cos(k_y a/2), \\ \gamma_1 &= (1/N) \sum_{A_2} \langle \Phi_{A_2}(r - r_{A_2}) | H | \Phi_A(r - r_A) \rangle, \text{ and} \\ s_1 &= (1/N) \sum_{A_2} \langle \Phi_{A_2}(r - r_{A_2}) | \Phi_A(r - r_A) \rangle. \end{aligned}$$

Putting all the above elements in the secular determinant we get

$$E^\pm(k) = \left[ E_{2p} + \gamma_1 u(k) \mp \gamma_0 \sqrt{g(k)} \right] / \left[ 1 + s_1 u(k) \mp s_0 \sqrt{g(k)} \right]. \quad (3.16)$$

3. In presence of third nearest neighbours only the matrix elements  $H_{AB}$  and  $S_{AB}$  get changed but  $H_{AA}$  and  $S_{AA}$  remain unchanged. Hence

$$\begin{aligned} H_{AB} &= \int \Psi_B^{*k}(r) H \Psi_A^k(r) d\vec{r} = \gamma_0 f(k) + \gamma_2 v(k), \\ S_{AB} &= s_0 f(k) + s_2 v(k), \text{ where} \\ \gamma_2 &= (1/N) \sum_A \langle \Phi_A(r - r_A) | H | \Phi_{B_3}(r - r_{B_3}) \rangle, \\ s_2 &= (1/N) \sum_A \langle \Phi_A(r - r_A) | \Phi_{B_3}(r - r_{B_3}) \rangle \text{ and} \\ v(k) &= e^{ik_x a / \sqrt{3}} 2 \cos k_y a + e^{-2ik_x a / \sqrt{3}}. \end{aligned}$$

Therefore, expressions for  $E_1$ ,  $E_2$ ,  $E_3$  are

$$\begin{aligned}
 E_1 &= 2s_0\gamma_0g(k) + (s_0\gamma_2 + \gamma_0s_2)t(k) + 2s_2\gamma_2g(2k) \\
 E_2 &= [E_{2p} + \gamma_1u(k)]^2 - [\gamma_0^2g(k) + \gamma_0\gamma_2t(k) + \gamma_2^2g(2k)] \\
 E_3 &= [1 + s_1u(k)]^2 - [s_0^2g(k) + s_0s_2t(k) + s_2^2g(2k)], \text{ where} \\
 g(2k) &= 1 + 4\cos^2(k_y a) + \cos(\sqrt{3}k_x a)\cos(k_y a) \text{ and} \\
 t(k) &= 2\cos(k_x a\sqrt{3}) + 4\cos(k_y a) + 4\cos(k_y a/2)\cos(k_x a\sqrt{3}/2) \\
 &\quad + 8\cos(k_y a)\cos(k_y a/2)\cos(k_x a\sqrt{3}/2).
 \end{aligned}$$

# Bibliography

- [1] S. Reich, J. Maultzsch, C. Thomsen and P. Ordejón, *Phys. Rev.* **B66**, 035412 (2002).
- [2] B. T. Kelly, *Physics of Graphite* (Applied Science Publishers, London and New Jersey, 1981).
- [3] P. R. Wallace, *Phys. Rev.* **71**, 622 (1947).
- [4] Novoselov, K. S., A. K. Geim, S. V. Morozov, D. Jiang, Y. Zhang, S.V. Dubonos, I.V. Gregorieva and A. A. Firsov, *Science* **306**, 666 (2004).
- [5] B. Partoens and F. M. Peeters, *Phys. Rev.* **B74**, 075404 (2006).
- [6] A. Bostwick, T. Ohta, T. Seyller, K. Horn and E. Rotenberg, *Nature Physics* **3**, 36-40 (2007).
- [7] R. Roldán, M. P. López-Sancho and F. Guinea “Effect of electron-electron interaction on the Fermi surface topology of doped graphene”, arXiv:0710.3034v1 [cond-mat.str-el] (2007).
- [8] R. Saito, G. Dresselhaus and M.S. Dresselhaus: *Physical Properties of Carbon Nanotubes* (chap.2 and 4) (Imperial College Press, London, 1998).
- [9] A. H. Castro Neto, F. Guinea, N. M. R. Peres, K. S. Novoselov and A. K. Geim, *Rev. Mod. Phys.* **81**, 109 (2009).
- [10] Edward McCann, *Phys. Rev.* **B74**, 161403(R) (2006).
- [11] Hongki Min, B.R. Sahu, Sanjay K. Banerjee, A.H. MacDonald, *Phys. Rev.* **B75**, 155115 (2007).
- [12] E. V. Castro, K. S. Novoselov, S. V. Morozov, N. M. R. Peres, J. M. B. Lopes dos Santos, J Nilsson, F. Guinea, A. K. Geim, and A. H. Castro Neto, *Phys. Rev. Lett.* **99**, 216802 (2007).
- [13] J. B. Oostinga, H.B. Heersche, X Liu, A.F. Morpurgo and L. M.K. Vandersypen, *Nature Materials* **7** 151-157 (2007).
- [14] Y. Zhang, Tsung-Ta Tang, C. Girit, Z. Hao, Michael C. Martin, A. Zettl, Michael F. Crommie, Y. Ron Shen and F. Wang, *Nature* **459**, 820-823 (2009).

- [15] T. Ohta, A. Bostwick, T. Seyller, K. Horn, and E. Rotenberg, *Science* **313**, 951 (2006).
- [16] L.M. Malard, J. Nilsson, D.C. Elias, J.C. Brant, F. Plentz, E.S.Alves, A.H. Castro Neto and M. A. Pimenta, *Phys. Rev.* **B76**, 201401(R) (2007).
- [17] A. Grüneis, C. Attacalite, L. Wirtz, H. Shiozawa R. Saito, T. Pichler, A. Rubio, “Tight-binding description of the quasiparticle dispersion of graphite and few-layer graphene”, arXiv:0808.1467v2 [cond-mat.mtrl-sci] (2008).
- [18] Z. Q. Li, E. A. Henriksen, Z. Jiang, Z. Hao, M. C. Martin, P. Kim, H. L. Stormer, and D. N. Basov, *Phys. Rev. Lett.* **102**, 037403 (2009).
- [19] A. R. Wright, Feng Liu, and C. Zhang, “Effect of next-nearest neighbor coupling on the optical spectra in bilayer graphene”, arXiv:0907.0504v1 [cond-mat.mtrl-sci] (2009).
- [20] J. W. McClure, *Phys. Rev.* **108**, 612 (1957).

# 4

## Band Structure of single crystal graphite and HOPG from ARPES and KRIPES

### 4.1 Introduction

The recent discovery of zero dimensional fullerene, one dimensional carbon nanotubes and the research activities on the very recently found two dimensional material graphene have given an impetus to the reinvestigation of some of the exotic and fundamentally important physical properties of carbon based materials. Like graphene, which shows a peculiar low energy electronic spectrum due to its sublattice structure, graphite also has a linear dispersion near the  $H$  point along with its quadratic band near the  $K$  point of its Brillouin zone [1]. Many physical properties like the transport and magnetic behaviours, in single crystal graphite and in highly oriented pyrolytic graphite (HOPG) [2–5] are not well understood and might be governed by the carrier dynamics near their Fermi energy ( $E_F$ ). The near  $E_F$  electronic structure on both the occupied and unoccupied sides are important for a consolidated understanding of the physics behind these properties. There have been many experimental studies [6–10] earlier on the electronic structure of the occupied states of graphite in which various bands were unambiguously identified using monochromatic light sources or synchrotron radiation. There are lot of PES studies (angle integrated and angle resolved) on HOPG and single crystal graphite along with many intercalated compounds of graphite. Although, the electronic structure studies on graphite seems to be complete, recent works have shown several new results owing mainly to the improved experimental techniques. On the other hand, along with ARPES study on graphite to determine its occupied band structure, a significant amount of effort was also put to study the unoccu-

pied band structure of it using  $k$ -resolved inverse photoelectron spectroscopy. But only a few studies [21] have been reported recently on the electronic structure of the unoccupied states.

Angle resolved photoelectron spectroscopy (ARPES) has been quite successful in elucidating the momentum-resolved valence band electronic structure of the graphite systems [11–16]. This spectroscopy gives a direct measurement of the spectral functions which reflect the quasiparticle lifetime and self-energies. Earlier ARPES studies on single crystal graphite have shown the energy dispersion of  $\pi$  and  $\sigma$  bands along different in-plane and out of plane symmetry directions of graphite Brillouin zone [12, 14, 15]. It was also shown that there exists some anomalous non-dispersive states very close to  $E_F$  over a small momentum region near the  $K$  point in the Brillouin zone which were attributed to edge-localized states and dangling bonds present on the surface [12]. ARPES studies on HOPG have reported that this azimuthally disordered material can exhibit energy dispersion along the radial direction with a loss of information in the azimuthal direction [16–19] and also shown that sharp quasiparticle dispersions can coexist with its in-plane randomness [16].

The unoccupied electronic states of single crystal graphite [20, 21] and HOPG [22, 23, 25] have been studied earlier using  $k$ -resolved inverse photoemission spectroscopy (KRIPES) which gives the wave-vector resolved unoccupied electronic structure of graphite. This spectroscopy has the ability to probe the energy region between the  $E_F$  and the vacuum level ( $E_V$ ) which is inaccessible by direct photoemission spectroscopy. In this chapter, we have compared the band structure of single crystal (natural) graphite and HOPG, particularly their near  $E_F$  electronic states along the high symmetry directions of their Brillouin zones. We have used ARPES to probe the occupied states and KRIPES to probe the unoccupied states. We have also compared the  $\pi$  bands of graphite obtained from the ARPES experiment with the tight binding  $\pi$  bands calculated in the previous chapter.

## 4.2 Experimental

Angle resolved ultraviolet photoemission data were collected using an AR65 hemispherical energy analyzer with a resolution of  $\sim 50$  meV at a pass energy of 1 eV and an acceptance angle of  $\pm 1^\circ$ . The analyzer is mounted on a double axes goniometer and can rotate independently along two planes mutually perpendicular to the sample surface. The rotational degrees of freedom are designated by  $\theta$  and  $\phi$ . Angular resolutions for both the directions are  $\pm 0.1^\circ$ . A high intensity vacuum ultraviolet source (HIS 13) with a photon flux of the

order of  $10^{16}$  photons/s/sr at the HeI (21.2 eV) line and a beam spot size of 2.5 mm diameter was used. The samples studied were natural graphite commercially obtained from NGS Naturgraphit GmbH and highly oriented pyrolytic graphite of grade SPI-1 commercially supplied by SPI Supplies Division of Structure Probe, Inc. The angular spread of the c-axes of the crystallites for the above mentioned grade of HOPG is  $\sim 0.4^\circ \pm 0.1^\circ$ . Both natural single crystal graphite and HOPG samples were cleaved insitu using post technique under a base vacuum of  $\sim 2.5 \times 10^{-10}$  mbar in the preparation chamber and were immediately transferred to the analysis chamber. The orientations of the crystal surfaces were determined by low energy electron diffraction (LEED) performed in the analysis chamber at a base pressure of  $\sim 2.8 \times 10^{-11}$  mbar. Before doing photoemission experiment the samples were freshly cleaved again to avoid any unwanted surface contamination due to LEED experiment on the samples. The Fermi energy was calibrated using the Fermi edge spectra of silver, freshly evaporated on to a sample holder.

The inverse photoemission experiments were carried out with an KRIPEs spectrometer in the isochromat mode with a mean photon energy of 9.9 eV. The spectrometer consists of a low-energy Stoffel-Johnson type electron gun and a band-pass Geiger-Müller type photon detector with acetone gas filling and  $\text{CaF}_2$  window (acetone/ $\text{CaF}_2$ ) [26]. The overall energy resolution of the spectrometer is 0.55 eV. The spectra have been normalized by dividing the photon counts from the acetone/ $\text{CaF}_2$  detector by the incident electron beam current, as in our other works [27]. The system is also equipped with a low energy electron diffraction (LEED) unit which was used to determine the orientation of single crystal graphite and to check the surface cleanliness of HOPG sample by looking at the sharpness of its diffraction ring. Both the samples were cleaved insitu with an adhesive tape at a pressure of  $\sim 1.6 \times 10^{-8}$  mbar in the preparation chamber. The experiments were performed at a base pressure of  $\sim 6 \times 10^{-10}$  mbar in the main chamber. Momentum-resolved spectra were collected by rotating the sample (say by  $\theta^\circ$ ) with respect to the incident electron beam at an angular interval of  $5^\circ$ . The Fermi energy was calibrated by using the spectrum taken on a polycrystalline silver sample.

### 4.3 Results and Discussions

Figure 4.1(a) shows the ARPES spectra of the single crystal graphite sample taken at room temperature along the  $\Gamma K$  direction of its Brillouin zone (marked by the thick arrow in inset) by using He I excitation line. The high symmetry directions of the sample were

determined from its low energy electron diffraction (LEED) pattern (fig. 4.2) having six bright spots which indicates the hexagonal symmetry of the surface. It can be seen from the figure that the spectrum at the  $\Gamma$  point has three weak features at  $\sim 2.8$  eV,  $\sim 8.3$  eV and  $\sim 10.3$  eV. The peak at around 8.3 eV could be from the bottom of the lower  $\pi$  band. Along the  $\Gamma K$  direction we find two dispersing bands; one moving towards higher binding energy up to  $\sim 9.8$  eV and the other dispersing strongly towards Fermi energy. Earlier reported ARPES measurements [11, 12] and band structure calculations [28–31] have identified this strongly dispersing band as the valence  $\pi$  band. Near about the  $K$  point of the Brillouin zone, this band splits into the upper  $\pi$  band ( $\pi_1$ ) and the lower  $\pi$  band ( $\pi_2$ ). In order to estimate the splitting between the two  $\pi$  bands at the  $K$  point, spectrum was taken over a smaller energy range at that point (spectrum marked as K in figure 4.1(c)). To visualize the dispersion of the near  $K$ -point features more clearly, a few spectra at and around the  $K$  point along the cut marked as A (in the inset) over an energy range of  $\sim 3.5$  eV are shown in fig. 4.1(c). The splitting between the two  $\pi$  bands at the  $K$  point is  $\sim 0.5$  eV, comparable to the value reported earlier [11, 13–15] in the literature. This splitting arises due to the coupling between adjacent layers in graphite. In figure 4.1(d) the  $K$ -point spectra over a very small energy range ( $\sim 0.6$  eV) taken at room temperature and at 77 K are compared. It is observed that the spectral feature sharpens at lower temperature. This spectral feature could be ascribed to the formation of quasiparticles due to the coupling of  $\pi$  electrons with the collective excitations such as phonon. The sharpening of this feature shows the increased lifetime of these quasiparticles at low temperature. Presence of the quasiparticles demonstrate the strong electron-phonon coupling in graphite. A recent study by Sugawara et al [13] on kish graphite has reported about a sharp peak appearing at low temperature very close to the  $K$  point within 200 meV below  $E_F$  and it becomes extremely sharp at the  $K$  point. This strong enhancement of spectral intensity is explained by the formation of quasiparticles due to coupling of  $\pi$  electrons with some collective excitation, namely phonon. Ref. [13] has also found the existence of another sharp peak above  $E_F$  originating from antibonding  $\pi^*$  band and the estimated separation between the peaks due to  $\pi$  and  $\pi^*$  bands at the  $K$  point at 260 K temperature is 25 meV. In our spectrum at the  $K$  point taken at room temperature the quasiparticle peak due to  $\pi^*$  band is not visible, could be due to poor instrumental resolution. They have shown that the linear energy dependence of this quasiparticle scattering rate indicates a non Fermi-liquid behaviour of electrons in graphite. In figure 4.1(b), the dispersion of the  $\pi$  band towards  $E_F$  is presented graphically by plotting the photoemission intensity against the energy and momentum component parallel to the

surface.

The ARPES spectra taken along  $\Gamma M$  direction of the Brillouin zone of the single crystal graphite sample is shown in figure 4.3(a). The spectra show an intense peak moving up to  $\sim 2.8$  eV below the Fermi energy. Apart from this, there is one feature at  $\sim 10.3$  eV which does not disperse with changes in emission angles whereas another feature at  $\sim 7.8$  eV appearing at higher emission angles disperses towards lower binding energy as the emission angles decrease. It can be seen from Fig. 4.3(a) that at some point the broad hump, present in the  $\Gamma$  point spectrum, splits into two bands: one goes towards higher binding energy up to  $\sim 7.8$  eV and the other disperses up to  $\sim 2.8$  eV below Fermi energy near the  $M$  point of Brillouin zone. Dispersion of this band is clearly visible in the intensity plot shown in figure 4.3(b). It is also observed that the feature at  $\sim 2.8$  eV becomes very intense and remains non-dispersive over a certain angular range near the  $M$  point, consistent with the reported dispersion near this point.

In order to compare our results in different high symmetry directions, the experimental data have been superimposed (Fig. 4.4) on a theoretically calculated band structure of graphite derived from first principle calculations [29] of Willis et al. The overall agreement of the experimental valence band features with calculated band structure in various symmetry directions,  $\Gamma K$  and  $\Gamma M$ , is good with some quantitative differences, although the differences are consistent with earlier experimental works [11, 12]. As mentioned earlier, at the  $K$  point, two  $\pi$  bands occur near  $E_F$  with a splitting of  $\sim 0.5$  eV. At higher emission angles they disperse towards higher binding energy in the second Brillouin zone ( $k_{\parallel} > 1.70\rho A^{-1}$ ). We find that one of these two  $\pi$  bands undergoes a dispersion towards higher binding energy from the  $K$  point towards the  $\Gamma$  point and almost coincides with the lower  $\pi$  band. It is observed that in both  $\Gamma K$  and  $\Gamma M$  directions the intensity of this peak is quite weak below  $k_{\parallel} = 0.6\rho A^{-1}$ . Moreover, along  $\Gamma K$  we have found a dispersive band which originates from weakly intense features but does not superpose onto any calculated bulk band and is almost parallel to the  $\sigma_1$  band. It has a relatively lower binding energy compared to the  $\sigma_1$  band. In the  $\Gamma M$  direction also our results are in good agreement with the calculations on the dispersing lower  $\pi$  band and the upper most  $\sigma$  band. The top of the  $\pi$  band at the  $M$  point ( $k_{\parallel} = 1.47\rho A^{-1}$ ) appears at  $\sim 2.8$  eV. Apart from these dispersing bands we find two extra non-dispersive features which are absent in the calculated valence band structure [31, 32]. All along the  $K\Gamma M$  direction these weak features appear at  $\sim 2.8$  eV and  $\sim 10.3$  eV. The 2.8 eV feature has been attributed to isolated carbon atoms on the surface or to surface states [6, 8, 10] while the 10.3 eV feature to conduction states [9] or

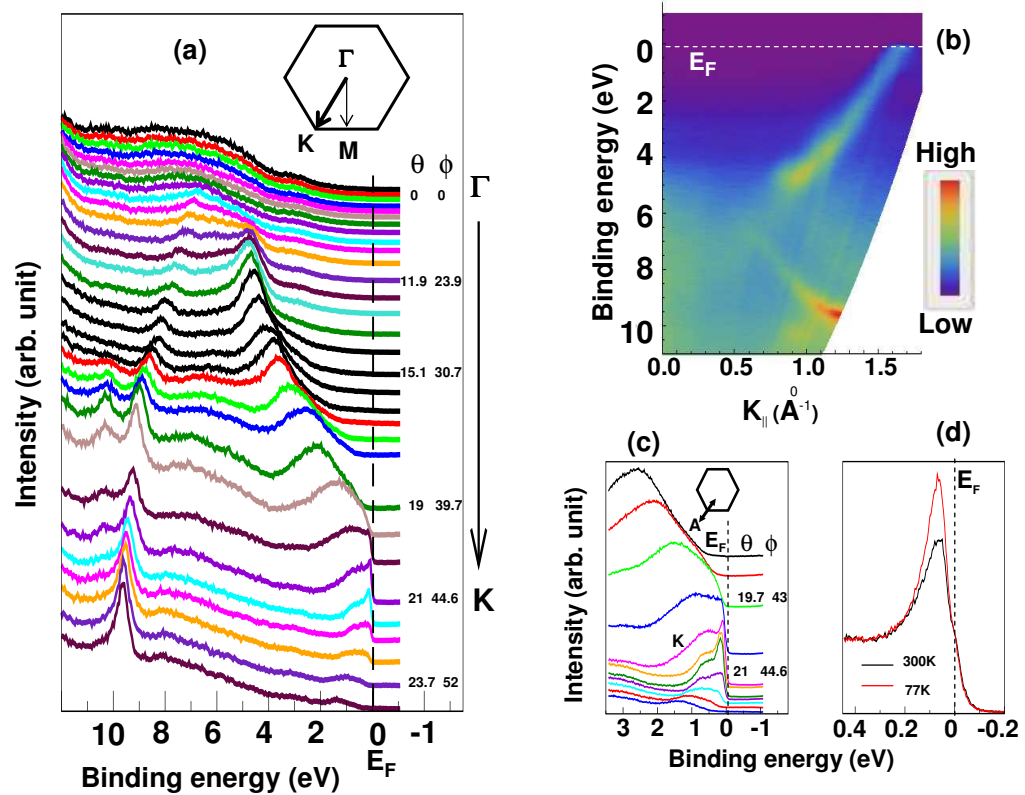


**Figure 4.1:** (a) The raw photoemission data from single crystal graphite along the  $\Gamma K$  direction of its Brillouin zone. Shown in the inset is the two dimensional brillouin zone of graphite. The emission angles  $\theta$  and  $\phi$  (in degree) for some of the spectra are indicated beside the spectra. In (b) the photoemission intensity plot as a function of binding energy and  $k_{\parallel}$  derived from the spectra in (a) is shown. The spectra along the cut A of the brillouin zone through the  $K$  point over a small energy range near Fermi energy are shown in (c). In (d) the spectra over a very small energy range at the  $K$  point at two different temperatures (300 K (black curve) and 77 K (red curve)) are compared.

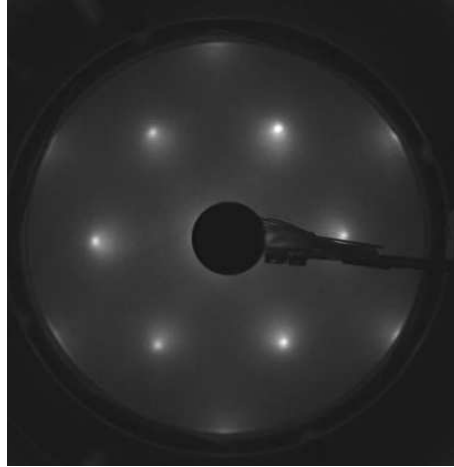


**Figure 4.2:** The low energy electron diffraction pattern of single crystal graphite.

a momentum broadening at regions of high densities of final states [7]. Law et al [7] have explained these nondispersive features by plotting them on a kinetic energy vs  $k_{\parallel}$  diagram and then compared them with a conduction band calculation. They observed coincidence of these bands with some conduction bands having large effective mass at  $\Gamma$  point or at some other  $k$  values which leads to the conclusion that these bands are related to regions of high densities of final states. On the other hand, it is argued in ref. [8, 10] that along with direct photoemission there are indirect transitions also with conservation of energy. This process usually gives the energy of initial states with high density in the valence band. The nondispersive feature at  $\sim 3$  eV appears in measurements with varying photon energy also, indicating that it must be an initial-state feature. The binding energy at  $M$  point has almost a similar value and the dispersionless feature could be due to non- $k$ -conserving transitions from the high density of states region at  $M$  point at that binding energy.

In figure 4.5 we have compared the  $\pi$  bands of graphite obtained from ARPES experiment with the tight binding  $\pi$  bands of graphite calculated in the previous chapter using the coupling parameters listed in table 3.3. In the previous chapter, in figs. 3.7 and 3.8 we have shown the tight binding  $\pi$  bands of graphite over the two symmetry planes of its Brillouin zone namely,  $\Gamma MK\Gamma$  and  $ALHA$  planes. In this chapter we have compared our experimental  $\pi$  bands with our calculated  $\pi$  bands in the  $\Gamma MK\Gamma$  plane only. The logic behind this choice is that an experimental spectrum from the  $H$  point should contain only a single feature at the Fermi level whereas the obtained experimental results show two features near Fermi energy with a separation of  $\sim 0.5$  eV. This indicates that the spectra are not from the  $ALHA$  plane, rather they might be from the  $\Gamma MK\Gamma$  plane. The red and green circles in

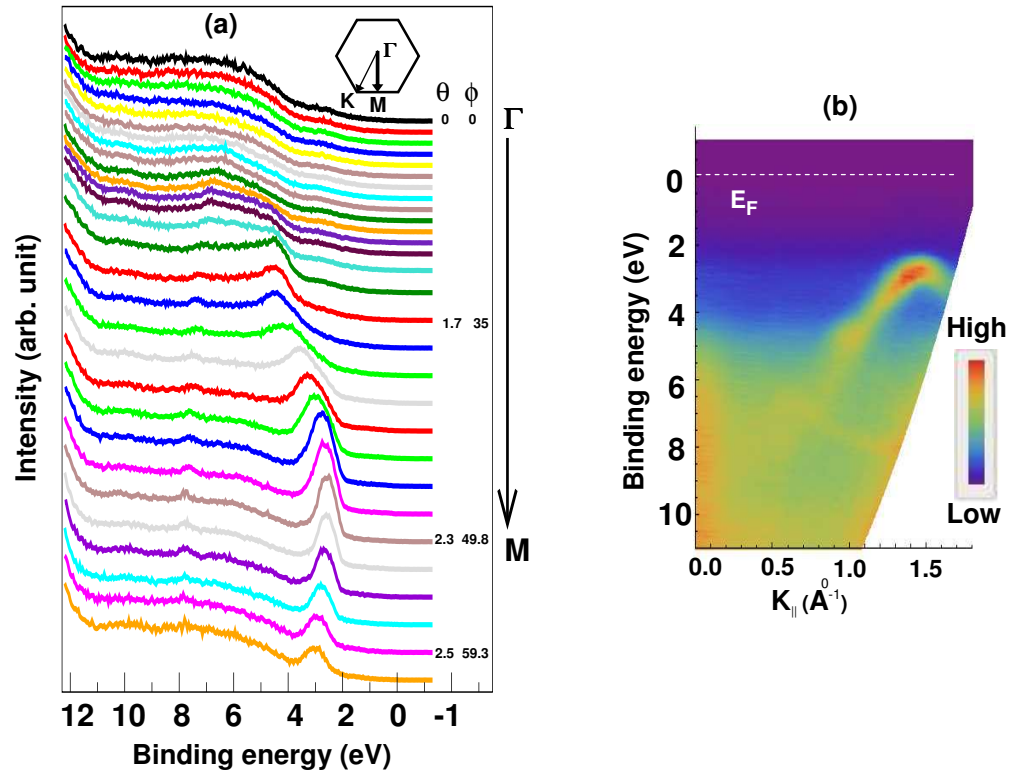


**Figure 4.3:** (a) The spectra along the  $\Gamma M$  direction of graphite Brillouin zone. The emission angles in degree for some of the spectra are marked beside the spectra. (b) The intensity map of the spectra shown in (a) as a function of binding energy and  $k_{||}$ .

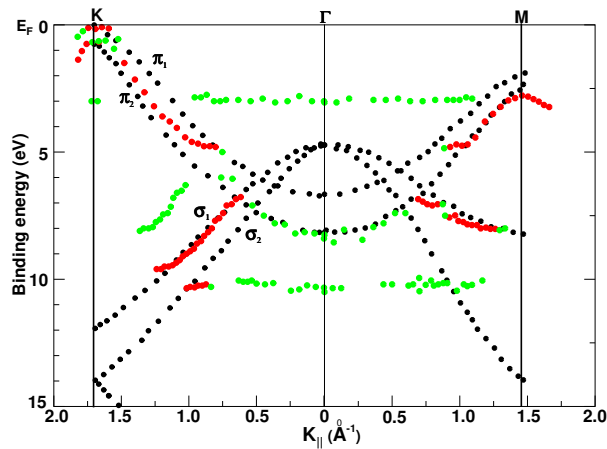


**Figure 4.4:** Energy versus momentum component parallel to the sample surface ( $E(k) \sim k_{\parallel}$ ) for all the strong (red circles) and weak (green circles) peaks of the experimental results in figs. 4.1(a) and 4.3(a). They have been plotted along with a theoretical band structure (black circles) of graphite in the  $\Gamma K$  and  $\Gamma M$  directions of the Brillouin zone.

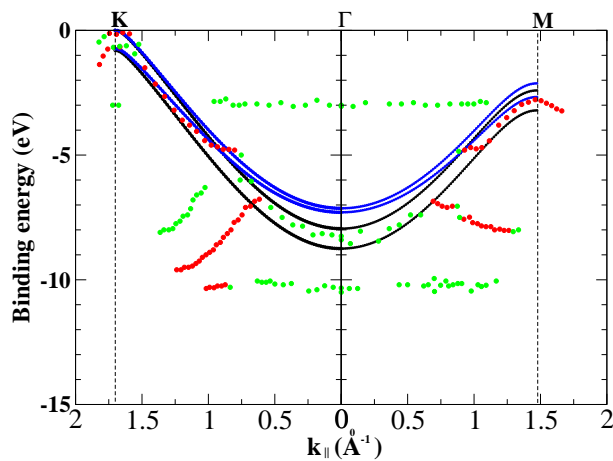


**Figure 4.5:** The red and green circles represent the strong and weak features respectively from ARPES experiment, the black curves are calculated tight binding bands due to nearest neighbour in-plane and interplane hopping ( $\gamma_0$  and  $\gamma'_1$ ) only and the blue curves are obtained by considering both the hopping and overlap integrals along with the coupling up to in-plane third nearest neighbours.

the figure are the strong and weak features respectively from ARPES experiment, the black curves contain informations of nearest neighbour in-plane and interplane hopping ( $\gamma_0$  and  $\gamma_1'$ ) only and the blue curves are obtained by considering both the hopping and overlap integrals along with the coupling up to in-plane third nearest neighbours. The in-plane parameters were found by fitting our tight binding model up to third nearest neighbour with a first principle result [33]. The parameters were determined on the ground that they should decrease in magnitude with respect to distant neighbours. In this plot our intention is to check the reproducibility of these energy dispersions with our own ARPES band mapping. We notice that there is an overall matching of the experimental bands with the first neighbour tight binding bands, in particular this is prominently visible near the  $\Gamma$  point. Near the  $M$  point the experimental points are more close to the band with third nearest neighbours and very close to the  $K$  point the first neighbour (black curves) and the third neighbour (blue curves) bands differ very little and the experimental points are going well with both the curves.

In figure 4.6(a), we present the normalized spectra in a radial direction (marked by arrow in the LEED pattern shown in the inset) of the Brillouin zone of HOPG. The photoemission intensity map as a function of the binding energy and the in-plane component of the crystal momentum in this direction is displayed in Fig. 4.6(b). In these figures, we find a clearly visible dispersing feature, becoming very prominent over certain angular range (around  $k_{\parallel} = k_M$ ). Further, at higher emission angles (near the  $K$  point) some density of states appears near the Fermi energy and moves up to  $E_F$ . We assign the intense feature at  $\sim 2.8$  eV to the valence  $\pi$  band at the  $M$  point and the density of states moving towards Fermi energy to the valence  $\pi$  band at the  $K$  point of the Brillouin zone, in accordance with the earlier reports [16–19]. The presence of  $M$  and  $K$  points like features in the same radial direction of the Brillouin zone indicates that the  $\Gamma M$  and  $\Gamma K$  directions are superposed in HOPG due to its inherent in-plane misorientations. Here the  $\pi$  band feature at  $K$  point is not as prominent as that of single crystal graphite because of the azimuthal disorder. We have taken the photoemission spectra along three different radial directions which show similar features indicating that the photoemission peaks have dispersion in the radial direction but do not have any azimuthal dependence. Similar to the single crystal graphite, along with the dispersing band we notice a feature at  $\sim 2.9$  eV which does not disperse at all and another at  $\sim 10.2$  eV which disperses within  $\sim 300$  meV. In contrast to single crystal graphite, HOPG has another non-dispersive band over the entire momentum range at  $\sim 6$  eV. Like in single crystal, the 2.9 eV non-dispersive peak could well be attributed to

the isolated carbon atoms on the surface or to surface states or grain boundaries. Lanzara et al [16] have observed such nondispersive features in HOPG at 2.9 eV, 4.3 eV and 7.8 eV and suggested their origin to be the non- $k$ -conserving transitions in the photoemission process or the elastic scattering of electrons in either the initial state or the final state by inhomogeneity or disorder.

As mentioned earlier, emission at angles near the  $K$  point show some states near  $E_F$  coming from the valence  $\pi$  band. Due to random in-plane orientations of the crystallites in HOPG the intensity of this structure is weak, although visible in fig. 4.6 as well as in the intensity plots along different radial directions (spectra along other radial directions are not shown here). In figure 4.7 we show this near  $E_F$  feature in detail. The  $\Gamma$  and the  $K$  point spectra are compared in Fig. 4.7(a). It should be noted from fig. 4.7(b) and (c) that along with the sharp peak at  $\sim 2.8$  eV there exists a broad feature ( $\sim 1.7$  eV wide) near the  $E_F$  in the  $K$  point spectrum. Fig. 4.7(d) clearly shows this feature, which could be identified as the upper  $\pi$  band of graphite. Fig. 4.7(d) further shows that this weak peak is dispersing back towards higher binding energy at higher emission angles. In figure 4.7(e) the normalized spectra of the HOPG sample taken at 77 K temperature at and around the  $K$  point is shown. Lowering of temperature does not result in any significant change in the spectra except for a slight enhancement of the intensity of the peak.

In figure 4.8 we present the angle resolved inverse photoemission spectra taken on the HOPG and single crystal samples at room temperature. Fig. 4.8(a) shows the spectra from HOPG along a radial direction of its circular Brillouin zone. The normal incidence spectrum has a rising tail at  $\sim 1.5$  eV and a small broad feature at  $\sim 10.2$  eV. There is no significant change in the spectral appearance up to an angle of  $\sim 15^\circ$  away from normal incidence. At  $\theta = 20^\circ$  a broad peak at  $\sim 8.5$  eV appears and becomes relatively narrow as well as dispersive in nature towards lower binding energy at higher polar angles. It disperses up to 2.5 eV above  $E_F$ . Due to grazing incidence of the electrons on the sample, this peak is suppressed at higher polar angles. In fig. 4.8(b) the bands obtained experimentally have been superimposed on a theoretical [30] unoccupied band structure of graphite along  $\Gamma M$  direction. It is noted from the figure that the dispersing peaks in fig. 4.8(a) are mainly coming from the lower  $\pi^*$  band of graphite while the last two points are nearer to the upper  $\pi^*$  band. Dispersing nature of this band is in agreement with previous experimental results on HOPG [22, 23, 25]. Apart from this feature, there is a non-dispersive peak at  $\sim 1.5$  eV above  $E_F$  over the entire radial direction. Earlier studies on HOPG have reported this non-dispersive peak appearing within an energy interval of  $\sim 1.5$  eV to 2.5 eV. A non-dispersive

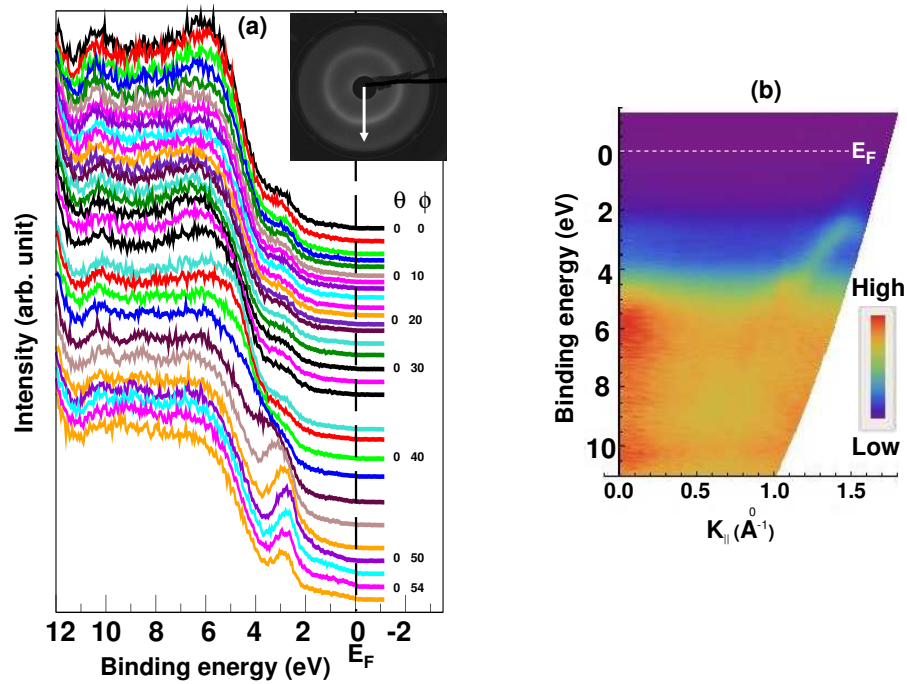


**Figure 4.6:** (a) The angle resolved photoemission spectra of HOPG along a radial direction of the circular Brillouin zone (along the arrow shown in inset); the low energy electron diffraction pattern of HOPG was taken at room temperature with a beam energy of 165 eV. The circular pattern, instead of six distinct spots as in single crystal graphite, shows its quasi crystalline structure. Since different symmetry directions of the Brillouin zone get averaged out, all the radial directions become equivalent. (b) The intensity plot of the photoemission spectra shown in (a).

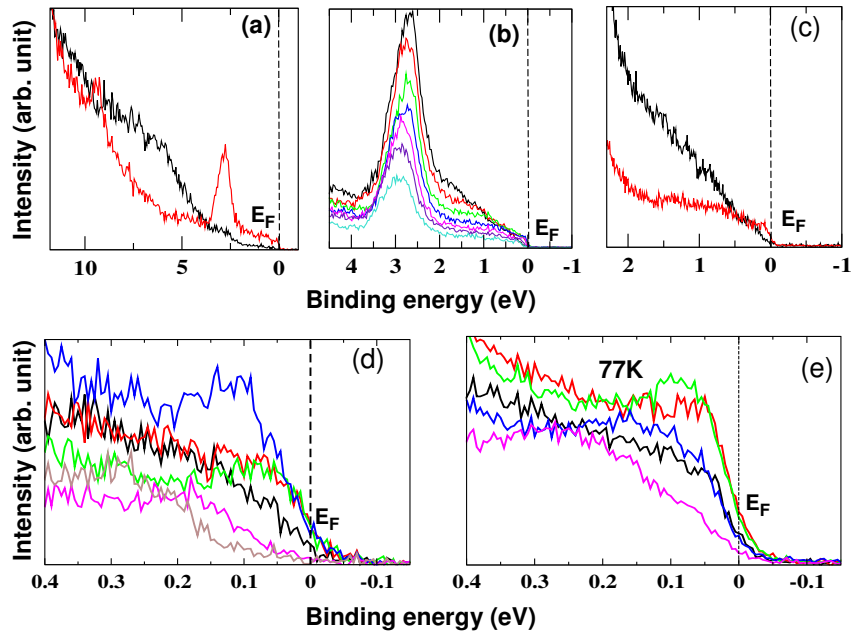


**Figure 4.7:** Spectra of HOPG along the same direction as in fig. 4.6 over different energy ranges: (a) shows the spectra at the  $\Gamma$  point (black curve) and at the zone boundary (red curve) over an energy range of  $\sim 11$  eV, (b) shows a set of spectra at and around the zone boundary over an energy range of  $\sim 5$  eV, in (c) the spectra at  $K$  point (red curve) and slightly away from the  $K$  point (black curve) of the Brillouin zone over the energy range of  $\sim 3$  eV are compared. The  $K$  point spectra shows the appearance of a small peak very close to the Fermi energy. The dispersion of this peak for some nearby angles is shown in (d) where the spectra are taken over an energy range of 0.5 eV, the same taken at a temperature of 77 K is shown in (e).

peak at similar energy position is also visible in the spectra (Fig. 4.8(c)) from single crystal graphite. Like the non-dispersive feature in ARPES spectra seen at  $\sim 2.8$  eV, this feature could as well be related to indirect transitions into the high density of states of the  $\pi^*$  band at the  $M$  point, probably aided by phonon or defect scattering [20–23]. Alternatively, these states could be attributed to extrinsic surface states or emission from isolated carbon atoms sitting on top of the outermost atomic plane [24]. Another clearly visible feature in the spectra of single crystal graphite is the peak appearing at a polar angle of  $\sim 20^\circ$  and dispersing towards the lower binding energy at higher polar angles. This is identified as the lower  $\pi^*$  band of graphite by comparing the experimentally obtained  $E$  vs  $k_{\parallel}$  result with the calculated band along  $\Gamma M$  direction (fig. 4.8(d)). Though we have taken angle resolved data along a direction which is  $\sim 17^\circ$  off from the  $\Gamma M$  symmetry direction, we notice from the  $E$  vs  $k_{\parallel}$  plot in fig. 4.8(d) that the dispersion is comparable with the  $\pi^*$  band in  $\Gamma M$  direction [20] which is quite unexpected for single crystal graphite.

## 4.4 Summary and Conclusions

Using ARPES, we have studied the valence band structure of natural single crystal graphite along the symmetry directions  $\Gamma K$  and  $\Gamma M$ . We observe that the agreement of ARPES results near the zone boundary is good with our calculated  $\pi$  bands having effect of coupling up to third nearest neighbours and near the zone centre the experimental features superpose better with the calculated band structure having first nearest neighbour coupling only. In HOPG the valence band dispersions were taken along different radial directions of its Brillouin zone and we found no azimuthal dependence of the spectra. We estimate a splitting of  $\sim 0.5$  eV between the two valence  $\pi$  bands of single crystal graphite from its near Fermi energy spectra. This splitting is due to the coupling between two layers of graphite. We also notice the appearance of a sharp peak below  $E_F$  at the  $K$  point at low temperature which comes up due to coupling of electrons with phonon, indicating a strong electron-phonon coupling. In HOPG we see only a single  $\pi$  band feature near the Fermi energy at its zone boundary. The inherent in-plane randomness of HOPG could be the reason for its two  $\pi$  bands to be unresolved. We have used KRIPES to study the conduction band structure of HOPG along a radial direction of its circular Brillouin zone and that of a single crystal graphite along a direction, slightly away from the  $\Gamma M$  symmetry direction. We see that for both the systems, the results superimpose on the theoretical conduction band structure of graphite along  $\Gamma M$  direction.

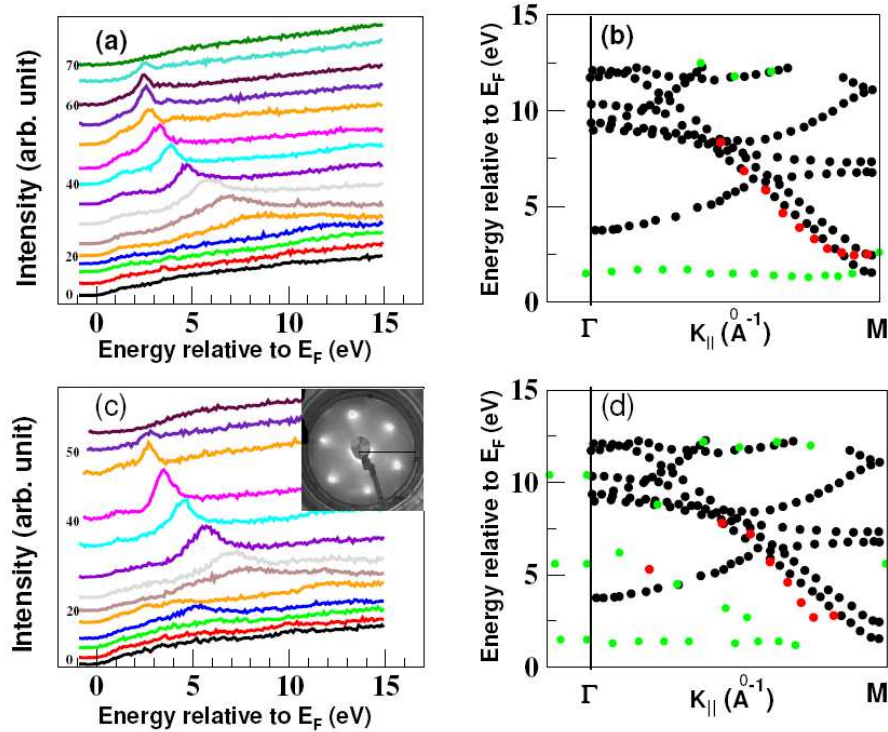


**Figure 4.8:** (a) The  $k$ -resolved inverse photoemission spectra of HOPG along a radial direction; (c) the same taken on single crystal graphite along the direction shown in inset. It is  $\sim 17^\circ$  away from the  $\Gamma - M$  direction of the Brillouin zone of graphite. The spectra were taken at an interval of  $5^\circ$ . For clarity, polar angle of incident electrons referred to the surface normal for some of the spectra are marked beside. All the strong (red circles) and weak (green circles) peaks of the experimental results in (a) and (c) have been plotted in (b) and (d) respectively along with the theoretical (black circles) unoccupied bands of graphite calculated by Holzwarth et al [30] in the  $\Gamma - M$  direction of the Brillouin zone.

# Bibliography

- [1] S. Y. Zhou, G. -H. Gweon, J. Graf, A. V. Fedorov, C. D. Spataru, R. D. Diehl, Y. Kopelevich, D. -H. Lee, S. G. Louie and A. Lanzara, *Nature Physics* **2**, 595 (2006)
- [2] Y. Kopelevich, P. Esquinazi, J. H. S. Torres and S. Moehlecke, *Journal of Low Temperature Physics* **119**, 691 (2000)
- [3] P. Esquinazi, A. Setzer, R. Höhne, C. Semmelhack, Y. Kopelevich, D. Spemann, T. Butz, B. Kohlstrunk and M. Lösche, *Physical Review B* **66**, 024429 (2002)
- [4] P. Esquinazi, D. Spemann, R. Höhne, A. Setzer, K. -H. Han and T. Butz, *Physical Review Letters* **91**, 227201 (2003)
- [5] H. Kempa, H. C. Semmelhack, P. Esquinazi, Y. Kopelevich, *Solid State Communications* **125**, 1-5 (2003)
- [6] W. Eberhardt, I. T. McGovern, E. W. Plummer and J. E. Fischer, *Physical Review Letter* **44**, 200 (1980)
- [7] A. R. Law, J. J. Barry and H. P. Hughes, *Physical Review B* **28**, 5332 (1983)
- [8] D. Marchand, C. Frétygny, M. Laguës, F. Batallan, Ch. Simon, I. Rosenman and R. Pinchaux, *Physical Review B* **30**, 4788 (1984)
- [9] T. Takahashi, H. Tokailin and T. Sagawa, *Physical Review B* **32**, 8317 (1985)
- [10] A. R. Law, M. T. Johnson and H. P. Hughes, *Physical Review B* **34**, 4289 (1986)
- [11] T. Kihlgren, T. Balasubramanian, L. Walldén and R. Yakimova, *Physical Review B* **66**, 235422 (2002)
- [12] K. Sugawara, T. Sato, S. Souma, T. Takahashi and H. Suematsu, *Physical Review B* **73**, 045124 (2006)
- [13] K. Sugawara, T. Sato, S. Souma, T. Takahashi and H. Suematsu, *Physical Review Letter* **98**, 036801 (2007)
- [14] C. S. Leem, B. J. Kim, Chul Kim, S. R. Park, T. Ohta, A. Bostwick, E. Rotenberg, H. -D. Kim, M. K. Kim, H. J. Choi and C. Kim, *Physical Review Letter* **100**, 016802 (2008)

- [15] A. Grüneis, C. Attaccalite, T. Pichler, V. Zabolotnyy, H. Shiozawa, S. L. Molodtsov, D. Inosov, A. Koitzsch, M. Knupfer, J. Schiessling, R. Follath, R. Weber, P. Rudolf, L. Wirtz and A. Rubio, *Physical Review Letter* **100**, 037601 (2008)
- [16] S. Y. Zhou, G. H. Gweon, C.D. Spataru, J. Graf, D. -H. Lee, Steven G. Louie and A. Lanzara, *Physical Review B* **71**, 161403(R) (2005)
- [17] H. Negishi, S. Negishi, K. Shimada, T. Narimura, M. Higashiguchi, H. Namatame, M. Taniguchi, K. Kobayashi, K. Sugihara and H. Oshima, *Journal of Physics and Chemistry of Solids* **67**, 1145-1148 (2006)
- [18] V. Pantin, J. Avila, M. A. Valbuena, P. Esquinazi, M. E. Dávila and M. C. Asensio, *Journal of Physics and Chemistry of Solids* **67**, 546-551 (2006)
- [19] M. E. Dávila, M. A. Valbuena, V. Pantín, J. Avila, P. Esquinazi and M. C. Asensio, *Applied Surface Science* **254**, 55-61 (2007)
- [20] R. Claessen, H. Carstensen and M. Skibowski, *Physical Review B* **38**, 12582 (1988)
- [21] I. Forbeaux, J. -M. Themlin and J. -M. Debever, *Physical Review B* **58**, 16396 (1998)
- [22] I. Schäfer, M. Schlüter and M. Skibowski, *Physical Review B* **35**, 7663 (1987)
- [23] H. Ohsawa, T. Takahashi, T. Kinoshita, Y. Enta, H. Ishii and T. Sagawa, *Solid State Communications* **61**, 347-350 (1987)
- [24] B.Reihl, J. K. Gilnzewski, J. M. Nicholls and E. Tosatti, *Physical Review B* **33**, 5770 (1986)
- [25] F. Maeda, T. Takahashi, H. Ohsawa, S. Suzuki and H. Suematsu, *Physical Review B* **37**, 4482 (1988)
- [26] A. K. Shukla, S. Banik and S. R. Barman, *Current Science* 90, 490 (2006); S. Banik, A. K. Shukla and S. R. Barman, *Rev. Sci. Instrum.* **76**, 066102 (2005)
- [27] M. K. Dalai, P. Pal, R. Kundu, B. R. Sekhar, S. Banik, A. K. Shukla, S. R. Barman, C. Martin, *Physica B* **405**, 186-191 (2010); S. K. Pandey, A. Kumar, S. Banik, A. K. Shukla, S. R. Barman and A. V. Pimpale, *Physical Review B* **77**, 113104 (2008); R. S. Dhaka, S. Banik, A. K. Shukla, V. Vyas, Aparna Chakrabarti, S. R. Barman, B. L. Ahuja and B. K. Sharma, *Physical Review B* **78**, 073107 (2008)

- [28] J. -C. Charlier, X. Gonze and J. -P. Michenaud, Physical Review B **43**, 4579 (1991)
- [29] R. F. Willis, B. Fitton and G. S. Painter, Physical Review B **9**, 1926 (1974)
- [30] N. A. W. Holzwarth, S. G. Louie and S. Rabi, Physical Review B **26**, 5382 (1982)
- [31] R. C. Tatar and S. Rabi, Physical Review B **25**, 4126 (1982)
- [32] F. Guinea, A. H. Castro Neto, and N. M. R. Peres, Physical Review B **73**, 245426 (2006)
- [33] S. Reich, J. Maultzsch, C. Thomsen and P. Ordejón, Phys. Rev. B **66**, 035412 (2002)

# 5

## Electronic structure of $\text{Bi}_{1-x}\text{Pb}_x\text{FeO}_3$ from XPS and UPS

### 5.1 Introduction

Multiferroic materials simultaneously exhibit ferroelectric (FE), magnetic and/or ferroelasticity orders in the same phase and a coupling between them over certain ranges of temperature [1,2]. These type of materials could be electrically polarized using an external magnetic field or structural strains and alternately an external electric field could induce magnetization in them. Hence, due to co-existence of different ferroic orders multiferroic materials are technologically very important. They can provide opportunities for potential applications in magnetic and ferroelectric devices as well as devices whose action is based on magneto electric effects. For the construction of multifunctional devices like data storage, spintronics, microelectronic devices and sensors [3,4] etc. multiferroic materials have huge application possibility. Owing to their potential applications and the physical mechanism behind their co-existing magnetic, ferroelectric and/or ferroelasticity orders, multiferroic materials have attracted a lot of interest in the last several years. So far  $\text{BiFeO}_3$  is the most widely studied multiferroic material, majorly because of its both the electrical and magnetic ordering occur above room temperature. Its ferroelectric  $T_C$  is  $\sim(810-830^\circ\text{C})$  and antiferromagnetic  $T_N$  is  $\sim(350-370^\circ\text{C})$  [5]. Moreover, thin film  $\text{BiFeO}_3$  shows exceptionally large polarization current compared to the conventional ferroelectric materials.  $\text{BiFeO}_3$  has its ferroelectric (FE) and antiferromagnetic (AFM) orders originating from the  $6s^2$  lone pair electrons of the off-center located Bi ions and the partially filled d orbitals of the Fe ions respectively [3]. The large spontaneous FE polarization shown by this material

was initially thought to be due to the heteroepitaxial constraint on its crystal structure [2]. But, recent measurements on thin films and single crystals [6, 7] have shown that strain has only minor effects on this FE polarization and it arises from the structural modifications. These studies have further shown that the FE polarization is intrinsic to the  $\text{BiFeO}_3$  and depends strongly on the topology of the oxygen octahedra in its structure.

At room temperature the  $\text{BiFeO}_3$  has a distorted  $\text{ABO}_3$  perovskite structure with R3c symmetry where the  $\text{Bi}^{3+}$  and  $\text{Fe}^{3+}$  ions are displaced relative to the oxygen octahedra [8]. At  $T_C$  (810-830 °C), this material undergoes a first order structural phase transition from FE (R3c) to paraelectric (PE) ( $\text{P}2_{1/m}$ ) which is accompanied by a strong tilting of the octahedra along the b axis and antiferroelectric displacements of the Fe cations. Haumont et al. have shown that this tilting of the oxygen octahedra results in significant electronic re-arrangements of the chemical bondings, especially the Fe - O bond lengths and Fe - O - Fe bond angles [8]. Such a tilting with respect to the Bi and Fe cations can lead to changes in the Bi 6p - O 2p and Fe 3d - O 2p hybridization strengths and thereby changes in the average valence of Bi and Fe sites. Partial substitutions of Bi by other elements were also found to result in the tilting of the oxygen octahedra leading to enhanced or suppressed multiferroic properties [9, 10]. With similar electronic structure, especially the lone pair electrons, Pb substitution for Bi was expected to modify the magnetic and FE properties. Further, the difference in the charge and ionic radii of  $\text{Bi}^{3+}$  and  $\text{Pb}^{2+}$  can also lead to topological changes in the oxygen octahedra. Our recent study on Pb substitution reported a structural phase transition reducing the rhombohedral distortion and leading towards a cubic structure with progressive breaking of the ferroelectric order [11].

The changes in Fe 3d - O 2p - Bi 6p hybridization strengths across the structural phase transition should reflect on the valence band electronic structure, particularly on the near Fermi level ( $E_F$ ) density of states (DOS) which are crucial to the FE and magnetic properties of this material. In order to understand the role of the R3c to cubic structural transition and its associated changes in the oxygen octahedra in reducing the ferroelectric order we have studied the changes in the valence band electronic structure of  $\text{Bi}_{1-x}\text{Pb}_x\text{FeO}_3$  ( $x=0.02$  to 0.15) system across its phase transition. The structure of this solid solution, at room temperature, presents a first order phase transition from R3c to cubic. We have used ultraviolet photoelectron spectroscopy (UPS) and X-ray photoelectron spectroscopy (XPS) in order to probe the fine changes in the valence band electronic structure of the  $\text{Bi}_{1-x}\text{Pb}_x\text{FeO}_3$  ( $x = 0.02$  to 0.15) system.

## 5.2 Experimental

Polycrystalline samples of  $\text{Bi}_{1-x}\text{Pb}_x\text{FeO}_3$  with  $x = (0.02 \text{ to } 0.15)$  were prepared by conventional solid state reactions by using high purity bismuth oxide, lead oxide and iron oxide as starting compounds. The compositional homogeneity of the samples were confirmed by a careful investigation using X-ray diffraction (XRD, Philips X-celerator Bragg-Brentano diffractometer) and scanning electron microscopy (SEM FEG, LEO 1530). XRD and SEM have confirmed a pure perovskite phase free from any impurities or intergranular second phases. The details of the sample preparation and characterization measurements were published elsewhere [11]. Our XRD measurements have shown that the composition with  $x = 0.02$  has a R3c crystal structure which is like pure  $\text{BiFeO}_3$ . As the Pb content increases from  $x = 0.05$  the samples showed the presence of nano regions with a Pm-3m structure. The size of these nano regions increased systematically with the Pb content and finally the  $x = 0.15$  has a long range cubic Pm-3m structure.

The photoemission measurements were performed by using an Omicron mu-metal ultra high vacuum system equipped with an Al  $\text{K}_\alpha$  X-ray source, a high intensity vacuum ultraviolet (VUV) source (HIS 13) and a hemispherical (mean radius of 125 mm) electron energy analyzer (EA125HR). The overall resolution for the XPS measurements was  $\sim 1$  eV. At the He I (21.2 eV) line, the photon flux from the VUV source was of the order of  $10^{16}$  photons/sec/steradian with a beam spot of 2.5 mm diameter. The Fermi energies ( $E_F$ ) for all measurements were calibrated by using the  $E_F$  of a freshly evaporated Ag film on a sample holder. The total energy resolution of the UPS measurements, estimated from the width of the Ag Fermi edge, was about 80 meV. Freshly cleaned surfaces of the samples were obtained by repeatedly scraping the sample surfaces by using a diamond file inside the chamber under a base vacuum of  $\sim 1.0 \times 10^{-10}$  mbar. The XPS and UPS measurements were performed under a base vacuum of  $\sim 1.0 \times 10^{-10}$  mbar. The negligible intensity found for the  $\sim 9.5$  eV bump (commonly regarded as a signature of un-clean surfaces) in the UPS spectra ensures the cleanliness of our sample surfaces. For the temperature dependent measurements, the samples were cooled by pumping liquid nitrogen through the sample manipulator fitted with a cryostat. The sample temperatures were measured by using a silicon diode sensor touching the bottom of the stainless steel sample holder.

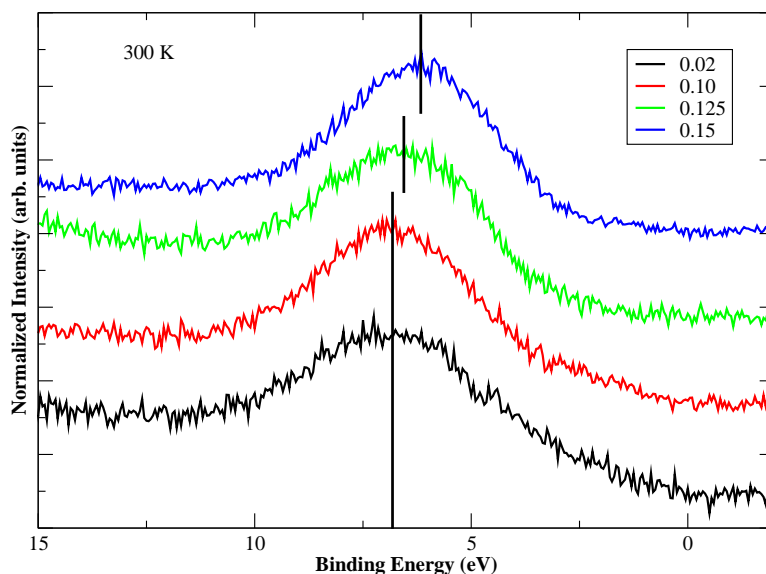


**Figure 5.1:** Valence Band Spectra of the  $\text{Bi}_{1-x}\text{Pb}_x\text{FeO}_3$  ( $x = 0.02$  to  $0.15$ ) samples taken at room temperature by using  $\text{Al K}_{\alpha}$  X-rays. The spectra corresponding to the  $x = 0.125$  and  $0.15$  shift towards lower binding energy, possibly due to increase in metallicity.

### 5.3 Results and Discussions

Figure 5.1 shows the valence band spectra of the  $\text{Bi}_{1-x}\text{Pb}_x\text{FeO}_3$  ( $x = 0.02$  to  $0.15$ ) samples taken at room temperature by using XPS. The spectra are normalized for their intensities and shifted along the ordinate axis for clarity of display. The main feature appearing at  $\sim 6$  eV could be due to the hybridized Fe 3d, O 2p and Bi 6p states. Although, band structure calculations based on local spin density approximations and strong correlation effect (LSDA + U, U being Hubbard parameter) agree qualitatively with this assignment, they have shown the Fe 3d derived states to dominate around the Fermi energy [6, 12]. The spectra corresponding to the  $x = 0.125$  and  $0.15$  show a shift to the lower binding energy compared to the other compositions. This shift in the valence band spectra is reflected in all the other core-level spectra of different compositions. In figure 5.2 we show the O 1s level photoemission spectra of the different samples. Here also the spectra are normalized in intensities and shifted along the ordinate axis for clarity. The O 1s spectra corresponding to the  $x = 0.125$  and  $0.15$  show a shift to the lower binding energy, even though the spectra are broad in shape. Since, this shift is observed in all the core level positions of both these compositions, it could well be ascribed to the increasing metallicity with increase in the

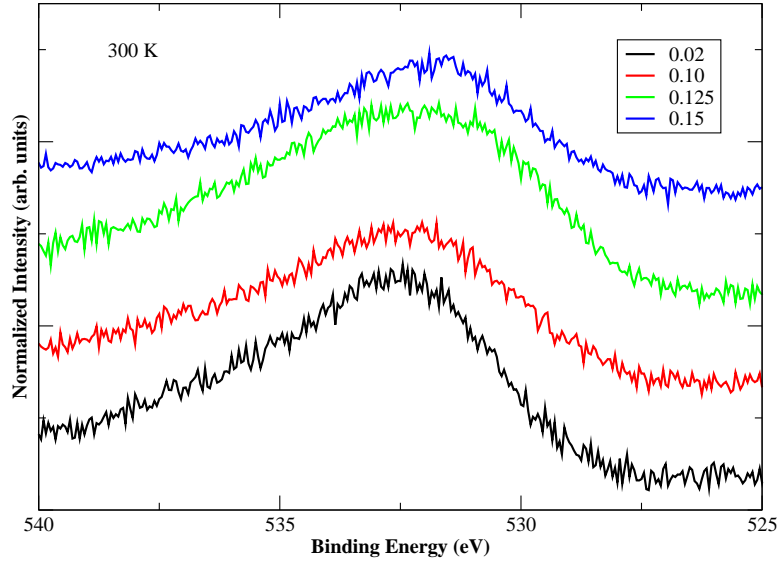


**Figure 5.2:** O 1s XPS spectra of the  $\text{Bi}_{1-x}\text{Pb}_x\text{FeO}_3$  ( $x = 0.02$  to  $0.15$ ) samples taken by using Al  $K_{\alpha}$  X-rays at room temperature. The spectra corresponding to the  $x = 0.125$  and  $0.15$  shift towards lower binding energy.

doping concentration.

The valence band spectra taken by using ultra-violet light are shown in Fig. 5.3. The main feature is similar to the one in the XPS valence band spectra. In this spectra (Fig. 5.3) also the  $x = 0.125$  and  $0.15$  compositions show a shift towards the Fermi level. Both the XPS and UPS valence band spectra look similar to the spectra obtained from the Fe 2p fluorescence by resonant X-ray emission spectroscopy [12, 13]. Although, the energy positions are similar in the XPS and the UPS spectra, an additional  $\sim 3$  eV feature appears in the UPS spectra. This feature with its long tail towards the  $E_F$  could be important to the electrical and magnetic properties of the  $\text{Bi}_{0.85}\text{Pb}_{0.15}\text{FeO}_3$  composition. The absence of this feature in the XPS spectra shows that it has predominant O 2p character, as the cross section of O 2p states at the ultra-violet energy range is larger compared to the X-ray.

It is mentioned earlier that the LSDA + U band structure calculations of Neaton et al. on  $\text{BiFeO}_3$  with R3c crystal structure have shown the states closest to the  $E_F$  have Fe 3d character [6]. within LSDA calculation they have found a small gap of  $\sim 0.4$  eV. With the inclusion of strong correlation term (U), the gap value increases which goes closer to our experimental findings. Though, in their calculations they used different values for the Coulomb term, only those results with  $U_{eff} = 4$  eV ( $U_{eff} = U - J$ , J being Hund's

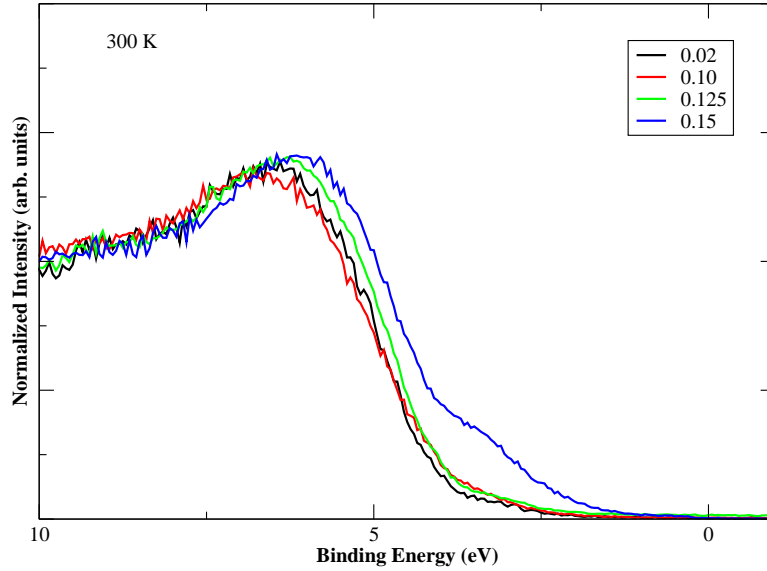


**Figure 5.3:** Valence Band spectra of the  $\text{Bi}_{1-x}\text{Pb}_x\text{FeO}_3$  ( $x = 0.02$  to  $0.15$ ) samples taken by using He I photons at room temperature. The cubic composition  $x = 0.15$  shows the presence of an additional feature at  $\sim 3$  eV below the  $E_F$ .

coupling) or higher look reasonably similar to our experimental results. According to these calculations the R3c structure is insulating with a band gap of 1.9 eV for  $U_{eff} = 4$  eV. The  $x = 0.02$  composition in our study has the same R3c crystal structure. The spectra corresponding to this composition presented in both Fig. 5.1 and 5.3 show that the value of the gap must be much larger ( $> 2.5$  eV). This indicates that the coulomb interaction has a significant role in this systems. Coupled to this large gap, the width of the valence band is also smaller compared to the calculated spectra. In our spectra, the emission from the Fe 3d states appears to be falling at a deeper energy position (higher binding energy). This would mean that the Fe 3d states are much strongly hybridized with the O 2p and Bi 6p states and the Coulomb term  $U_{eff}$  should effectively be larger than the value (4 eV) used in the LSDA + U calculations [6].

It is to be noted that the additional feature at  $\sim 3$  eV shown (Fig. 5.3) by the  $x = 0.15$  composition has emerged due to the transition of its crystal structure to cubic. As stated earlier, a comparison of the XPS and UPS valence band spectra shows that the  $\sim 3$  eV feature has mainly O 2p character. In Fig. 5.4 we show the UPS valence band spectra taken at 77 K which show that the behavior of the valence band features do not have any major temperature dependence. The spectra of the  $\text{Bi}_{0.85}\text{Pb}_{0.15}\text{FeO}_3$  sample taken

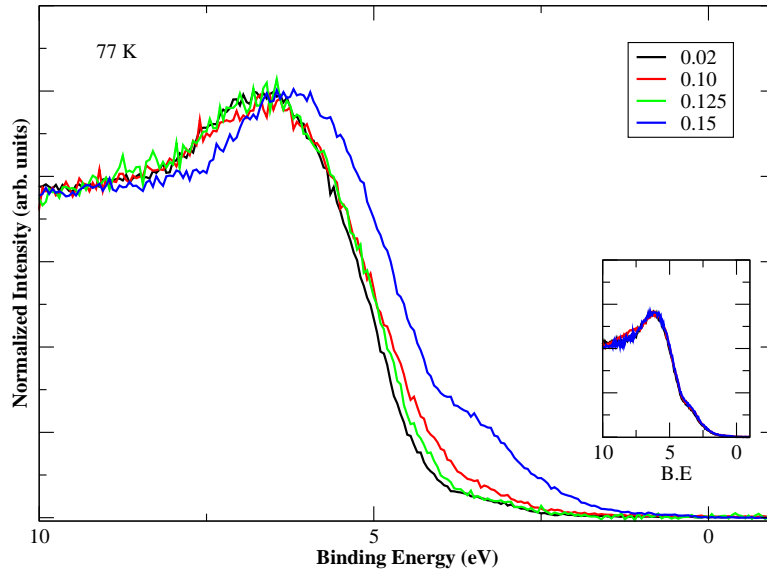


**Figure 5.4:** Valence Band spectra of the  $\text{Bi}_{1-x}\text{Pb}_x\text{FeO}_3$  ( $x = 0.02$  to  $0.15$ ) samples taken at  $77\text{ K}$  by using He I photons. Inset: Comparison of the spectra of  $x = 0.15$  sample taken at  $300\text{ K}$ ,  $150\text{ K}$  and  $77\text{ K}$ .

at different temperatures also do not show any change with temperature (inset of Fig. 5.4). Nevertheless, the  $\sim 3\text{ eV}$  feature with its long tail towards the  $E_F$  shows that the  $x = 0.15$  composition is more metallic in nature compared to the others. Neaton et al. have also performed band structure calculation on the possible cubic phase of  $\text{BiFeO}_3$ . Within LSDA scheme it shows metallicity and within LSDA+U a gap of  $\sim 0.5\text{ eV}$  opens up with  $U_{eff} = 2\text{ eV}$  whereas this gap is  $1.3\text{ eV}$  for the same value of  $U_{eff}$  with R3c structure. Our  $\text{Bi}_{1-x}\text{Pb}_x\text{FeO}_3$  sample with  $x = 0.15$  composition also posses a cubic structure and the spectroscopic results show it is less insulating compared to other compositions indicative of a smaller value of  $U$  with respect to pure  $\text{BiFeO}_3$ . Though the LSDA + U band structure calculations for the cubic structure also show a nearly metallic nature [6], it is not well accounted for. The R3c to cubic phase transition with Pb doping in  $\text{BiFeO}_3$  should be leading to a straightening up of the Fe-O-Fe bond angle to  $180$  degree from the buckled  $165$  degree. This would mean less distortion / tilting of the oxygen octahedra with respect to the Bi as well as Fe. Consequently, the Fe  $3d - \text{O } 2p$ , Bi  $6p - \text{O } 2p$  hybridization strengths might weaken resulting in the shift of O  $2p$  states more close to the  $E_F$ . Structural studies [11] performed on various compositions of the  $\text{Bi}_{1-x}\text{Pb}_x\text{FeO}_3$  have also arrived at similar conclusions. Addition of Pb reduces the rhombohedral distortion and progressively

breaks the ferroelectric ordering where the structure becomes cubic [11].

## 5.4 Summary and Conclusions

We have studied the valence band electronic structure of the  $\text{Bi}_{1-x}\text{Pb}_x\text{FeO}_3$  ( $x = 0.02$  to  $0.15$ ) system by using X-ray and ultra-violet photoelectron spectroscopy. As this system undergoes a R3c to cubic phase transition with Pb doping, the near Fermi level states show an enhanced oxygen 2p character due to the weakening of the Fe 3d - O 2p - Bi 6p hybridization strength. The valence bands of compositions with the R3c structure were found to be qualitatively similar to the LSDA calculations except for their estimates of the band width and band gap. Reasons for this could be the higher value of the effective Coulomb interaction. These results could be of importance to the understanding of the electron-electron correlation in multiferroic materials.

# Bibliography

- [1] S. R. Shannigrahi, A. Huang, N. Chandrasekhar, D. Tripathy and A. O. Adeyeye, *Appl. Phys. Lett.* **90**, 022901 (2007)
- [2] J. Wang, J. B. Neaton, H. Zheng, V. Nagarajan, S. B. Ogale, B. Liu, D. Viehland, V. Vaithyanathan, D. G. Schlom, U. V. Waghmare, N. A. Spaldin, K. M. Rabe, M. Wuttig and R. Ramesh, *Science* **299**, 1719 (2003).
- [3] S. -W Cheong and M. Mostovoy, *Nature Mater.* **6**, 13 (2007).
- [4] R. Ramesh and N. A. Spaldin, *Nature Mater.* **6**, 21 (2007).
- [5] Donna C. Arnold, Kevin S. Knight, Finlay D. Morrison and Philip Lightfoot, *Phys. Rev. Lett.* **102**, 027602 (2009)
- [6] J. B. Neaton, C. Ederer, U. V. Waghmare, N. A. Spaldin and K. M. Rabe, *Phys. Rev. B* **71**, 014113 (2005).
- [7] V. V. Shvartsman, W. Kleemann, R. Haumont and J. Kreisel, *Appl. Phys. Lett.* **90**, 172115 (2007).
- [8] R. Haumont, Igor A. Kornev, S. Lisenkov, L. Bellaiche, J. Kreisel and B. Dkhil, *Phys. Rev. B* **78**, 134108 (2008).
- [9] V. A. Khomchenko, D. A. Kiselev, M. Kopcewicz, M. Maglione, V. V. Shvartsman, P. Borisov, W. Kleemann, A. M. L. Lopes, Y. G. Pogorelov, J. P. Araujo, R. M. Rubinger, N. A. Sobolev, J. M. Vieira, and A. L. Kholkin, to be published.
- [10] G. L. Yuan and S. W. Or, *J. Appl. Phys.* **100**, 024109 (2006).
- [11] J. Chaigneau, R. Haumont and J. M. Kiat, *Phys. Rev. B* **80**, 184107 (2009).
- [12] J. A. McLeod, Z. V. Pchelkina, L. D. Finkelstein, E. Z. Kurmaev, R. G. Wilks, A. Moewes, I. V. Solovyev, A. A. Belik, and E. Takayama-Muromachi, *Phys. Rev. B* **81**, 144103 (2010).
- [13] T. Higuchi, Yi-Sheng Liu, Pen Yao, Per-Anders Glans, J. Guo, C. Chang, Z. Wu, W. Sakamoto, N. Itoh, T. Shimura, T. Yogo and T. Hattori, *Phys. Rev. B* **78**, 085106 (2008).

# 6

## Electronic Structure of $\text{Sm}_{0.1}\text{Ca}_{0.9-x}\text{Sr}_x\text{MnO}_3$ from UPS and ResPES Studies

### 6.1 Introduction

Perovskite manganites show a fascinating competition between various magnetic ground states originating from the spin and orbital degrees of freedom of charge carriers. For example, the magnetic and electrical properties of the  $\text{Ln}_{1-x}\text{Ca}_x\text{MnO}_3$  show dissimilar behaviours in their electron-doped ( $x > 0.5$ ) and hole-doped ( $x < 0.5$ ) versions [1, 2]. Maignan et al. have shown that the electron-doped manganites exhibit a semimetallic behaviour in their normal state for low  $x$  values while the hole-doped compositions show an insulating nature for similar doping [1]. Further, the cluster glass-like ferromagnetic behaviour shown by the electron doped compositions is markedly different from the ferromagnetism in hole-doped compounds [2]. Neutron diffraction studies have shown that these compositions show a phase separation comprising of ferromagnetic (FM) clusters embedded in a G-type antiferromagnetic (AFM) insulating matrix [2]. Such phase separated systems are at the focus of many theoretical models explaining the physical properties of CMR systems [3, 4].

$\text{Sm}_x\text{Ca}_{1-x}\text{MnO}_3$  is a typical example of the electron doped manganite systems. For  $x$  ranging from 0 to 0.12 this compound shows a semimetallic behaviour in the range 300-175 K, which could be explained considering the weak Jahn-Teller effect and consequently weak electron-phonon coupling [1]. Electrons in the sparingly occupied narrow  $e_g$  band

are delocalized leading to the semimetallic behavior. Interestingly, the  $\text{Sm}_x\text{Ca}_{1-x}\text{MnO}_3$  system exhibits ferromagnetism only in a narrow range of doping or  $\text{Mn}^{3+}$  concentration. In this range this compound shows coexisting ferromagnetic and G-type AFM phases for doping levels of about 5 percent of  $\text{Mn}^{3+}$ . Further, the nature of phase separation and amount of ferromagnetic component in this compound is controlled by the size of the A-site cation. The ferromagnetic (FM) and antiferromagnetic (AFM) interactions present are governed by the one electron band width of the  $e_g$  band which in turn is controlled by the Mn-O-Mn bond angles and Mn-O bond lengths. It has been shown that the FM component is the largest in the  $\text{Sm}_{0.1}\text{Ca}_{0.9}\text{MnO}_3$  sample with a manganese oxidation state of +3.9 [5].

In order to see the consequence of the A-site cationic change and ferromagnetism on the near Fermi level electronic structure, in this study we have used samples of the  $\text{Sm}_{0.1}\text{Ca}_{0.9-x}\text{Sr}_x\text{MnO}_3$  system doped with Sr in place of Ca. As can be noticed from the Mn valence, the  $e_g$  electron concentration in these samples remain the same irrespective of the doping. As mentioned earlier, the A-site cation controls the nature of the phase separation in this system. We have used photoelectron spectroscopy and resonant photoelectron spectroscopy for our studies.

## 6.2 Experimental

The polycrystalline samples of  $\text{Sm}_{0.1}\text{Ca}_{0.9-x}\text{Sr}_x\text{MnO}_3$  were prepared by conventional solid state reactions by mixing  $\text{MnO}_2$ ,  $\text{CaO}$ ,  $\text{SrCO}_3$  and  $\text{Sm}_2\text{O}_3$  in stoichiometric proportions. The powders were first heated at 1000 °C for 12 hrs with intermediate grindings and then pressed in the form of pellets. They were then sintered at 1200 and 1500 °C for 12 h in air with a slow cooling down to 800 °C and finally quenched to room temperature. Details of the sample preparation technique could be found elsewhere [6]. The monophasic, homogeneous nature of the samples have been checked by using x-ray powder and electron diffraction techniques. The cationic compositions, close to their nominal values were confirmed by using energy dispersive spectroscopy and iodometric titrations. Magnetic and electrical transport properties of the samples were determined by using a vibrating sample magnetometer (SQUID-VSM, Quantum Design) and four probe resistivity measurements (PPMS, Quantum Design). Consolidated results of these studies are published elsewhere [6].

Angle integrated ultraviolet photoemission measurements were performed by using an Omicron mu-metal ultra high vacuum system equipped with a high intensity vacuum-ultraviolet source (HIS 13) and a hemispherical electron energy analyzer (EA 125 HR). At

the He  $I$  ( $h\nu = 21.2$  eV) line, the photon flux was of the order of  $10^{16}$  photons/sec/steradian with a beam spot of 2.5 mm diameter. Fermi energies for all measurements were calibrated using a freshly evaporated Ag film on a sample holder. The total energy resolution, estimated from the width of the Fermi edge, was about 80 meV for He  $I$  excitation. All the photoemission measurements were performed inside the analysis chamber under a base vacuum of  $\sim 7.0 \times 10^{-11}$  mbar. The polycrystalline samples were repeatedly scraped using a diamond file inside the preparation chamber with a base vacuum of  $\sim 2.0 \times 10^{-10}$  mbar and the spectra were taken within 1 hour, so as to avoid any surface degradation. All measurements were repeated many times to ensure the reproducibility of the spectra. For the temperature dependent measurements, the samples were cooled by pumping liquid nitrogen through the sample manipulator fitted with a cryostat. Sample temperatures were measured using a silicon diode sensor touching the bottom of the stainless steel sample plate. The low temperature photoemission measurements at 77 K were performed immediately after cleaning the sample surfaces followed by the room temperature measurements. Resonant photoemission measurements were performed across the  $\text{MnL}_{2-3}$  absorption edge under UHV conditions. Soft X rays from the BACH beamline associated with the ELETTRA synchrotron light source at Trieste had been used for these measurements. The total energy resolutions were set at 381 meV for Mn 2p-3d ResPES measurements. The fermi level of the samples were referred to that of a freshly cleaned gold sample in good electrical contact with the sample holder. The measurements were carried out in the analysis chamber with a base vacuum of about  $1 \times 10^{-10}$  mbar. Before each measurement, the samples were cleaned by repeated scraping using a diamond file inside the preparation chamber with a base vacuum of about  $1 \times 10^{-9}$  mbar.

### 6.3 Results and Discussion

At room temperature  $\text{Sm}_{0.1}\text{Ca}_{0.9-x}\text{Sr}_x\text{MnO}_3$  ( $0 \leq x \leq 0.8$ ) has a  $Pnma$  structure ( $a_p\sqrt{2} \times 2a_p \times a_p\sqrt{2}$ ) for  $x \leq 0.4$  and for  $0.5 \leq x < 0.8$  the structure is  $I4/mcm$  ( $a_p\sqrt{2} \times a_p\sqrt{2} \times 2a_p$ ,  $a_p$  being the cell parameter for cubic perovskite). For  $x \geq 0.8$  the structure is a mixture of hexagonal and cubic phases. Further, in the  $Pnma$  domain there are two types of lattices, i.e., ( $a > b/\sqrt{2} > c$ ) for  $x < 0.2$  and ( $c > b/\sqrt{2} > a$ ) for  $x > 0.2$ . All the three lattice parameters increase with increasing Sr content. The phase diagram of the  $\text{Sm}_{0.1}\text{Ca}_{0.9-x}\text{Sr}_x\text{MnO}_3$  system built from the magnetic and transport measurements and published earlier [6] is shown in Fig.6.1. The magnetic ground state of the parent com-

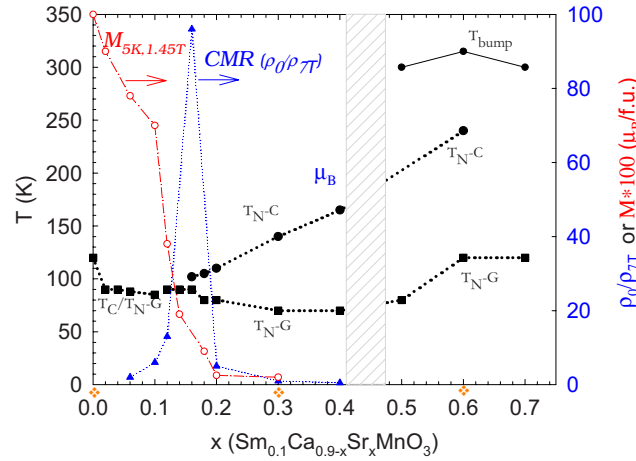
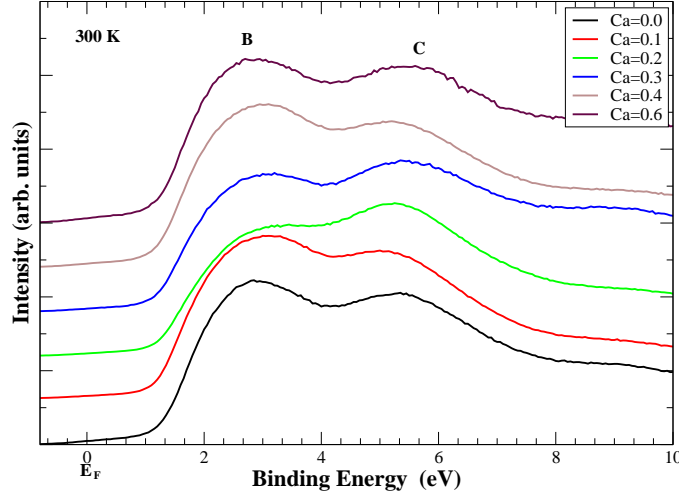


**Figure 6.1:** Phase diagram of  $\text{Sm}_{0.1}\text{Ca}_{0.9-x}\text{Sr}_x\text{MnO}_3$  samples determined from magnetic and transport measurement (taken from reference [6]).

pound ( $\text{Sm}_{0.1}\text{Ca}_{0.9}\text{MnO}_3$ ) at low temperatures (below  $T_N=T_C=110\text{K}$ ) comprises of ferromagnetic clusters (FM) embedded in a G-type AFM phase. Compositions with  $x < 0.2$  also show the presence of this FM component. This component is sensitive to the substitution of Sr for Ca. Compositions with  $0.18 \leq x \leq 0.6$  have  $T_C \neq T_N$  and they vary from 70K to 120K and 140K to 315K (for  $x=0.3$  to 0.6).

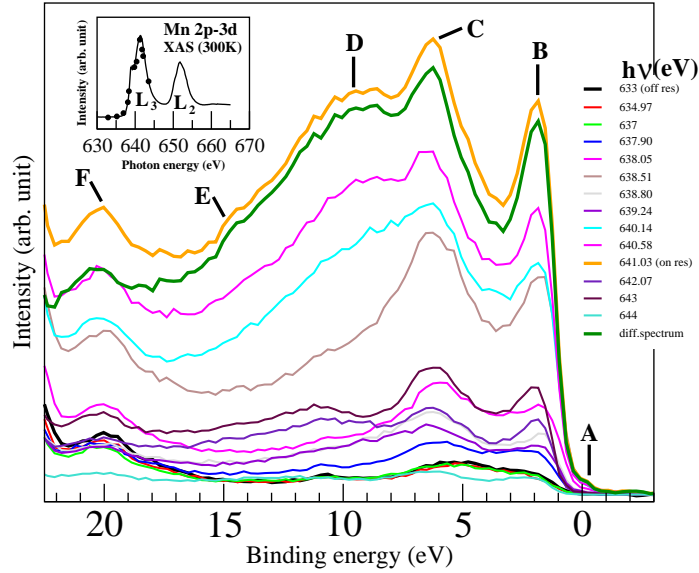
In Fig.6.2 we present the angle integrated valence band photoemission spectra from the different compositions of the  $\text{Sm}_{0.1}\text{Ca}_{0.9-x}\text{Sr}_x\text{MnO}_3$  system taken at room temperature by using He I photons. Intensities of all the spectra are normalized and shifted along the ordinate axis by a constant value for clarity of presentation. The features seen in the spectra are dominated by the states due to the Mn 3d-O 2p hybridized orbitals. The origin of the two prominent features, one at  $\sim 2.9$  eV (marked B) and another at  $\sim 5.3$  eV (marked C) below  $E_F$ , are by now well understood from earlier experiments and band structure calculations [7–11] on similar systems. The feature at  $\sim 2.9$  eV is mainly due to the  $t_{2g\uparrow}$  states of the  $\text{MnO}_6$  octahedra while the one at  $\sim 5.3$  eV has contributions from both Mn  $t_{2g}$  and O 2p states. The Mn 3d  $e_g$  states appear in the figure as a tail towards the  $E_F$ . Intensity of this feature is quite small compared to B and C, indicating the small  $e_g$  electron concentration in these samples.

Figure 6.3 shows the resonant photoemission spectra of the  $\text{Sm}_{0.1}\text{Ca}_{0.9-x}\text{Sr}_x\text{MnO}_3$  ( $x = 0$ ) sample taken at room temperature across the Mn  $2p \rightarrow 3d$  absorption edge. The photon energies at which these spectra were collected are marked in the inset showing



**Figure 6.2:** Angle integrated valence band photoemission spectra from the different compositions of the  $\text{Sm}_{0.1}\text{Ca}_{0.9-x}\text{Sr}_x\text{MnO}_3$  system taken at room temperature by using He I photons. Intensities of all the spectra are normalized and shifted along the ordinate axis by a constant value for clarity of presentation.

the  $MnL$  edge x-ray absorption spectrum (XAS). All the spectra shown in the figure are normalized by the incident photon flux. Different features of the spectra are marked A - E. As mentioned earlier the valence band consists mainly of Mn  $3d$  and O  $2p$  states. In Mn $2p$  -  $3d$  resonant photoemission, the photoemission process from Mn $3d$  level is strongly enhanced when the energy of the exciting photons equals the energy necessary to excite a Mn $2p$  electron to an unoccupied Mn $3d$  level. As we can see from the figure, the resonant enhancement of the Mn  $3d$  valence states have a maximum for  $h\nu = 641.03$  eV and a minimum for  $h\nu = 633.0$  eV, marked as the on- and off-resonant spectra. This resonance of the Mn  $3d$  photoemission is due to the process  $3d^n \rightarrow \underline{c}3d^{n+1} \rightarrow 3d^{n-1} + e^-$ , where  $\underline{c}$  denotes a Mn $2p$  hole. Interference between the normal photoemission process and the Mn $2p$  -  $3d$  transition followed by a  $2p$ - $3d$ - $3d$  Coster-Kronig decay generates this resonance in the valence band. The on-resonance spectra shows a sharp peak (marked B) positioned at  $\sim 2.5$  eV which could be ascribed to the Mn  $3d$   $t_{2g}$  states. The broad feature (C) appearing at  $\sim 6.5$  eV originates from the hybridized O  $2p$  and Mn  $3d$   $t_{2g}$  bonding states. Features D and E shift to higher binding energy with increasing photon energy and hence their origin could be assigned to Auger processes. Feature F at  $\sim 20$  eV is due to O  $2s$  [12–15]. The individual plots (not shown here) of the compositions  $x=0.2$ ,  $0.3$  and  $0.6$  show an extra small feature at  $\sim 18$  eV which could be assigned to Sr  $4p$  states [12, 13]. Appearance of a small spectral weight very close to  $E_F$  and the strong enhancement in intensity of the 1.9



**Figure 6.3:** Valence band resonant photoemission spectra of  $\text{Sm}_{0.1}\text{Ca}_{0.9-x}\text{Sr}_x\text{MnO}_3$  for  $x = 0.0$  composition. In the inset the  $MnL$  edge x-ray absorption spectrum (XAS) is shown. The photon energies used to probe the resonant valence band are marked by black circles in the XAS spectrum. Off- and on-resonance spectra are mentioned. Various peaks appearing in the on-resonance spectrum have been indicated by A, B, C, D, E and F respectively.

eV feature indicate that Mn 3d states give a significant contribution to the valence band of  $\text{Sm}_{0.1}\text{Ca}_{0.9}\text{MnO}_3$ . The sharp feature at 6 eV indicates the existence of strong Mn3d-O2p hybridization in the valence band regime. The very weak spectral weight (feature A) around Fermi energy in the resonant photoemission spectrum could be attributed to low density of  $e_g$  electrons in  $\text{Sm}_{0.1}\text{Ca}_{0.9-x}\text{Sr}_x\text{MnO}_3$ ; having only a small fraction of  $\text{Mn}^{3+}$  ( $t_{2g}^3 e_g^1$ ) ions.

In figure 6.4 we present the Mn 3d spectra from the  $\text{Sm}_{0.1}\text{Ca}_{0.9-x}\text{Sr}_x\text{MnO}_3$  samples. These spectra were obtained by subtracting the corresponding off-resonant spectra from the on-resonant spectra obtained from the different compositions. The difference spectrum is expected to resemble the Mn 3d partial density of states. As can be seen from the figure, there are significant spectral changes with increase in the Sr doping. The states coming from the Mn 3d  $e_g$  band do not show any shift in binding energy positions or a change in spectral intensity. This behaviour is consistent with its electrical transport measurements which showed that the room temperature resistivity values of various compositions ( $x$ ) have almost the same order of magnitude. For  $x=0.2$ , the Mn  $t_{2g}$  peak shows a shift towards the lower binding energy. This shift indicates a change in the Mn-O-Mn hybridization strength.

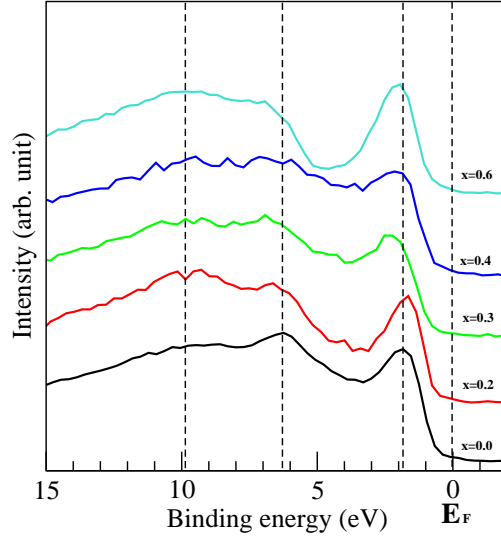


**Figure 6.4:** The difference spectra obtained from the on and off resonance spectra corresponding to the compositions  $x=0.2, 0.3, 0.4$  and  $0.6$  are shown. The spectra have been given constant shifts along y-axis for clarity of presentation.

As strontium content is raised, the A site cation size increases. Ionic radii of  $\text{Sr}^{2+}$  is 132 pm while  $\text{Ca}^{2+}$  is 114 pm. Increase in cation size could be leading to a decrease in the distortion of the  $\text{MnO}_6$  octahedra and straightening of Mn-O-Mn bond angle. This results in an increase in Mn 3d - O 2p hybridization. Hence Mn  $t_{2g}$  peak shifts towards Fermi energy. For higher doping like  $x= 0.3$  and  $0.4$ , the size mismatch could be detrimental to the Mn-O-Mn bond angle and the Mn 3d - O 2p hybridization [6]. Therefore despite the increase in Sr, the Mn-O-Mn bond angle decreases and this reduces the Mn 3d - O 2p hybridization. Dalai et al. [7] have reported in a recent paper that the electron-doped compound  $\text{Ca}_{0.86}\text{Pr}_{0.14}\text{MnO}_3$  shows a transfer of some of the electrons from the  $t_{2g}$  states to  $e_g$  states due to the reduced crystal field splitting in the FMM phase. The low temperature ground state of this compound also comprises of phase separated FMM and AFMI clusters. The observed shift in the  $t_{2g}$  states in our  $\text{Sm}_{0.1}\text{Ca}_{0.9-x}\text{Sr}_x\text{MnO}_3$  samples could also indicate a similar weakening of the crystal field splitting in compositions with  $x \leq 0.2$  following the structural changes in the  $\text{MnO}_6$  octahedra.

## 6.4 Conclusions

We have studied the valence electronic structure of the electron-doped CMR material  $\text{Sm}_{0.1}\text{Ca}_{0.9-x}\text{Sr}_x\text{MnO}_3$  for  $x=0.0, 0.2, 0.3, 0.4$  and  $0.6$  using ultra violet photoelectron spectroscopy (UPS) and resonance photoelectron spectroscopy (ResPES) with varying photon energy across the Mn 2p-3d absorption edge. The magnetic ground state of the parent compound ( $\text{Sm}_{0.1}\text{Ca}_{0.9}\text{MnO}_3$ ) at low temperatures consists of ferromagnetic clusters (FM) embedded in a G-type AFM phase. But this FM component is very sensitive to the substitution of Sr for Ca. The combined UPS and ResPES studies suggest that the valence band of this material has major contribution from Mn 3d states and there is a strong hybridization between Mn 3d  $t_{2g}$  and O 2p states. With strontium doping, the A site cation size increases and a significant change in the Mn 3d spectral weight is observed, indicating that there is a change in Mn 3d - O 2p hybridization strength due to structural modification caused by Sr doping.

# Bibliography

- [1] A. Maignan, C. Martin, F. Damay, B. Raveau and J. Hejtmanek, *Physical Review B* **58**, 2758 (1998).
- [2] C. Martin, A. Maignan, M. Hervieu and B. Raveau, *Physical Review B* **60**, 12191 (1999).
- [3] Adriana Moreo, Matthias Mayr, Adrian Feiguin, Seiji Yunoki, and Elbio Dagotto, *Phys. Rev. Lett.* **84**, 5568 (2000).
- [4] Adriana Moreo, Seiji Yunoki, Elbio Dagotto, *Science* **283**, 2034 (1999).
- [5] C. Martin, A. Maignan, M. Hervieu, B. Raveau, Z. Jiráč, M. M. Savosta, A. Kurbakov, V. Trounov, G. André, F. Bourée, *Physical Review B* **62**, 6442 (2000).
- [6] C. Martin, A. Maignan, M. Hervieu, S. Hébert, A. Kurbakov, G. André, F. Bourée-Vignerón, J. M. Broto, H. Rakoto, and B. Raquet, *Physical Review B* **77**, 054402 (2008).
- [7] M. K. Dalai, P. Pal, B. R. Sekhar, M. Merz, P. Nagel, S. Schuppler and C. Martin, *Physical Review B* **85**, 155128 (2012).
- [8] P. Pal, M. K. Dalai, R. Kundu, and B. R. Sekhar, *Physical Review B* **77**, 184405 (2008).
- [9] P. Pal, M. K. Dalai, B. R. Sekhar, I. Ulfat, M. Merz, P. Nagel, S. Schuppler, *Physica B* **406**, 3519-3523 (2011).
- [10] M. Chakraborty, P. Pal, and B. R. Sekhar, *Solid State Commun.* **145**, 197, (2008).
- [11] T. Saitoh, A. E. Bocquet, T. Mizokawa, H. Namatame, A. Fujimori, M. Abbate, Y. Takeda and M. Takano, *Physical Review B* **51**, 13942 (1995).
- [12] F. L. Battye, H. Höchst and A. Goldmann, *Solid State Communications* **19**, 269-271 (1976).
- [13] B. Reihl, J. G. Bednorz, K. A. Müller, Y. Jugnet, G. Landgren and J. F. Morar, *Physical Review B* **30**, 803 (1984).
- [14] P. Pertosa and F. M. Michel-Calendini, *Physical Review B* **17**, 2011 (1978).

- [15] M. Kowalik, R. Zalecki and A. Kolodziejczyk, *Acta Physica Polonica A* **117**, 277 (2010).

# 7

## Summary

In this thesis, the electronic structures of single crystal graphite and highly oriented pyrolytic graphite have been studied using ARPES, KRIPES and band structure calculations. The electronic structures of single layer graphene and bilayer graphene have also been investigated using tight binding calculations. Further, the occupied electronic structures of Pb doped multiferroic material,  $(\text{Bi}_{1-x}\text{Pb}_x\text{FeO}_3)$  and Sr doped  $\text{Sm}_{0.1}\text{Ca}_{0.9}\text{MnO}_3$  (a colossal magnetoresistive material) have been studied using UPS, XPS and ResPES techniques.

Using ARPES, we have studied the valence band structure of natural single crystal graphite along the symmetry directions  $\Gamma K$  and  $\Gamma M$  of its Brillouin zone. We find two clearly dispersing bands ( $\pi$  and  $\sigma$ ) in both the directions. We observe that the agreement of our results is good near the zone boundaries (the  $K$  and  $M$  points) with the calculated band structure for which interactions of electrons up to third nearest neighbours are considered and near the zone centre (the  $\Gamma$  point) the agreement is better with the calculated bands having first nearest neighbour interaction only. In HOPG the valence band dispersions were taken along different radial directions of its Brillouin zone and we found no azimuthal dependence of the spectra as expected. We estimated a splitting of  $\sim 0.5$  eV between the two valence  $\pi$  bands of single crystal graphite from its near Fermi energy spectra at the  $K$  point. This splitting is due to the weak interlayer coupling in graphite. We also observe the appearance of a sharp peak below  $E_F$  at the  $K$  point at low temperature which comes up due to coupling of electrons with phonon, indicating a strong electron-phonon coupling. In HOPG we see only a single  $\pi$  band feature near the Fermi energy at its zone boundary. The inherent azimuthal disorder of HOPG makes it difficult to resolve the two  $\pi$  bands at the zone boundary. To study the conduction band structure of HOPG along a radial direction of its circular Brillouin zone and that of a single crystal graphite along a direction,

slightly away from the  $\Gamma M$  symmetry direction, we have used KRIPES. We see that for both the systems, the results superimpose on the theoretical conduction band structure of graphite along  $\Gamma M$  direction. In order to calculate the band structure of three dimensional graphite we have first constructed a formalism for the electronic structure calculation of single layer graphene, developed the method for bilayer graphene including up to third nearest neighbour interactions and finally applied it on graphite. From the calculations on graphene we have got a set of tight binding parameters on the physical ground that the absolute values of the parameters should decrease as one moves from first nearest neighbour towards higher distance. This set of parameters has been used to see the effect of in-plane first nearest neighbour overlap integral, second and third nearest neighbour interactions on the band structure of bilayer graphene. We have also illustrated the role of site energy difference ( $\Delta$ ) between A and B sublattices in the same graphene layer on the electronic spectra of bilayer graphene. The Sublattice asymmetry in monolayer graphene introduces a gap in the spectra at the  $K$  point whereas in bilayer it gives an asymmetry in the energy values of the top valence and bottom conduction bands with respect to the energy at which the other two bands are degenerate. The different in-plane parameters also induce electron-hole asymmetry in the slope of the valence and conduction bands. The effects of these parameters are similar, on graphite at the  $K$  point, to those of bilayer graphene but at the  $H$  point a gap opens up due to  $\Delta$ .

Further, we have studied the valence band electronic structure of the  $\text{Bi}_{1-x}\text{Pb}_x\text{FeO}_3$  ( $x = 0.02$  to  $0.15$ ) system by using X-ray and ultra-violet photoelectron spectroscopy. As this system undergoes a R3c to cubic phase transition with Pb doping, the near Fermi level states show an enhanced oxygen 2p character due to the weakening of the Fe 3d - O 2p - Bi 6p hybridization strength. The valence bands of compositions with the R3c structure were found to be qualitatively similar to the LSDA calculations except for their estimates of the band width and band gap. Reasons for this could be the higher value of the effective Coulomb interaction. These results could be of importance to the understanding of the electron-electron correlation in multiferroic materials.

Finally, we have studied the electronic structure of  $\text{Sm}_{0.1}\text{Ca}_{0.9-x}\text{Sr}_x\text{MnO}_3$  ( $x=0.0, 0.2, 0.3, 0.4$  and  $0.6$ ) system, an electron-doped CMR material using ultra violet photoelectron spectroscopy (UPS) and resonance photoelectron spectroscopy (ResPES) with varying photon energy across the Mn 2p-3d absorption edge. The magnetic ground state of the parent compound ( $\text{Sm}_{0.1}\text{Ca}_{0.9}\text{MnO}_3$ ) at low temperatures consists of ferromagnetic clusters (FM) embedded in a G-type AFM phase. But this FM component is very sensitive to the substi-

tution of Sr for Ca. From the combined UPS and ResPES studies we find that the valence band of this material has major contribution from Mn 3d states and a strong hybridization is there between Mn 3d  $t_{2g}$  and O 2p states. With strontium doping, the A site cation size increases and a significant change in the Mn 3d spectral weight is observed which indicates that there is a change in Mn 3d - O 2p hybridization strength due to structural modification caused by Sr doping.

Regarding the first part of this thesis, i.e., the electronic structure study of graphite, it could be noted that though the system has been studied earlier quite a bit, many of its modified forms like intercalated and irradiated graphite might display interesting physics if reinvestigated using the advanced experimental facilities that are available in the present day. On the other hand, the transition metal oxides need a lot more studies for a better understanding of their complex physical properties.